Wall Adhesion Characteristics of Fuel Spray Impinging on Flat Wall in Cross-Flow Ambient under Split Injection Condition

（横風中で平板壁面に衝突するスプリット噴射燃料噴霧の壁面付着特性）

By

史 鵬華（SHI PENGHUA）

Dissertation

Submitted in Partial Fulfillment of the Requirements for the

Degree of Doctor of Engineering

at

Mechanical Engineering Program

Division of Advanced Science and Engineering

Graduate School of Advanced Science and Engineering

Doctor of Engineering

Hiroshima University

September 2024

ABSTRACT

In Direct Injection Spark Ignition (DISI) engines, the small cylinder volume and high injection pressure result in high-pressure fuel injectors introducing fuel into the cylinder. This leads to fuel spray coming into contact with and adhering to the cylinder walls, creating flat-wall wetness phenomenon on the piston surface and cylinder wall. The phenomenon of fuel adhesion following wall impingement adversely impacts fuel spray mixture formation, leading to increased fuel consumption and higher pollutant emissions, thereby reducing the combustion efficiency of the engine.

To improve the high combustion efficiency and low emissions of gasoline engines, the high-pressure wind tunnel was used for the experimental investigation. The study examined the effects of different cross-flow velocities, injection strategies, and wall impingement distances on the characteristics of spray impingement structure and fuel adhesion distribution. The Particle Image Velocimetry (PIV) technology is utilized to assess cross-flow field uniformity at different velocities. The continuous wave laser-Mie scattering technique was constructed using a high-speed camera and laser sheet light to observe the wall-impingement spray structure in the vertical plane. The fuel adhesion characteristics of the wall spray were examined using the Refractive Index Matching (RIM) method. Subsequently, the area, mass, and thickness of fuel adhesion are calculated using MATLAB.

The findings demonstrate that under cross-flow field conditions split injection can decrease the fuel adhesion area, thickness, and mass. When the cross-flow velocity is high, the fuel adheres to the surface in the shape of longer strips. In the early stage, an increase in cross-flow velocity leads to a higher growth rate of the fuel adhesion area. In the later stage, the rate at which the fuel adhesion area decreases initially rises with an increase in cross-flow velocity. However, once the critical velocity threshold of 20 m/s is surpassed, this decreases rate tends to stabilize. In addition, the cross-flow enhances the volatilization of the spray and fuel adhesion, leading to a reduction in fuel adhesion mass over time. Consequently, in the later stage, the average fuel adhesion thickness decreases as cross-flow velocity and impingement distance increase. In the later stages, the fuel adhesion area increases proportionally with the impingement distance. The fuel adhesion mass and ratio of fuel adhesion mass

increase with the increase of the impingement distance. Additionally, the spreading of fuel adhesion was proposed to evaluate the fuel adhesion distribution. The spreading of fuel adhesion increases with the increase of the impingement distance. In the context of carbon neutrality, this study highlights the critical need to optimize fuel injection conditions to reduce both emissions and fuel consumption.

NOMENCLATURES

D	Hole diameter
D_{imp}	Impingement distance
f	Relationship between the transmittance and fuel adhesion thickness
I	Gray value of the spray image
I_0	Gray value of the background light
I_d	Deformation coefficient
I_{dry}	Surface brightness of a dry quartz flat-wall
I_{wet}	Surface brightness of a wet quartz flat-wall after fuel adhesion
P_a	Ambient pressure
P_{ing}	Injection pressure
R_f	Surface roughness
T_{tem}	Room temperature
U_x	cross-flow velocity
m	Injection mass
ΔI	the change in transmittance
h	fuel adhesion thickness
ASOI	After Start of Injection
CCD	Charge-Coupled Device
COP 15	15th Conference of the Parties
CO	Carbon Monoxide
CO_2	Carbon Dioxide
CW	Continuous Wave
DISI	Direct Injection Spark Ignition

ECU	Electronic Control Unit
GDI	Gasoline Direct Injection
HC	Hydrocarbons
HOS	Homogeneous Stratified
HSV	High-Speed Video
ICEs	Internal Combustion Engines
IEA	International Energy Agency
IVC	Intake Valve Closing
IPCC	Intergovernmental Panel on Climate Change
LAS	Laser Absorption Scattering
LED	Light Emitting Diode
LIF	Laser-Induced Fluorescence
2p-LIF	Two-Photon Excitation Laser-Induced Fluorescence
N_2	Nitrogen
NO_x	Nitrogen Oxides
PDF	Probability Density Function
PFI	Port Fuel Injection
PIA	Particle Image Analysis
PIV	Particle Image Velocimetry
PLC	Programmable Logic Controller
PM	Particulate Matter
RANS	Reynolds-Averaged Navier–Stokes
RIM	Refractive Index Matching
UHC	Unburned Hydrocarbon
We	Weber number

wOFV   Wavelet-Based Optical Flow Velocity

TABLE OF CONTENTS

CHAPTER 1 INTRODUCTION

1.1 Background and Motivation

1.1.1 Energy and environmental

The 15th Conference of the Parties (COP 15) of the United Nations Framework Convention on Climate Change emphasized the significance of greenhouse gas emissions in global warming, warning that failure to control these emissions would result in unacceptable increases in Earth's temperature and entail severe consequences [1, 2]. Rising temperatures are directly linked to increased risk. The five metrics for assessing climate-related risks are illustrated in Figure 1.1 [3]. Observed global warming is primarily attributed to anthropogenic greenhouse gas emissions, with Carbon Dioxide (CO_2) being the most prominent component originating from various activities associated with fossil fuel usage [2]. The relationship between cumulative anthropogenic CO_2 emissions and global warming is approximately linear. It has been assessed that every 1000 gigatons of CO_2 emissions may lead to a global surface temperature increase ranging from 0.27°C to 0.63°C. The near-linear relationship between cumulative CO_2 emissions and global surface temperature increase is depicted in Figure 1.2 [4].
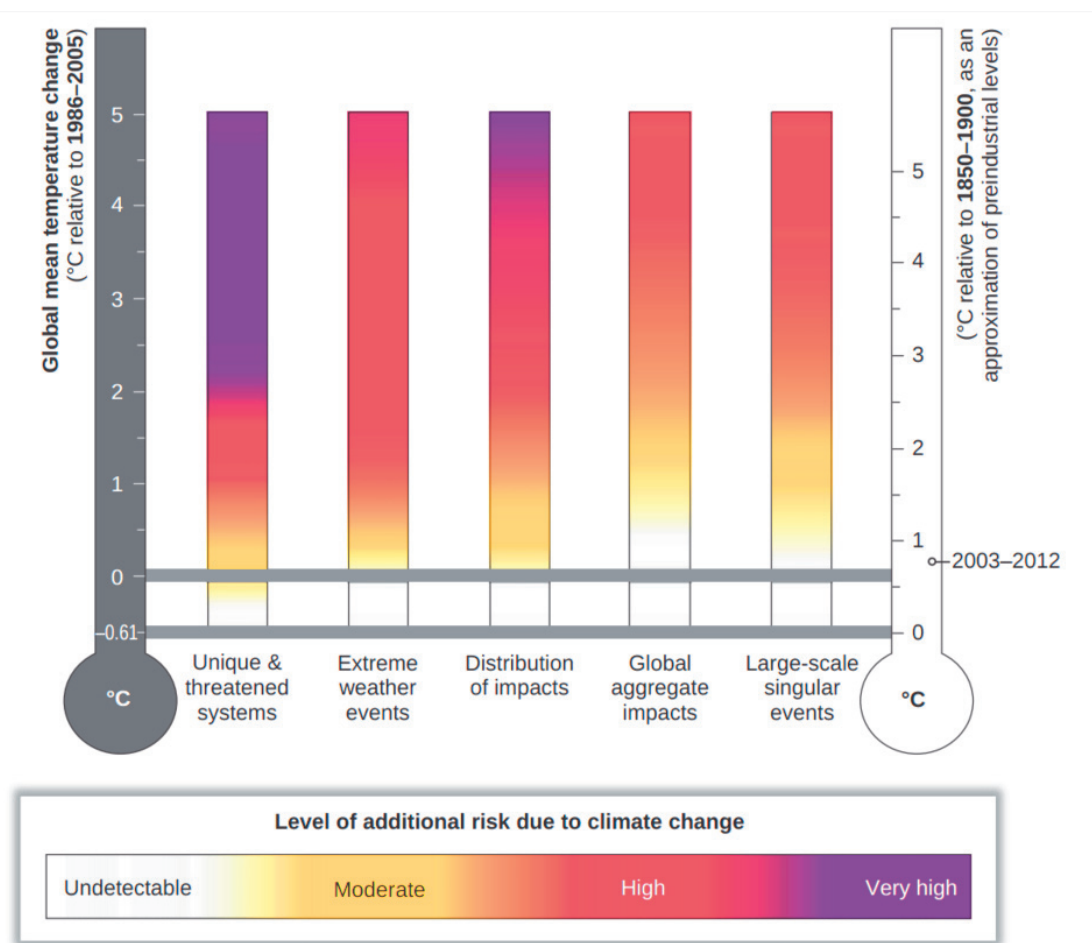
Figure 1.1 Five measures of climate-related risks [3].

According to the Intergovernmental Panel on Climate Change (IPCC) Fifth Assessment Report, achieving specific temperature limits necessitates setting clear limits on greenhouse gas emissions. For instance, to keep the global average temperature increase within 2°C, stringent cumulative emission limits must be established [5]. As highlighted by Tejal Kanitkar in the referenced article, restricting temperature increases to within 2°C requires limiting cumulative emissions to 992 billion tons of carbon between 1870 and 2100, ensuring a 67% likelihood of temperature control within the specified threshold. This implies that only 325 gigatons of carbon equivalent emissions can be emitted between 2012 and 2100 [3].
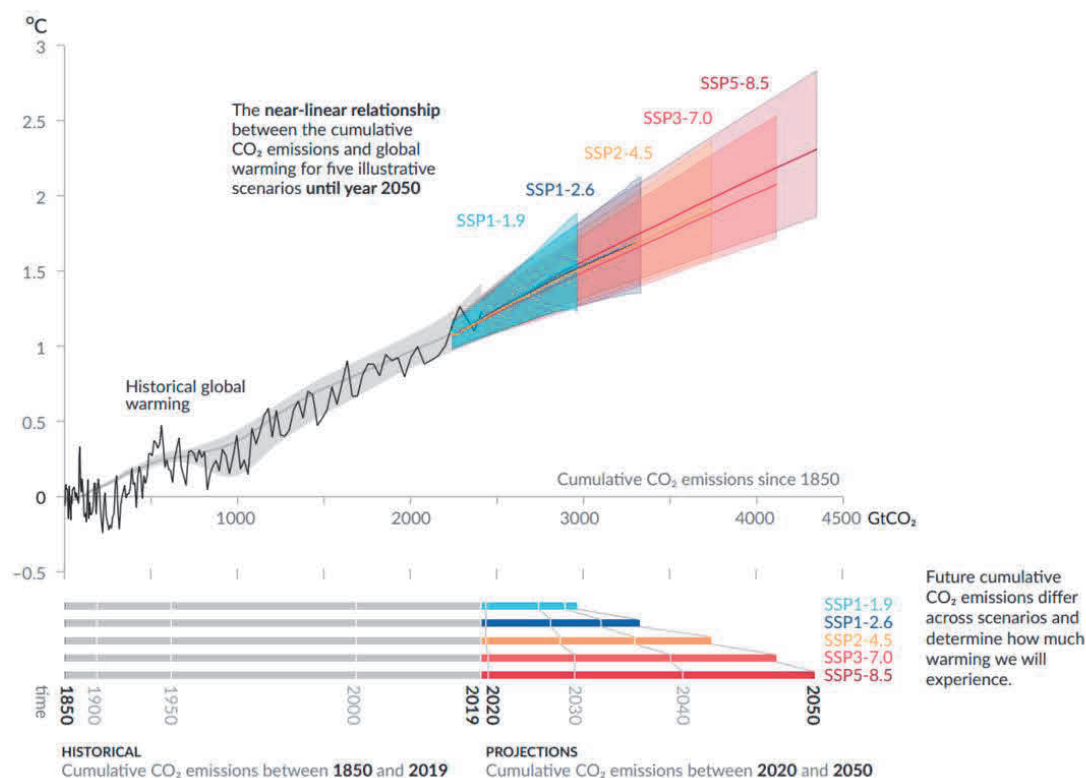
Figure 1.2 Near-linear relationship between cumulative CO_2 emissions and the increase in global surface temperature [4].

In the Paris Agreement, to lessen the dangers and effects of climate change, governments pledge to work toward limiting the rise in the world's average temperature to well below 2°C above pre-industrial levels and to pursue efforts to limit the temperature increase to 1.5 °C above pre-industrial levels. The Paris Agreement highlights the necessity of limits and regulations on greenhouse gas emissions in order to accomplish this goal [6]. The energy supply total and CO_2 emission intensity in The International Energy Agency (IEA) are depicted in Figure 1.3 [7].

Coal use declines, oil plateaus and renewables and natural gas grow substantially to 2050

Note: EJ = exajoule; MJ = megajoule; TES = total energy supply.
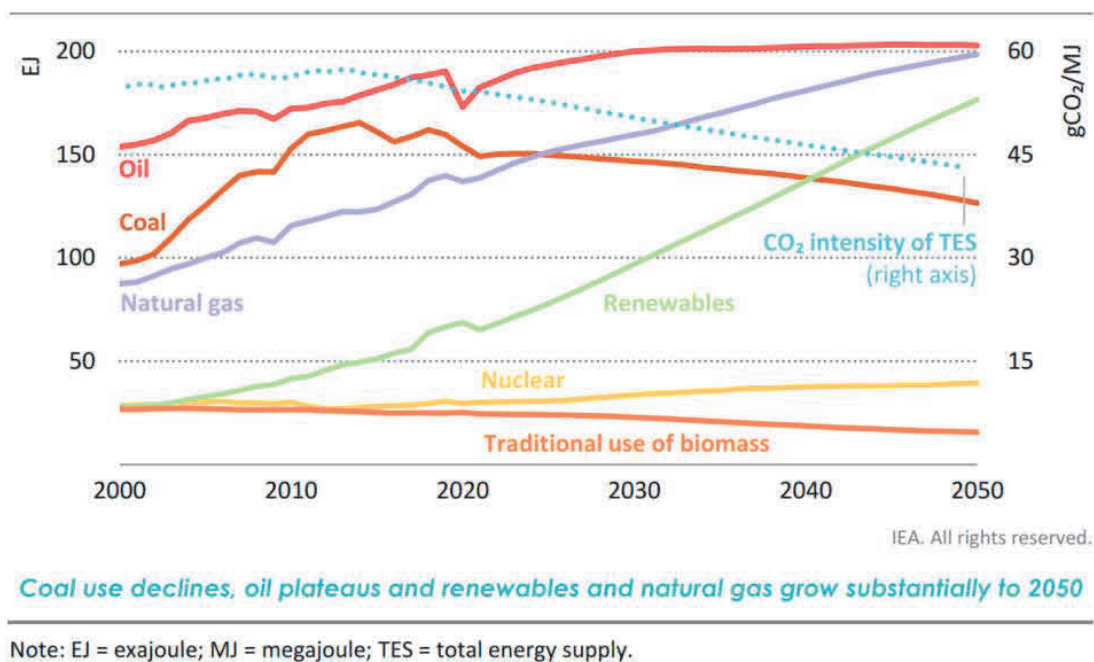
Figure 1.3 Total energy supply and CO$_2$ emissions intensity [7].

The transportation industry is widely recognized as one of the largest carbon emitters. Figure 1.4 depicts global CO$_2$ transport emissions by mode, as well as the share of emissions reductions by 2050 based on technological maturity. As a cornerstone industry of the national economy, it has rapidly expanded alongside the acceleration of urbanization and modernization. However, due to its heavy reliance on fossil fuels, especially gasoline, the transportation sector accounted for 28.89% of total energy consumption in 2017 [8]. The sector predominantly relies on fossil fuels, resulting in its carbon emissions contributing to over 20% of the total emissions. In 2020, global CO$_2$ emissions from the transportation sector exceeded 7 billion tons [7, 9]. The increasing use of fossil fuels in transportation and the consequent rise in carbon emissions are causing sustainability issues. Figure 1.5 shows total final consumption by sector and fuel between 2020 and 2050. The automotive industry requires cleaner and more efficient technologies to improve environmental quality and reduce emissions. While hybrid and electric vehicles are important, gasoline will remain the primary fuel for the foreseeable future. Hence, technologies such as Direct Injection Spark Ignition (DISI) engines, which enhance engine performance, are under recent

scrutiny.
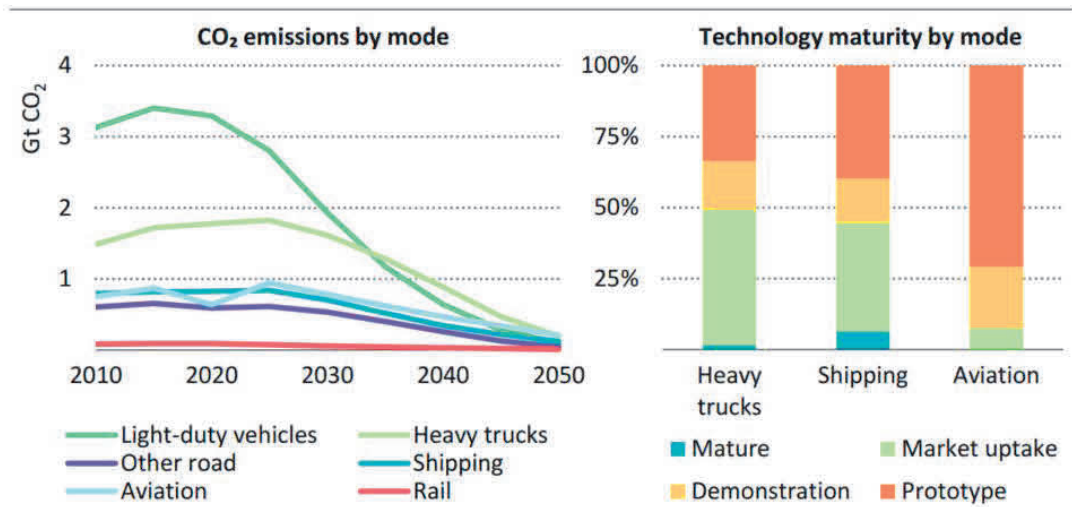
Figure 1.4 Global CO₂ transport emissions by mode and share of emissions reductions to 2050 by technology maturity [7].

With the growth of the global economy, it is crucial to utilize energy more efficiently and enhance resource efficiency. The transportation sector represents a significant portion of total energy consumption and is one of the most fossil fuel-dependent sectors, contributing substantially to greenhouse gas emissions and exerting immense pressure on the environment and human well-being [9-11]. Therefore, global action must be taken to curb greenhouse gas emissions, achieve the goals of the Paris Agreement, and mitigate the adverse effects of climate change on the Earth and human society. Exploring emission reduction strategies in the transportation sector is indispensable.
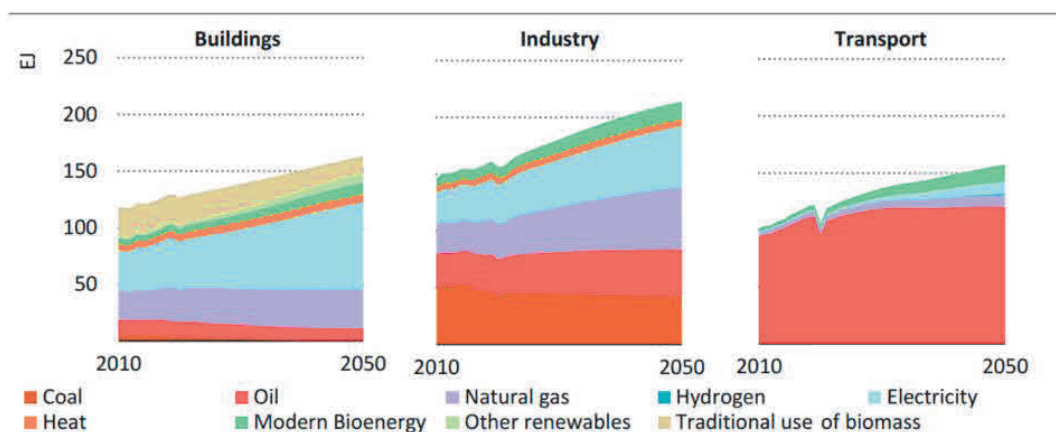
Figure 1.5 Total final consumption by sector and fuel [7].

1.1.2   DISI (Direct Injection Spark Ignition) engines

Carbon neutrality goals aim to achieve net-zero or zero carbon emissions by reducing or offsetting carbon emissions [6]. The IEA reports that automakers are striving to lower fuel consumption and emissions to meet regulations on greenhouse and polluting gas emissions [12, 13]. Engine strategies have the potential to reduce CO_2 emissions by up to 30% [14]. DISI engines are widely favored due to their low fuel consumption and high fuel efficiency.

Experimental investigations reveal that DISI engines consume less fuel and emit lower levels of Carbon Monoxide (CO), total hydrocarbons, and Particulate Matter (PM) compared to Port Fuel Injection (PFI) engines. Notably, PM emissions from PFI engines are significantly higher than those from DISI engines during startup [15]. Compared with the PFI system, the DISI system can significantly improve fuel economy by achieving load control without throttling, mainly due to its more precise fuel control and more efficient combustion process [16]. Figure 1.6 shows PFI and DISI engine [17].

(a) PFI engine   **(b) DISI engine**

Figure 1.6 PFI and DISI engine [17].

The widespread adoption of DISI engines can be attributed to their low fuel consumption, excellent fuel efficiency, and low emissions [18-20]. Moreover, DISI engines offer advantages such as high sensitivity and a high compression ratio [21]. However, the limited air-fuel mixing in DISI engines, caused by their small volume and high injection pressure, leads to fuel adhesion on piston surfaces and cylinder walls. This can result in pool fires, deposits, and exacerbated soot formation [22-24]. Consequently, there is an increase in fuel consumption and emissions, including PM and unburned hydrocarbon (UHC) compounds [25-27]. Meeting emission standards, such as Euro 6c, is challenging due to the fuel adhesion issue in direct injection engines [28, 29]. Before carbon-free energy completely replaces traditional DISI engine, addressing this issue is essential. To achieve these goals in DISI engine, two operating modes are required: stratified and homogeneous charge modes, as shown in Figure 1.7 [30].
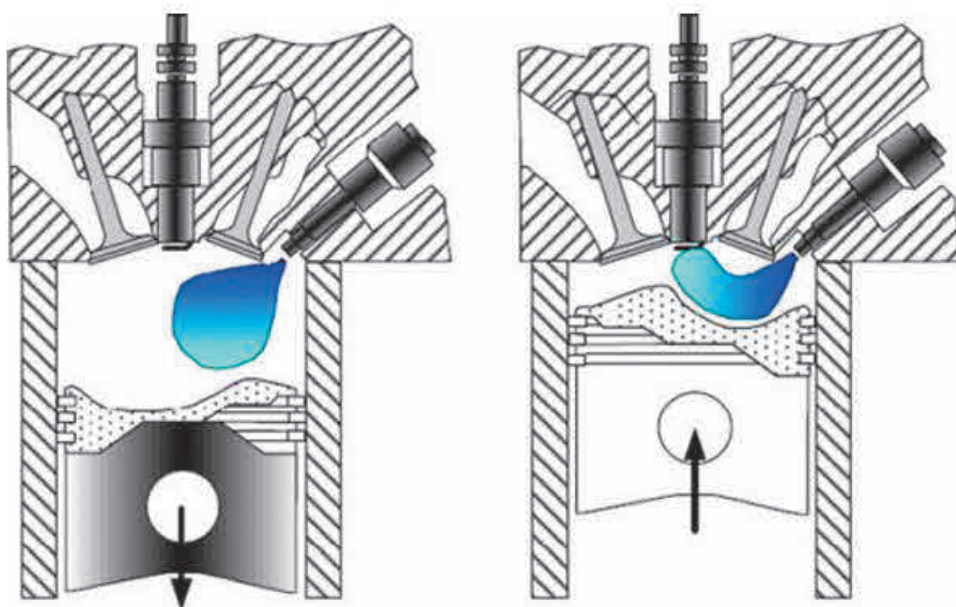
(a) Homogeneous mode   **(b) Stratified mode**

Figure 1.7 Two basic charge modes of DISI engines [30].

The working mode of the DISI engine is depicted in Figure 1.8. During low load/low-speed operation, the engine operates with stratified charge and lean mixture. Conversely, under higher load/speed conditions, the engine operates with homogeneous charge. The homogeneous charge operation is divided into two regions: moderate load and high load [31, 32].
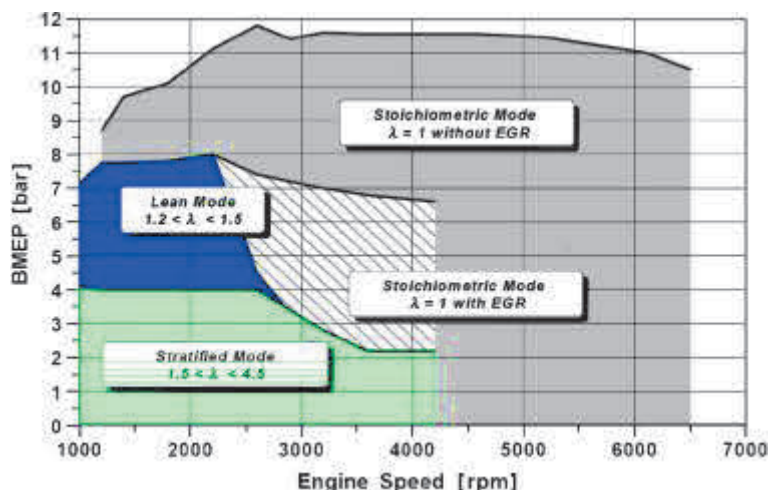
Figure 1.8 Operational modes for the DISI engines [32].

The combustion systems of DISI engines can be classified into three main categories: air-guided, wall-guided, and spray-guided, as illustrated in Figure 1.9 [32-36].
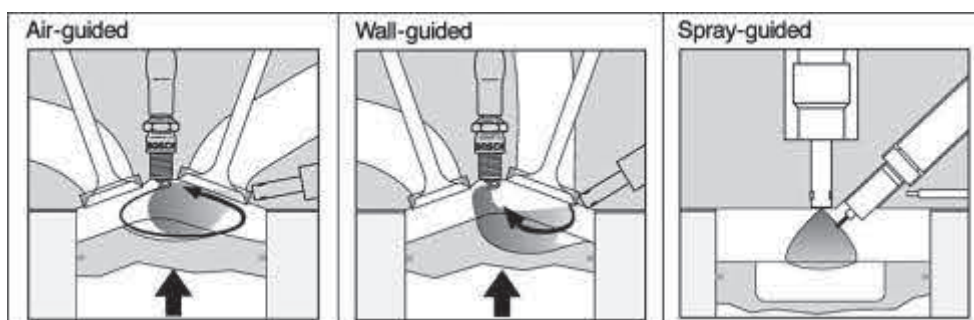
Figure 1.9 Classification of the GDI combustion systems [32].

Spray-guided combustion system: In this system, the spark plug and injector are positioned very close, forming a limited spatial stratification. This system requires high physical characteristics of the spray. Although the stratified mixture is unstable

and fuel spray can easily impact the spark plug, the combustion system can reduce pollutant emissions and improve combustion efficiency. The spray-guided combustion system needs to pay attention to the insufficient extension of the flammable mixture area around the spray, and the installation geometry and spray characteristics are crucial for this system.

Wall-guided combustion system: In this system, the distance between the spark plugs and injector is relatively large. Due to the presence of the combustion chamber wall (usually a specially shaped piston), the fuel spray is guided towards the spark plug, forming a clearly stratified mixture. This system can avoid spark plug wetting phenomenon, demonstrating good combustibility, but it may lead to the formation of fuel film and incomplete combustion.

Air-guided combustion system: In this system, airflow is generated in the cylinder to help the fuel spray reach the spark plug, forming a stratified mixture. Although it can avoid spark plug wetting and reduce the formation of fuel film, which is beneficial for lowering engine emissions, the airflow is unstable and difficult to form, with relatively low intensity.

To tackle these challenges, a comprehensive study of spray-wall impingement dynamics within DISI engines, with a specific focus on fuel adhesion characteristics, is crucial.

1.2 Objectives and Approaches

This study aims to investigate the effects of impingement distance and cross-flow velocity on impingement spray and fuel adhesion characteristics under the split injection strategy. It aims to elucidate the impact of in-cylinder airflow on spray behavior and thereby lays the foundation for this understanding. Therefore, this research examines impingement spray and fuel adhesion from four perspectives.

(1) Utilizing Particle Image Velocimetry (PIV) technique to evaluate the uniformity of flow field distribution in cross-flow at different velocities, thereby

understanding the impact of cross-flow on spray dispersion and fuel adhesion.

(2) Investigating the evolution patterns of impinging spray and fuel adhesion under cross-flow and static flow field conditions with various injection strategies.

(3) Studying the influence of different cross-flow fields on split spray and fuel adhesion characteristics.

(4) Exploring the effects of different wall impingement distances on impinging spray and fuel adhesion under cross-flow conditions.

In this study, the uniformity of cross-flow fields at different velocities was assessed using PIV technique to gain insights into the impact of cross-flow on fuel adhesion and spray dispersion. Additionally, an optical setup was constructed using high-speed cameras and laser sheet illumination to observe the impingement spray structure in a vertical plane. Furthermore, the fuel adhesion characteristics of impingement spray were examined using the Refractive Index Matching (RIM) method.

1.3 Outlines

To introduce this research, the research will be structured as follows:

Firstly, Chapter 1 introduces the background of this study, covering topics from energy and environment to DISI engines. The review of research progress on various aspects such as spray mixture formation, spray in cross-flow, spray/wall interaction, split spray, and fuel impingement, and also includes optical diagnostic techniques in the field of spray research.

Secondly, Chapter 2 introduces the experimental setup of this study, including the cross-flow setup, fuel injection system, and image acquisition system, among others. The optical diagnostic techniques employed are PIV, continuous wave laser-Mie scattering technique, and RIM method.

Thirdly, Chapter 3 studies the wall-impingement distance of 75 mm as the baseline and describes in detail the behavior of the split spray before and after the wall-impingement in the cross-flow and its effect on the fuel adhesion. Chapter 4 studies

the spray development and fuel adhesion characteristics of different injection strategies under cross-flow and static flow fields. Chapter 5 examines the impact of varying cross-flow velocities on the spray evolution and fuel adhesion characteristics of split injection. Chapter 6 studies the influence of different impingement distances on the spray development and fuel adhesion characteristics of split injection.

Finally, Chapter 7 summarizes the effects of various injection strategies, cross-flow velocities, and impingement distances on spray development and fuel adhesion characteristics.

1.4 Review of Previous Works

1.4.1   Fuel adhesion

The engine fuel injector blends liquid fuel with air, crucially impacting the ignition, heat release, pollutant emissions, and fuel efficiency of a direct injection engine. Throughout the fuel injection process, a fuel jet initially forms and swiftly fragments into a conical spray. This initial breakup predominantly occurs near the nozzle, generating large ligaments and droplets, resulting in a dense spray. Elevated injection pressure escalates the breakup process, exacerbated by cavitation and turbulence within the nozzle, leading to secondary breakup. Droplets gradually diminish in velocity due to relative gas speed and decelerate owing to gas resistance. Intense resistance expedites droplet loss of momentum near the nozzle [37-40]. Over time, droplets at the spray's apex are replaced by fresher ones, shaping a conical spray structure. As shown in Figure 1.10.

Dense droplets concentrate near the nozzle, while downstream, they are diluted by entrained air. This distribution emerges from interactions between the spray and entrained gas. In regions of dense droplets, collisions may arise, inducing instability in droplet size and speed. These collisions prompt droplet coalescence, forming larger droplets. Gas temperature, density, and flow rate serve as boundary conditions influencing downstream dilution spray in the nozzle. Droplets exhibit high sensitivity

to these conditions, pivotal in further spray decomposition and evaporation. The maximum penetration distance of the spray spans from the nozzle to the piston bowl. High pressure, prolonged injection, or low gas density may impact the wall, culminating in a liquid wall film. Owing to evaporation challenges, the fuel mixture may undergo partial combustion, leading to decreased fuel efficiency and heightened emissions.
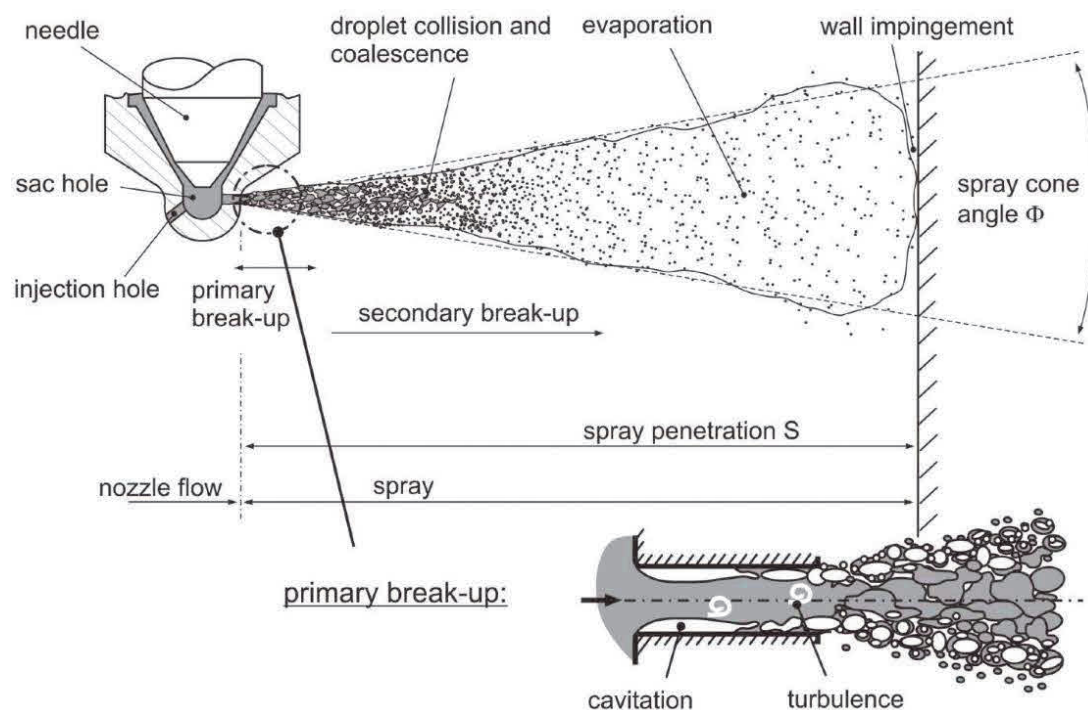
Figure 1.10 Spray breakup process from hole-injector [41].

Due to high injection pressure and small cylinder volume, fuel spray may impact the piston bowl wall before complete vaporization. The spray/wall interaction has received extensive attention from automotive engineers. Depending on surface characteristics, including surface morphology and chemical properties, the outcomes of droplet impingement on solid, non-porous surfaces are relatively complex.

Rioboo et al. [42] initially categorized six potential outcomes in 2001, which included deposition, prompt splash, and corona splash, rebound rupture, partial rebound, and complete rebound. Figure 1.11 illustrates typical outcomes of droplet impingement on solid surfaces [43].
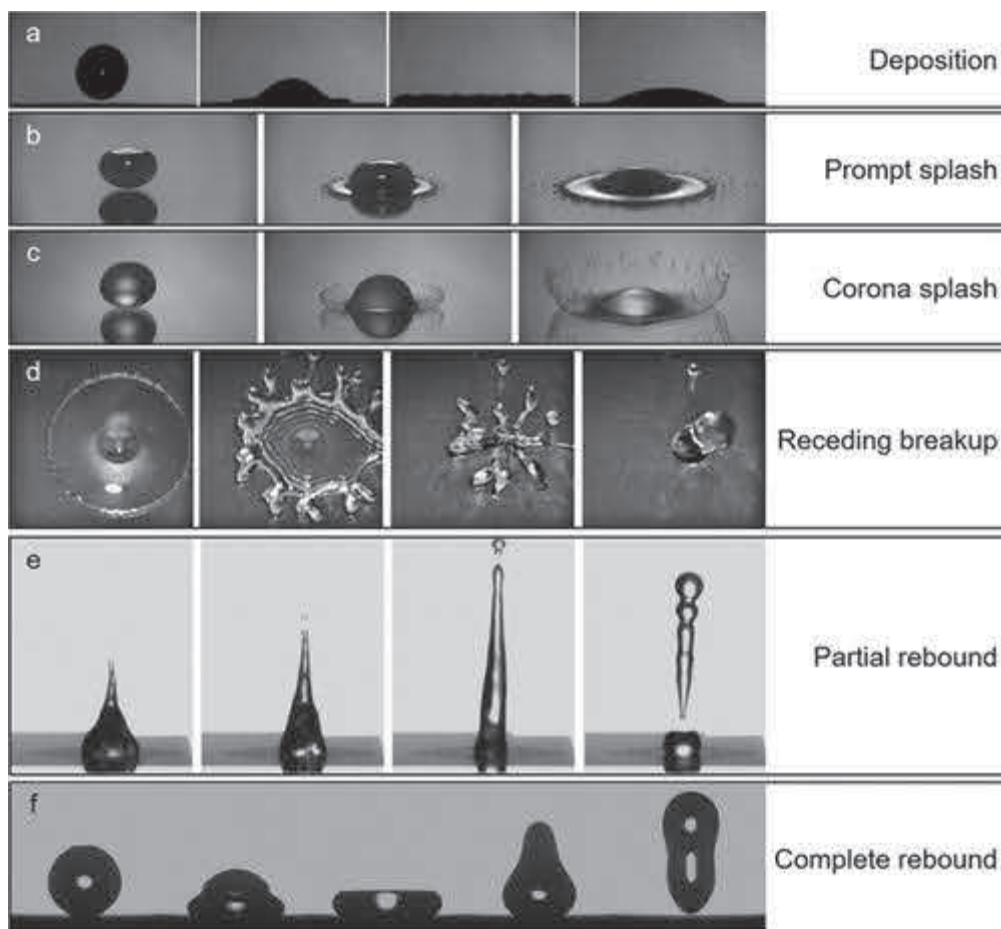
Figure 1.11 Typical outcomes of liquid droplet impact on a solid surface [43].

Fujimoto et al. [44] initially explored the interaction between spray and wall at room temperature, followed by further investigation by Katsura et al. [45], who proposed a classical spray-wall interaction model as depicted in Figure 1.12. After impact, the spray flows along the wall, particularly forming a wall jet vortex region at the spray tip due to the resistance of surrounding airflow. This vortex causes the liquid droplets to be entrained, enhancing the spray dispersion. Closer to the wall, the droplet density is higher at measurement points. Along the wall direction, the droplet concentration varies with distance, being more concentrated at the impact point and the wall jet vortex region.
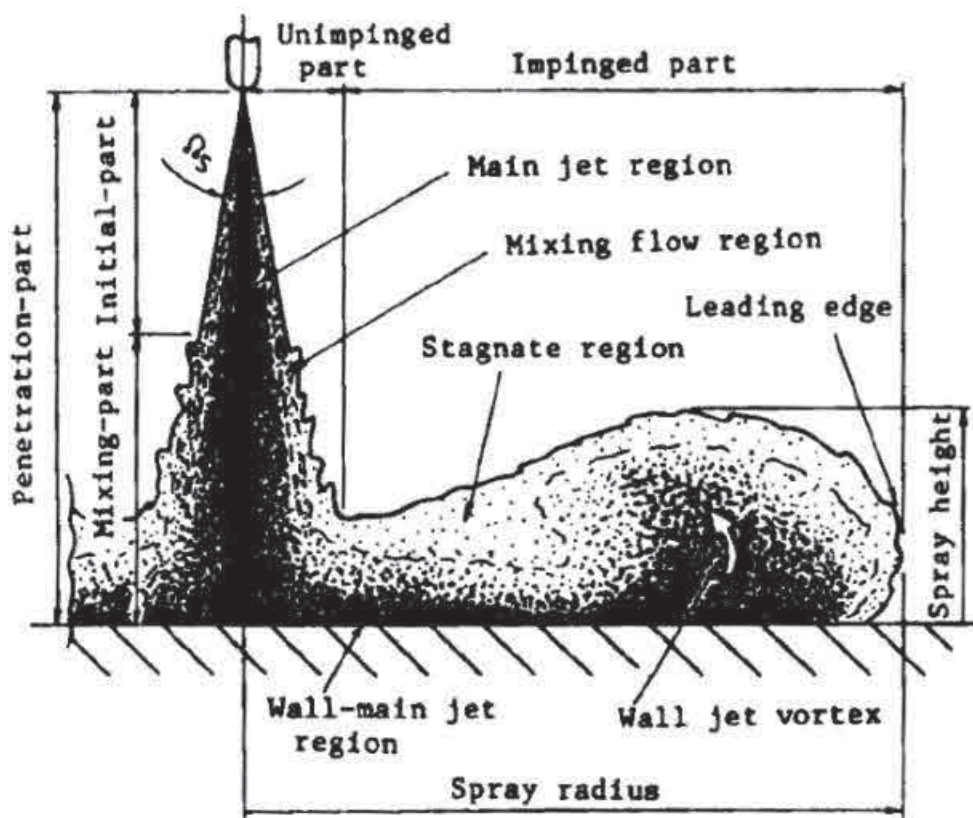
Figure 1.12 Model of a wall-impingement spray [44].

Zhao et al.[46] conducted a study on the interaction between high-pressure fuel spray and a flat solid wall using a combination of experiments and numerical simulations based on the Reynolds-averaged Navier-Stokes (RANS) method. The experiments were performed in a constant-volume combustion chamber, where Mie scattering and shadowgraph optical diagnostics were employed to characterize the spray properties. Features were extracted using internal MATLAB image processing code. The experimental results revealed that the penetration distance of rebound spray exceeds the spreading distance of the spray on the wall. Numerical simulations accounted for the influence of spray on grid resolution and were matched with experimental results to assess the capability of the spray-wall interaction model. Figure 1.13 shows the schematic of spray-wall interaction.
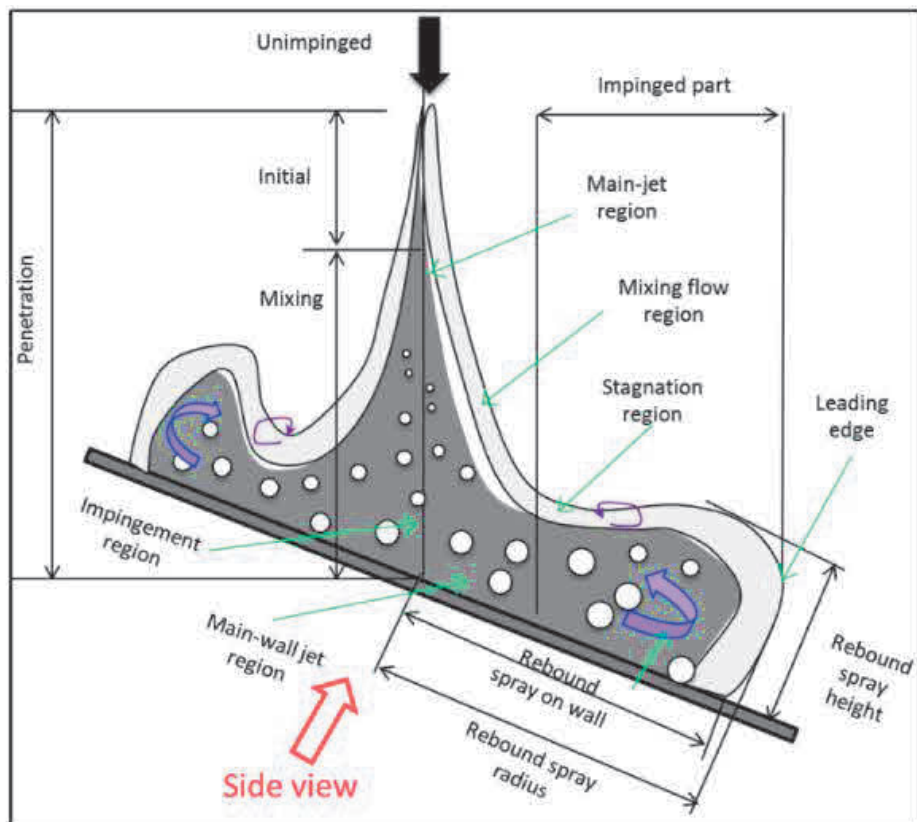
Figure 1.13 Schematic of spray-wall interaction [46].

Numerous researchers have explored elements that can impact fuel adhesion characteristics, for instance, injection pressure, ambient temperature, and ambient pressure. He et al. [47] employed the RIM method to examine the impact of varying ambient pressures on the fuel adhesion during flash boiling. The results showed that the ambient pressure is inversely related to the rate of fuel film evaporation, and that flash boiling promotes fuel film evaporation. Luo et al. used the RIM method to study the influence of impingement distance, ambient temperature, ambient pressure/ injection pressure, and roughness of the impingement wall on fuel adhesion characteristics [48-52]. The findings of this study indicated that the fuel adhesion mass rose as the impingement distance grew [48]. When the ambient temperature was relatively high, the thin fuel adhesion evaporated rapidly; however, the thick fuel adhesion hardly evaporated, resulting in more uniform fuel adhesion on the wall [49]. Figure 1.14 shows the evolution of fuel adhesion on the wall [49].
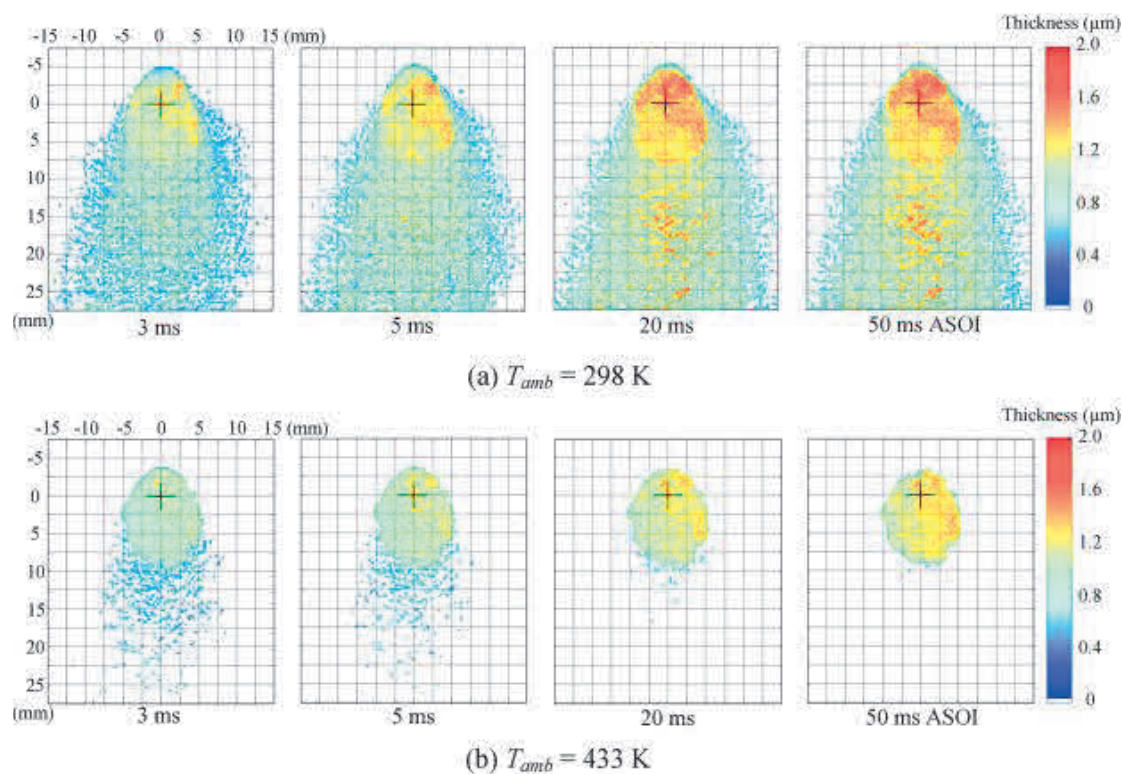
Figure 1.14 Evolution of fuel adhesion on the wall [49].

As the ambient pressure rises, the fuel adhesion area and mass rise [50]. At room temperature, the fuel adhesion area and mass tend to rise with the injection pressure; by contrast, increasing the injection pressure causes both the fuel adhesion area and mass to decrease under the high ambient temperature [51]. The uniformity of the fuel adhesion distribution decreases with an increase in the roughness of the impingement wall [52]. In addition, Akop et al. [53] studied the adhesion characteristics of diesel spray when impacting a flat disk. Various disk sizes and tilt angles were tested, revealing that the thickness of the liquid film decreased with increasing injection pressure, and higher disk tilt angles led to a reduction in the mass ratio of adhered fuel.

Most scholars have focused on the fuel adhesion characteristics produced by wall impingement spray to prevent the formation of fuel adhesion. However, most studies on fuel adhesion were conducted in a static flow field, which should be investigated further under an airflow flow field.

1.4.2   Split Injection

Considering the influence of the variations in injection penetration and momentum flux on the fuel spray mixture distribution inside the cylinder, previous research has proved that the timing and ratio of fuel splits had a significant impact on emissions and combustion [54]. Busch et al. [55] incorporated thermodynamic and injection rate data to verify the effectiveness of the split injection method in reducing combustion noise. Zhang et al. [56] analyzed the effect of the multi-segment injection strategy on the fuel/air equivalency ratio. According to this study, when the injection segment is increased, the average fuel/air equivalency ratio decreases and the impact of fuel-air mixture grows. Li et al. investigated the impact of split injection on the mixture generation process [57, 58]. According to the findings, split injection promotes the formulation of a more flammable combination because the spray brings on the ambient air motion, enables the subsequent evaporation of the second spray, and aids in the development of the split spray mixture. Wang et al. [59, 60] studied the spray properties of split injection under different flash evaporation conditions and the interaction between split injections. Their research findings indicate that employing a split injection strategy can significantly reduce the total penetration length of the spray and weaken the impact mist effect. Higher film formation rates are typically observed during secondary injections. Additionally, larger droplet sizes were observed in the split injection strategy. Yang et al. [61] utilized the Laser Absorption Scattering (LAS) technique to study the impact of split injection on the formation and combustion processes of diesel spray mixture. Experimental findings reveal that the vapor distribution with split injection is notably more uniform compared to single injection. Furthermore, split injection demonstrates a significantly higher reduction rate in smoke particles compared to single injection. Chang et al. [62] used the RIM method to investigate the fuel adhesion characteristics of split injection under high- and low-ambient-temperature conditions. The experimental findings indicated that the fuel adhesion mass ratio of split injection marginally increased but was more uniform

under high-temperature conditions. Figure 1.15 shows the fuel adhesion mass during split injection.
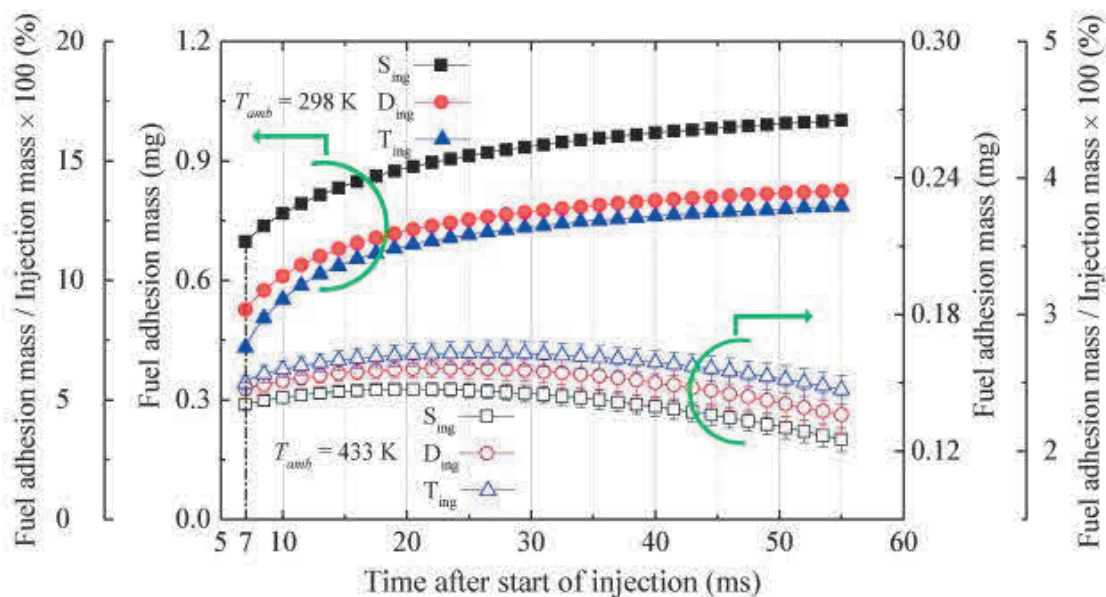
Figure 1.15 Fuel adhesion mass [62].

Compared to the single injection approach, split injection strategies have a significant influence on engine performance and emissions, and the Nitrogen Oxides (NO_x) and PM emissions can be decreased using the split injection strategy [63, 64]. Park et al. [65] also evaluated the exhaust emission characteristics under the split injection strategy; this strategy reduces soot, Hydrocarbons (HC), and CO emissions, as well as the number of large particles. Bo et al. [66] studied the impact of multi-injection strategy on the ignition process of low-temperature diesel injection. The results showed that pilot fuel injection could promote combustion and reduce the ignition delay of main injection fuel. To investigate the effect of fuel injection techniques on combustion parameters, Figure 1.16 depicts heat release rates with various injection strategies [66].

(a) $T_{atm} = 760$ K

(b) $T_{atm} = 800$ K
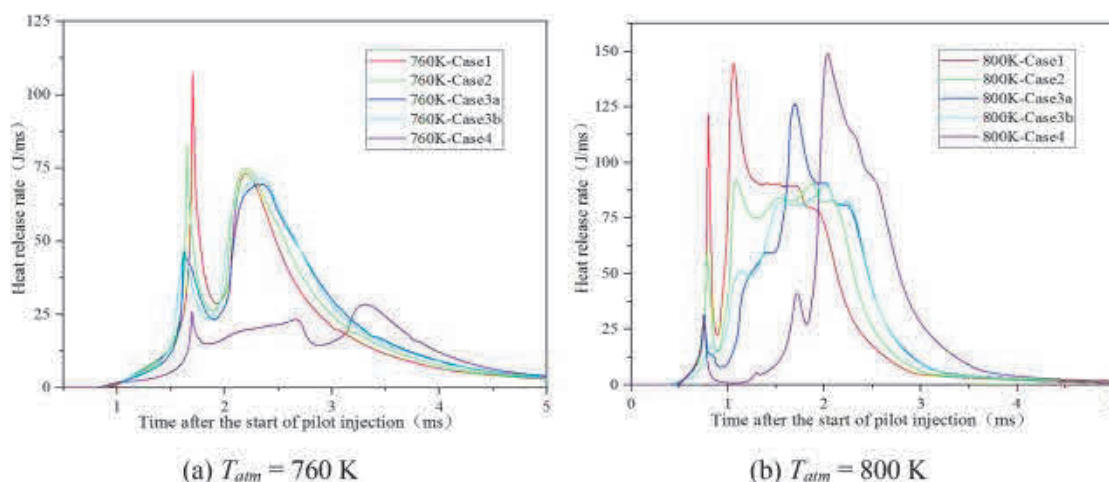
Figure 1.16 The heat release rate with different injection strategies. [66]

Costa et al. [67] analyzed the effects of separated injection events in a Gasoline Direct Injection (GDI) engine operating with Homogeneous Stratified (HOS) lean charge using experimental and numerical techniques. The research findings indicate that synchronizing the second injection affects the formation of PM and NO_x as well as power output. Faster heat release can be achieved by appropriately selecting spark timing and initiating the second injection before ignition. After preparing a homogeneous mixture with the first injection during the intake process, the second injection must occur immediately after Intake Valve Closing (IVC), and the spark timing must be advanced relative to single injection to improve engine power output and pollutant emissions. Figure 1.17 shows exhaust gas emissions and smoke opacity for various split injection cases as a function of SOI_2 [67].
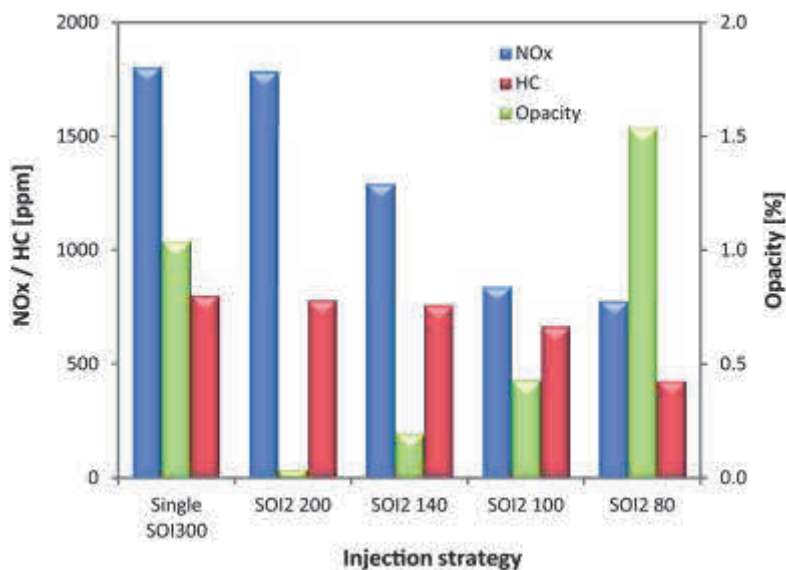
Figure 1.17 Exhaust emissions of NO$_x$, HC and opacity (soot) for single and split injections as a function of SOI$_2$ [67].

Kim et al. [19] investigated the impact of turbulence augmentation throughout the combustion procedure of the double injection strategy. The results demonstrated that the double injection strategy improved the turbulence intensity. Furthermore, the intensity of turbulent flow increased the speed of flame propagation. Park et al. [68] evaluated split injection as a strategy for achieving ultra-lean operation in GDI engines. Their study investigated the lean combustion characteristics resulting from this approach in terms of engine performance and emissions. Engine test results indicate that under lean combustion conditions, split injection of fuel enables the formation of well-stratified mixtures, ensuring stable combustion.

Yehliu et al. [69] examined the effects of single and split injection strategies on combustion and emissions when employing various fuels; the results indicated that NO$_x$ emission at high loads and PM emissions could be decreased by applying the split injection strategy. Oh et al. [70] investigated the effects of several injections on the spray-guided direct-injection spark-ignition engines' stratified combustion properties (using a single-cylinder engine). In the experimental findings from the dual-injection engine, the multi-injection strategy enhanced the local uniformity of the stratified mixture, resulting in improvements in both averages indicated pressure and

combustion efficiency. Additionally, significant decreases were observed in hydrocarbon and CO emissions. Tow et al. [71] showed that both double and triple injections were effective in reducing particle and NO_x emissions. Compared to single and double injection, triple injection provided greater flexibility in controlling heat release rates. Additionally, How et al. [72] investigated the impact of the split injection strategy on emissions, performance, and combustion characteristics. The results demonstrated that split injections are a feasible method for concurrently lowering NO_x and smoke emissions. Figure 1.18 depicts the amount of smoke emitted by each test fuel at various SOI timings and injection strategies [72].
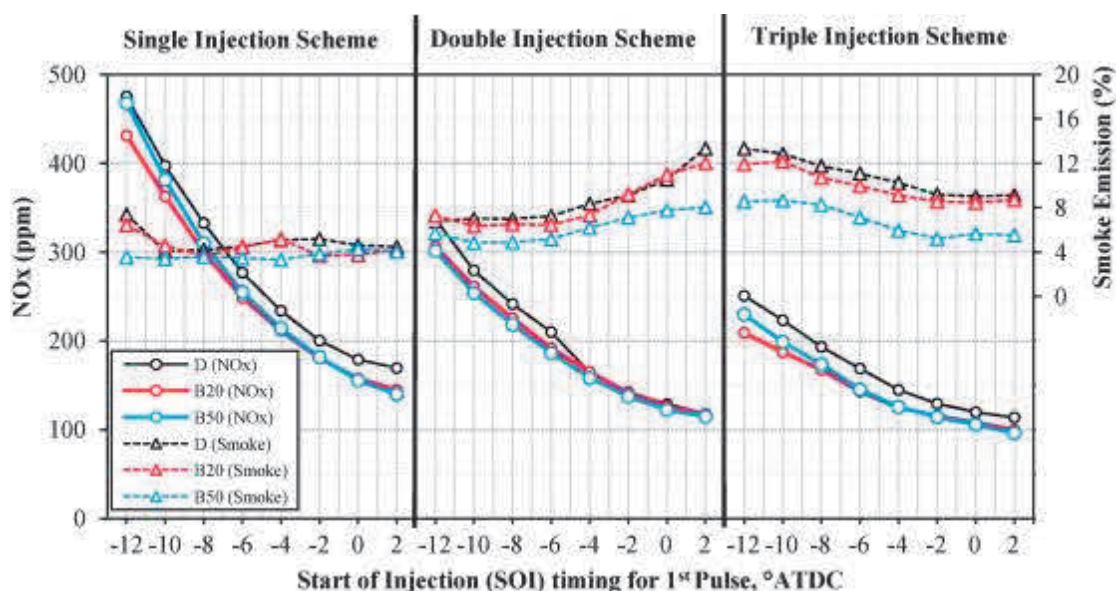
Figure 1.18 NO_x and smoke emission for various fuels, SOI timings and injection strategies [72].

Although some studies have involved split injection strategies, the effect of split injection on the fuel adhesion characteristics in the cross-flow field, which is important towards the end of the exhaust cycle, has not been studied.

1.4.3 *Spray/jet in cross-flow*

The complex physical and chemical processes within the cylinder directly impact the performance, fuel economy, and emissions of the engine, particularly the fuel spray structure, atomization, evaporation, and combustion processes, which are greatly

impacted by the flow field of the cylinder [73-78]. The simultaneous measurement of fuel concentration and velocity depicted in Figure 1.19 illustrates the strong coupling between spray momentum and air-fuel mixture [79].
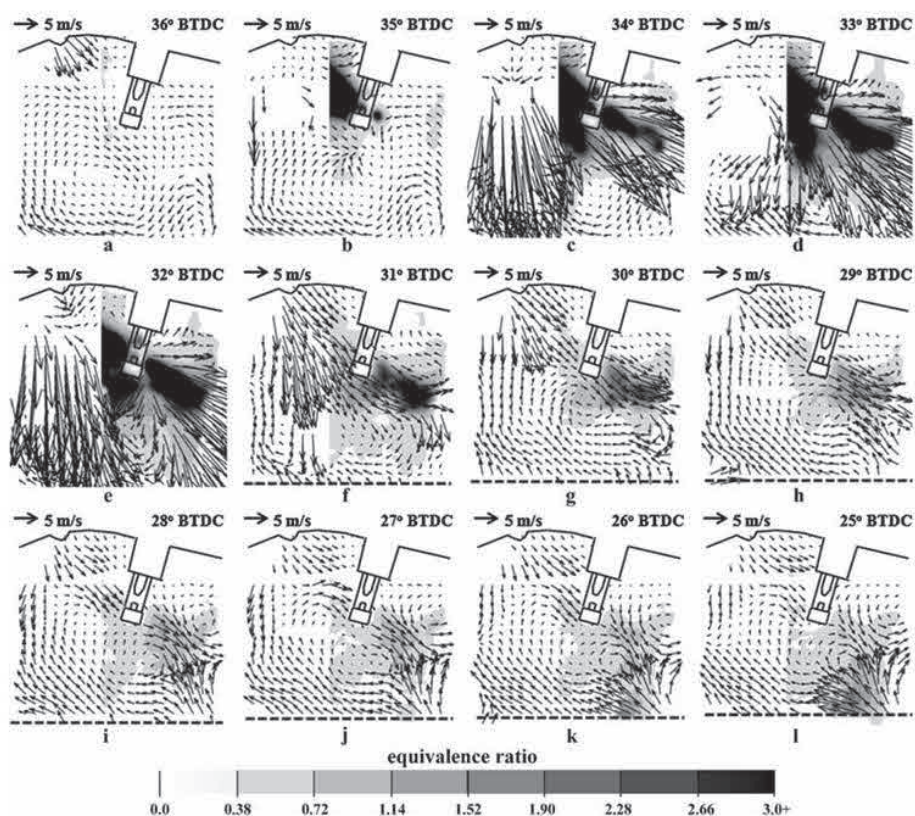
Figure 1.19 The spray and evolution of the air-fuel mixture [79]

The interaction between air and fuel injected into the engine mixes and interacts with components such as the cylinder walls and piston surfaces, directly affecting the generation and combustion of the air-fuel mixture, thus influencing engine performance [78, 80-83]. Modern direct injection gasoline engines typically employ large-scale flow field designs, such as tumble flow, swirl, or squish flow, achieved by altering the intake system and combustion chamber structure [84-87]. Additionally, turbulence is another crucial flow characteristic that promotes the exchange between unburned and burned mixtures, enhancing combustion speed [88, 89]. Optimizing the cylinder flow field can enhance fuel spray decomposition and evaporation rates, reducing the risk of knock and minimizing emissions of unburned fuel and PM. Due

to the complexity of the flow field, cross-flow is commonly used to simulate cylinder flow motion [90-93]. After a liquid jet enters a cross-flow of air, it undergoes a primary breakup to form primary liquid droplets, experiences a secondary breakup, and eventually evaporates into a vapor cloud. Simultaneously, the cross-flow causes the liquid column to bend, forming counter-rotating vortexes, resulting in the deformation of the liquid column into kidney-shaped structures. This pressure imbalance leads to structural changes, potentially inducing momentum exchange between the liquid column and the gas as shown in Figure 1.20 [94].
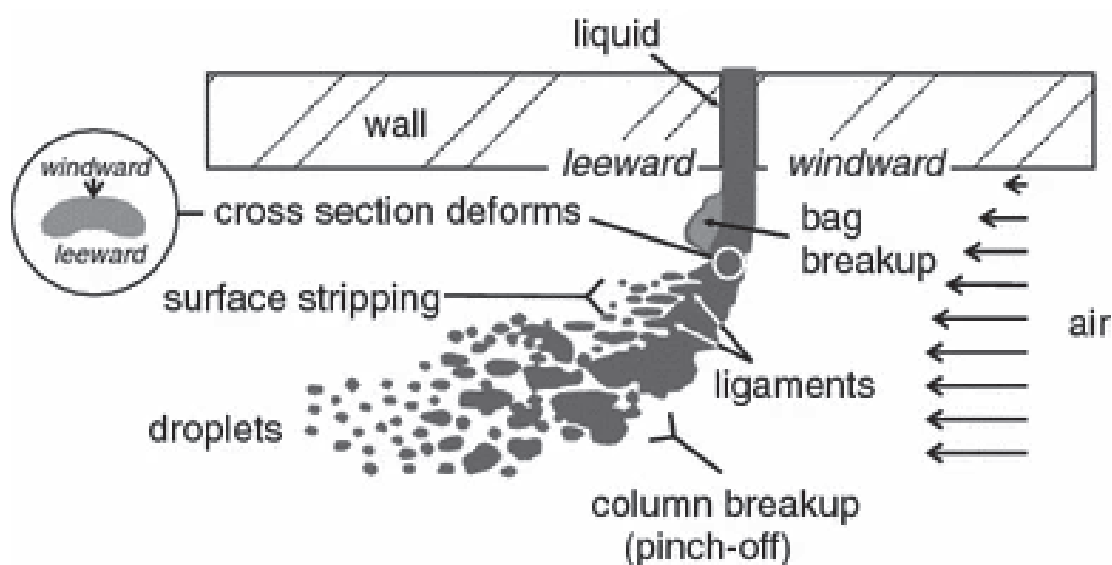
Figure 1.20 Schematic of a liquid jet issuing into a cross-flow of air [94].

The airflow movement inside the engines can promote the diffusion of fuel spray. Braun et al. examined the fuel spray characteristics with and without airflow[95]. The findings showed that the fuel spray was distributed much more extensively over the cylinder as a product of the primary breakup of the spray, which produced small droplets that were broadly distributed by the intake airflow and tumble behavior. Finally, it was proved that the engine airflow enhanced the mixture fuel spray formation. In a consistent airflow system produced by a wind tunnel, Moon et al. [96] studied the interaction between the fuel spray and air utilizing a slit injector; the results showed that the airflow pattern is related to the droplet size distribution within the spray and that optimizing the airflow and spray together is a critical factor in

influencing interaction.

Guo et al. [97, 98] observed free spray characteristics using High-Speed Video (HSV) at various ambient pressures and cross-flow velocities and then used aerodynamic equations to determine the properties of individual droplet motion. The results demonstrated the fact that at constant cross-flow velocities, the dispersion of free spray was more pronounced at low ambient pressures than at high ambient pressures. Under cross-flow conditions, the spray has more minuscule droplets on the higher leeward side, and the spray deforms proportionally to the ambient pressure. Theoretical calculations have led to the conclusion that small droplets are more affected by cross-flow. Si et al. [99, 100] investigated the effects of different cross-flow velocities and ambient pressures on the wall-impingement spray characteristic using CW laser sheet HSV and Particle Image Analysis (PIA) technology. According to the findings, the cross-flow promoted spray breakup and dispersion and led to a large wall-injection vortex phenomenon. The leeward side exhibits a larger deformity of the spray feature than the windward side, and eddy currents cause an unequal deformity of droplets in the higher portion of the leeward side. Arcoumains et al. studied the impact of a previous liquid film on the impingement spray under various cross-flow velocities [101]. The results showed that the wall film survived the two injections and became thicker at lower air velocities.

Zhang et al. [102] examined the impact of various ambient pressures and cross-flow velocities on the wall-jet vortex generated after the spray impinged on the impingement wall using laser-sheet technology; they observed that the height of the vortex core grows as the cross-flow velocity rises but decreases with ambient pressure. Zhang et al. [103] utilized the Mie scattering and RIM method to investigate wall-impingement sprays and fuel adhesion under varying cross-flow velocities. Their findings indicate that cross-flow significantly enhances fuel spray diffusion and adhesion while accelerating the volatilization of fuel adhesion. As the cross-flow velocity increased, the thickness of fuel adhesion decreased.

However, according to the current research on the fuel adhesion characteristics of wall-impingement spray, the velocity in the cross-flow field is far from sufficient, and the injection strategies should also be optimized.

1.4.4   Optical diagnostic techniques

Optical diagnostic techniques play a crucial role in assessing fuel injection, evaporation, and combustion processes within Internal Combustion Engines (ICEs). Due to the high velocity of sprays and the transparent nature of fuels, direct observation is challenging. These techniques enable the measurement of cylinder parameters at various scales to monitor the evolution of sprays. The comprehensive application of these methods provides extensive spray information, particularly in the widespread study of gasoline sprays and fuel film. This aids researchers in better understanding the structure, motion, and evaporation characteristics of sprays, thereby optimizing internal combustion engine performance and emissions.

In spray research, light scattering is a significant phenomenon. In most cases, scattering is caused by Rayleigh scattering, primarily originating from molecules or very small liquid droplets, whose sizes are typically smaller than the wavelength of light or approximately equal to one-tenth of the wavelength. However, when the droplet size equals or exceeds the wavelength of light, Mie scattering occurs. Due to the relatively small wavelength of light, Mie scattering predominates in non-evaporating spray visualization experiments. Nonetheless, Mie scattering is limited in accurately analyzing droplet diameter and concentration. Consequently, this method is commonly employed to capture spray structure and liquid phase penetration phenomena, rather than for precise measurements of droplet diameter and concentration [104-106].

According to scattering behavior, photons can be divided into three types: ballistic photons, snake photons, and diffuse photons. Ballistic photons travel in a straight line without scattering, preserving undistorted information about embedded structures.

Snake photons scatter once or twice, retaining slightly distorted information. Diffuse photons scatter multiple times, thus reducing image quality. By collecting ballistic photons and snake photons, clear images of the liquid-gas interface and primary liquid droplets can be obtained. Linne et al. [107, 108] utilized ballistic imaging technology to capture instantaneous images of liquid nuclei in atomized sprays, a method that is remarkably impressive. Figure 1.21 shows the schematic of the ballistic imaging system. However, this technique's limited dynamic range may affect the accurate observation of liquid nucleus behavior. They employed a time-gated ballistic imaging instrument and successfully captured the transient breakup of single-hole atomized diesel fuel sprays in the core region of the atmosphere. These images depicted characteristics of periodic behavior, cavitation, and entrainment processes. Two-photon absorption or excitation is a nonlinear process described by Maria Göppert-Mayer's hypothesis and empirically validated with the introduction of lasers. When the energy of two incident photons equals the energy difference between two quantum states, an electron in an atom can be excited from the ground state to the excited state [109]. Berrocal et al. [110] utilized Two-Photon Excitation Laser-Induced Fluorescence (2p-LIF) technique to image the single spray plume of a commercial GDI system with six holes operating at 200 bar injection pressure.
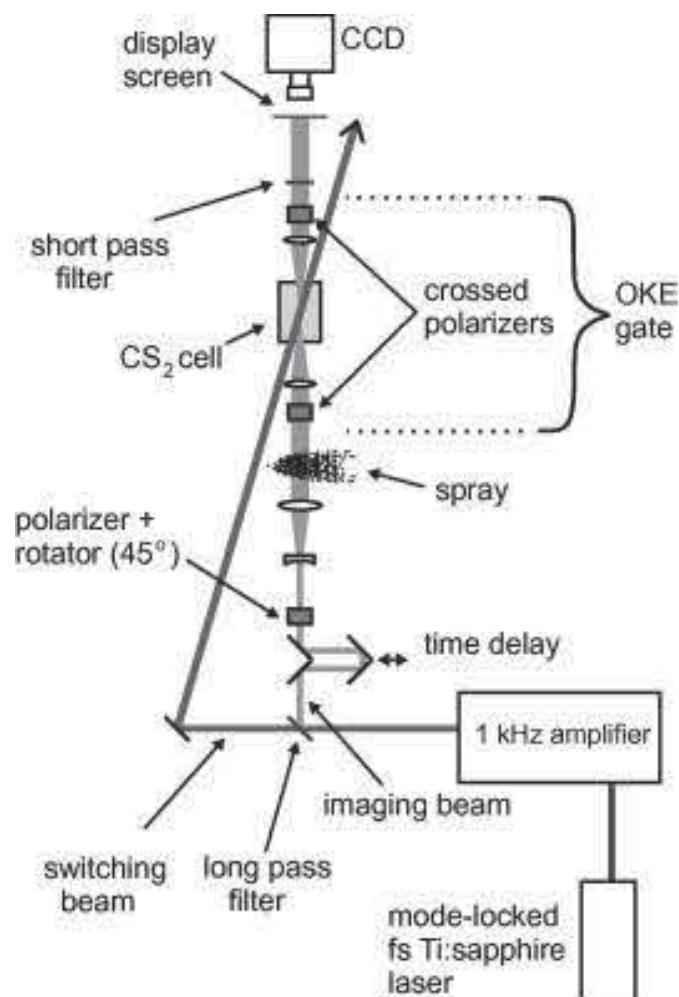
Figure 1.21 Schematic of the ballistic imaging system [107].

Drake et al. [22, 111] developed an optical method, known as the RIM method, for quantitatively studying the fuel adhesion on the pistons of direct injection gasoline engines. Due to the disparate refractive indices of quartz (1.46) and air (1.0), light undergoes scattering on the surface of the sheet, making it appear brighter. However, when fuel adheres to the sheet's surface, the similarity in refractive indices between the fuel (ranging from 1.43 to 1.49) and quartz (1.46) leads to a reduction in scattered light, causing the sheet to appear darker. Consequently, different light intensities result in varying thicknesses of fuel adhesion.

Luo et al. [49] used the RIM method to investigate the impact of ambient temperature, and ambient pressure/ injection pressure on fuel adhesion characteristics. The findings of this study indicated that when the ambient temperature was relatively high, the thin

fuel adhesion evaporated rapidly; however, the thick fuel adhesion hardly evaporated, resulting in more uniform fuel adhesion on the wall. Parks et al. [112] employed Laser-Induced Fluorescence (LIF) spectroscopy to measure the concentration of fuel absorbed in the oil film on the cylinder walls of tiny internal combustion engines.

Uchida et al. [113] utilized the LIF method to elaborate on the impact behavior of fuel spray on the oil film. The research revealed significant differences in the impact behavior of fuel droplets on the oil film, which are influenced by factors such as the Weber number (We), oil viscosity, oil temperature, and oil film thickness. Wang et al. [114] used the LIF method to quantitatively study the characteristics of fuel film deposition on dry and viscous surfaces. The study findings indicated that compared to dry surfaces, pre-existing oil films often result in the formation of smaller, thicker deposited fuel films. The schematic diagram of the LIF optical system is shown in Figure 1.22.
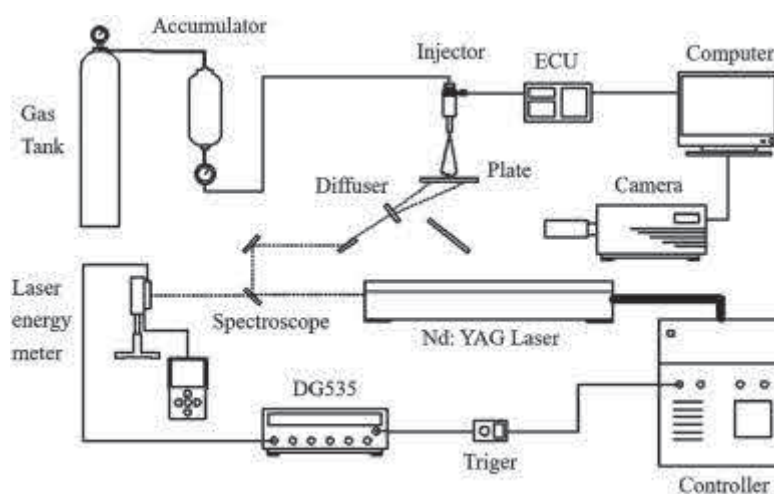
Figure 1.22 LIF optical system [114].

Optical flow is a method used to compute the velocity vector of each pixel in a digital image, with one velocity vector assigned to each pixel. By calculating a denser set of vectors, additional frequency content can be recovered. Schmidt et al. [115-117] research indicate that their use of Wavelet-Based Optical Flow Velocity (wOFV) can significantly distinguish higher spatial frequencies in both synthetic and experimental

non-reactive turbulent flow datasets. Particularly, when evaluating synthetic particle images generated from direct numerical simulations of incompressible turbulence, they found that the current wOFV method provides more accurate velocity estimates compared to methods based on cross-correlation.

PIV technique is a laser measurement technique used to measure fluid velocity fields. It captures spatial distribution images of particles in the flow field within an extremely short period and utilizes these images to calculate the velocity and direction of particles over a certain time interval. Unlike tracking individual particle trajectories, PIV technique divides the particle images captured by the camera into multiple sub-regions called "interrogation windows," and then employs cross-correlation algorithms to compute the displacement and direction of all particles within each interrogation window [118, 119].
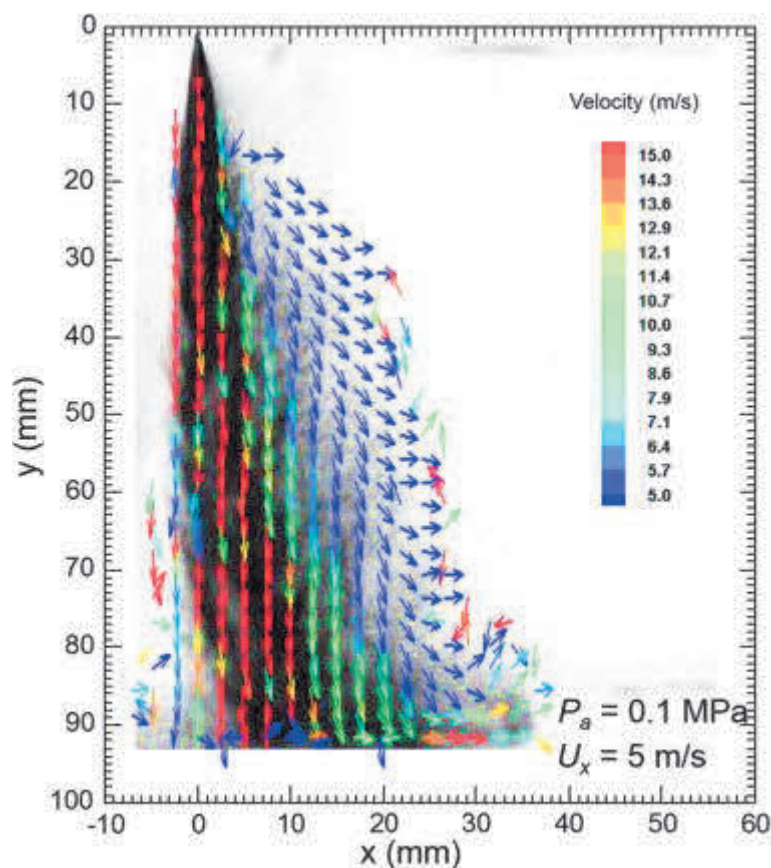
Figure 1.23 Spray velocity flow field distribution [97].

Guo et al. [97] utilized high-speed photography and PIV technique to observe fuel

spray and measure its velocity distribution. As environmental pressure increases, the curved spray profile is compressed. With the increase in environmental pressure, the velocity distribution of the fuel injection becomes more uniform; additionally, the magnitude of the vertical velocity can exceed the lateral velocity. Figure 1.23 shows the spray velocity flow field distribution.

1.5 Summary

This chapter begins by introducing the background and motivation of the study, which focuses on global concerns about energy and the environment. With the increasing consumption of energy, traditional sources are depleting, exacerbating the trend of climate change. Given the significant role of the transportation industry in energy consumption and emissions of harmful gases, enhancing energy efficiency is crucial.

Next, review the formation of the fuel-air mixture in DISI engines. While DISI technology has improved fuel efficiency in gasoline engines, further improvements are necessary to control energy consumption and emissions. The characteristics of spray and fuel adhesion are crucial for fuel combustion.

Finally, summarize the research progress in split spray, cross-flow, and spray optical diagnostics. Under the split injection strategy condition, the impact of wall impingement distance and cross-flow velocity on impinging spray and fuel adhesion has been largely overlooked. Through an analysis of optical diagnostic techniques, this study will utilize PIV technique to analyze velocity field distribution, employ continuous wave laser-Mie scattering technique to observe spray structure on vertical planes and utilize RIM method to observe fuel adhesion characteristics.

CHAPTER 2 EXPERIMENTAL APPARATUS AND PROCEDURE

2.1 Experimental Setup

2.1.1 High-pressure wind tunnel

The method of using a loop wind tunnel, as described by Tajima et al.[120], can provide airflow at high pressure, but its complex structure and high cost are one of the main problems in airflow experiments. In addition to loop wind tunnels, another method of obtaining air flow in high-pressure environments is to use pressure tanks. The schematic diagram is shown in Figure 2.1. The specific operations are as follows：

Storing Compressed Air: Compressed air is stored in a pressure vessel, ensuring that the pressure inside the vessel exceeds atmospheric pressure.

Valve Adjustment: Valve 2 is kept partially open to control the release of airflow. When experimentation is required, Valve 1 is opened, allowing compressed air to enter the observation chamber. This leads to a rapid increase in pressure inside the chamber, accompanied by observable changes in velocity. The pressure inside the observation chamber is maintained at the desired stable state by adjusting the throttling of Valve 2 and replenishing the pressure vessel as necessary, preventing rapid fluctuations in atmospheric pressure.

When the velocity and pressure within the observation chamber meet the experimental criteria, measurements can be triggered through a responsive control system, facilitating data collection and analysis.
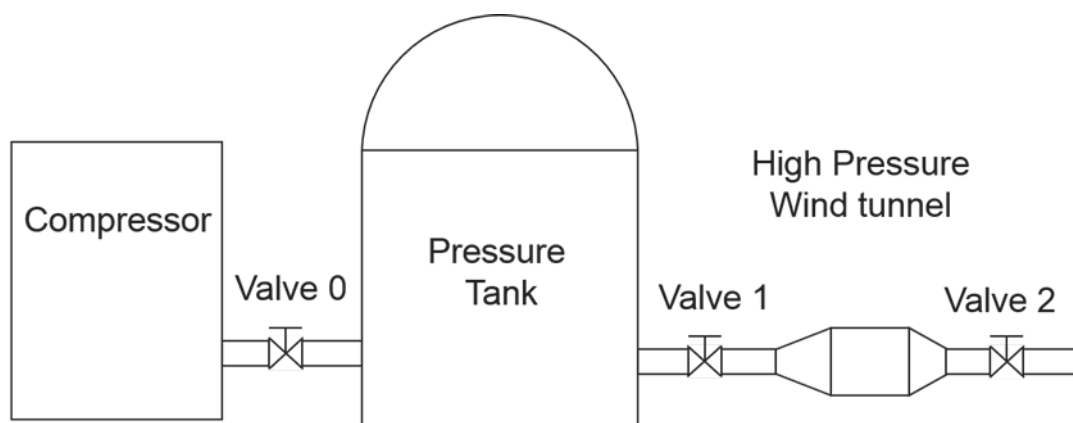
Figure 2.1 Schematic of cross-flow wind tunnel system.

2.1.2 Experiment platform

This experimental setup provides a uniform cross-flow field through a wind tunnel to investigate the wall-impingement spray behavior and fuel adhesion characteristics under cross-flow field conditions. The cross-flow wind tunnel and observation chamber are illustrated in Figure 2.2. The wind tunnel consisted of diffusion, rectification, contraction, and observation sections. Guide vanes and a mesh screen were installed in the rectification section to reduce the flow turbulence and eddies and thereby ensure a smoother and more uniform cross-flow field. The wind tunnel adjusts the opening angle of valve 1 to control the airflow velocity, thereby providing uniform transverse flow at different velocities for the downstream observation chamber [97, 98].
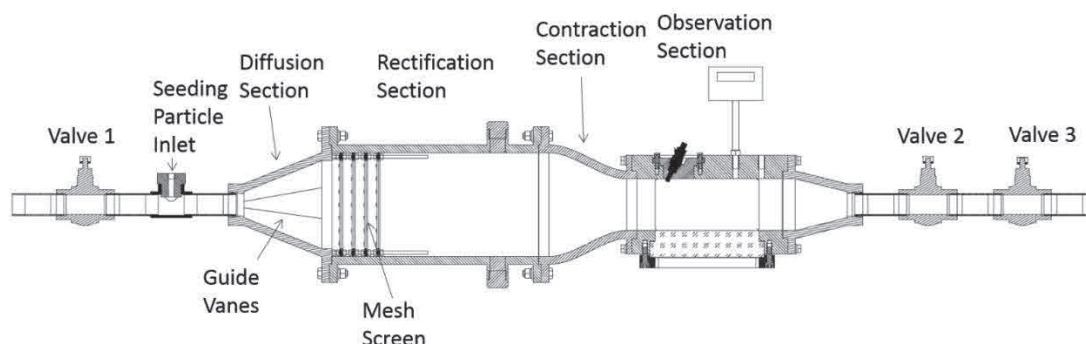
Figure 2.2 Experiment platform.

The front, back, and bottom optical windows of the observation chamber were made

of Pyrex with dimensions of 200 mm × 100 mm× 100 mm. As shown in Figure 2.3, a single-hole injector (whose injection direction of the injector is 90° to cross-flow), pressure sensor (for real-time monitoring of the chamber pressure), and hot-wire anemometer (simultaneously monitored cross-flow velocity) were sequentially installed in the ceiling of the observation chamber. The spray is injected perpendicular to the cross-flow direction. The nozzle was the coordinate origin O, with the x-axis parallel to the cross-flow, the y-axis parallel to the injector installation, and the z-axis perpendicular to the injector installation and cross-flow. In engine research, metallic surfaces are typically used as the impingement pact inner walls, with a surface roughness of approximately Ra 1.0 μm (arithmetic mean deviation of the profile) on the piston surface. However, due to the accumulation of deposits, the roughness may increase to Ra 10.0 μm or higher [49, 52]. For visualization, the metallic impingement wall was replaced with quartz glass in this study. Therefore, it was expected that substituting a quartz glass plate for a metallic impingement wall would not cause significant differences in the experimental results. A quartz glass plate of size 125 mm × 70 mm was installed horizontally 25, 50, and 75 mm below the injector tip inside the observation chamber to observe the wall-impingement spray and fuel adhesion characteristics. The flat-wall was manufactured with a surface roughness of 7.7 μm.
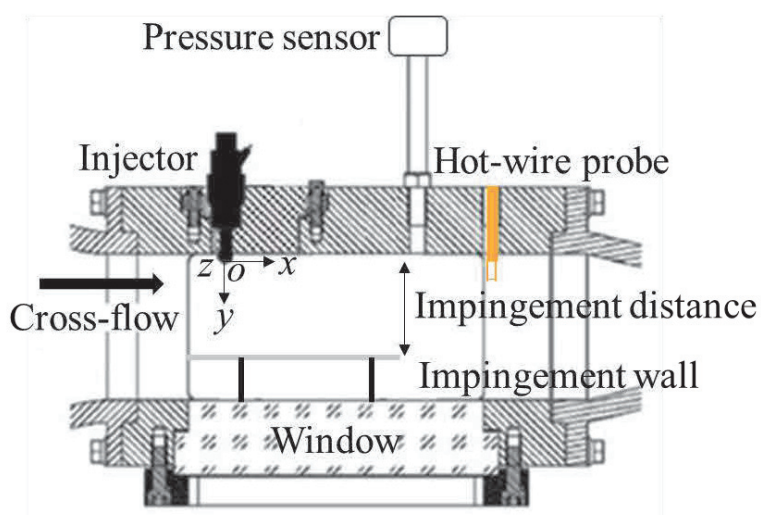
Figure 2.3 observation chamber.

2.2 Control System

High-pressure wind tunnel experiments are typically conducted under specific experimental conditions, where ambient pressure and cross-flow velocity are crucial parameters. In the observation chamber, the experiment is triggered only when both of these parameters simultaneously meet the requirements for the experiment.
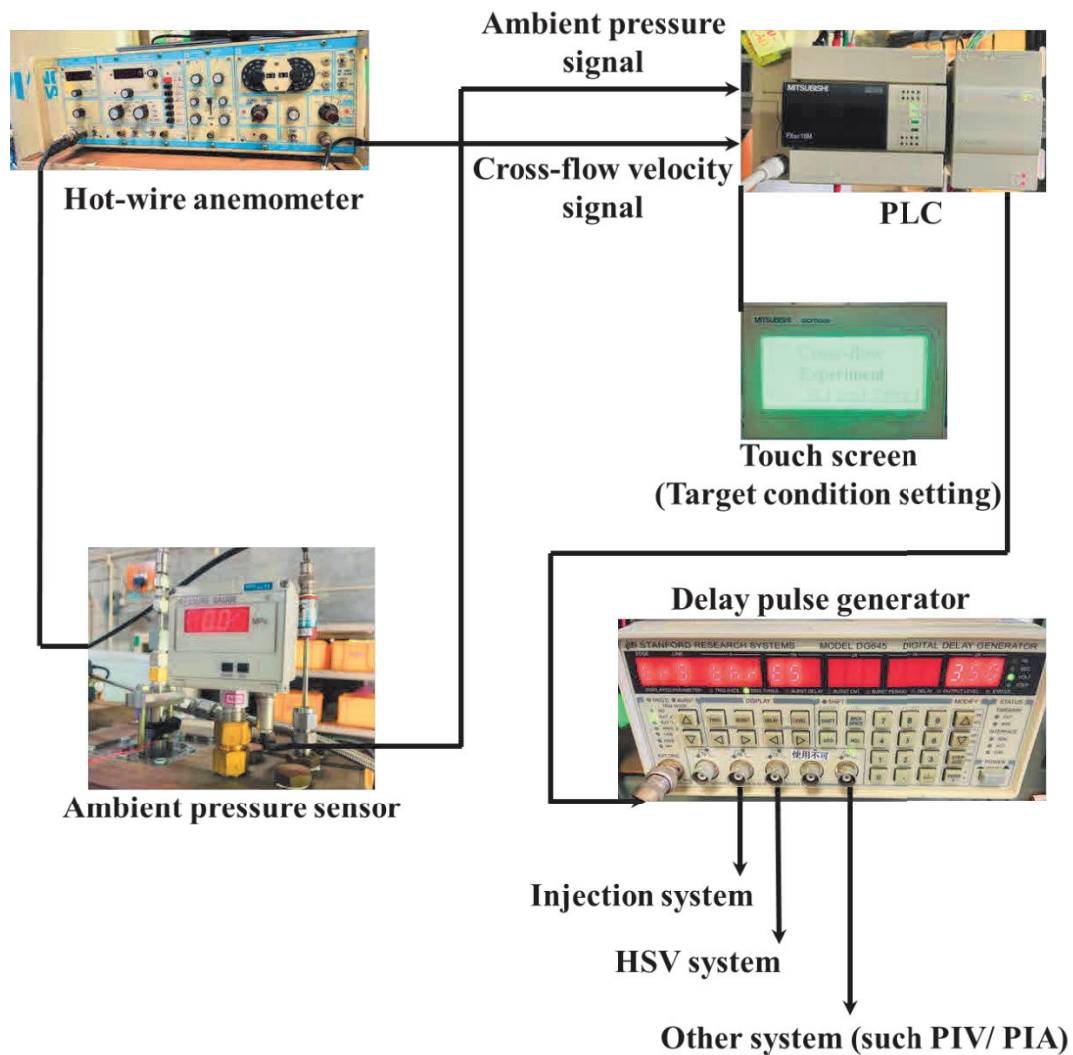
Figure 2.4 Control system for high-pressure wind tunnel.

To ensure swift responses to pressure and velocity fluctuations, this control system strategically employs boasting a response time of under 1 ms, a pressure sensor, NSK (GC75243), alongside a hot-wire anemometer, KANOMAX 0251R-T5, and they are simultaneously tasked with detecting pressure and velocity signals. Analog signals

from both the pressure sensor and anemometer undergo conversion into digital signals through Mitsubishi's analog-to-digital converter (FX3U-4AD), thereafter routed to the Programmable Logic Controller (PLC, Mitsubishi, FX3U-16MR/ES). Through meticulous programming, the PLC meticulously compares these signals. Facilitating user interaction, the system interface integrates Mitsubishi's touch screen (GT1020-LWD), offering a real-time display of pressure and velocity values alongside operational functionalities. An experimental framework is meticulously crafted within the touchscreen interface. Upon meeting predefined experimental criteria, the PLC promptly issues a pulse signal. This pulse, seamlessly received by the pulse generator, orchestrates control over injection systems, high-speed cameras, and PIV systems. Figure 2.4 shows control system for high-pressure wind tunnel. Recognizing the challenges posed by fluctuating ambient pressure in confined spaces, the experiment adopts an intrusive method for cross-flow velocity measurement.

The mechanical anemometer utilizes cups or blades to convert wind velocity into electrical signals, but the airflow field is affected post-measurement. The Pitot tube anemometer is a pressure-based wind velocity measurement device, but it faces issues with response time and involves a complex transmission process [121]. The hot-wire anemometer measures the rate at which heat transfers from a heated filament to the airflow, for the measurement of wind velocity and turbulence, with its probe typically made of platinum or tungsten[122-124], as shown in Figure 2.5. The hot-wire anemometer was chosen for this study due to its response time of less than 1 ms and its immunity to pressure variations. The hot-wire probe was installed at the center of the observation room because at this position, the wind velocity is relatively stable, and there is less turbulence. This helps to ensure accurate measurement results.
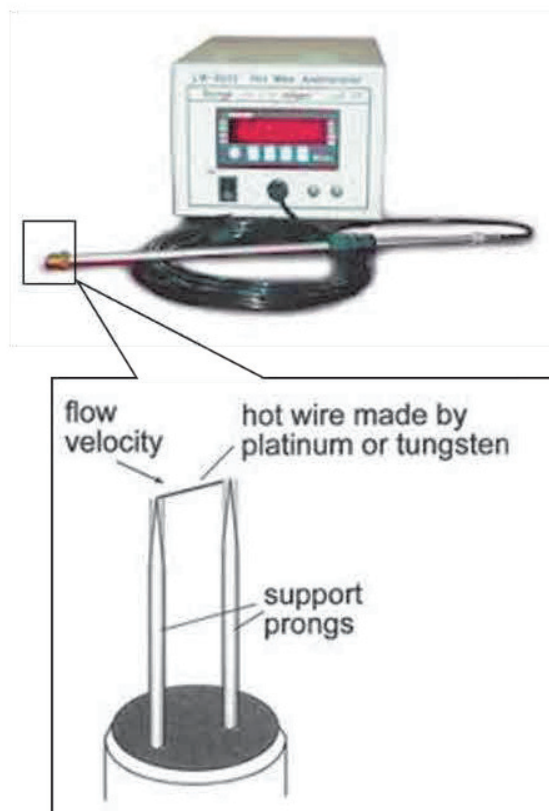
Figure 2.5 Typical Anemometers.

By adjusting the valves 1 and 2 of the wind tunnel, it is possible to achieve cross-flow at different velocities and ambient pressures. Initially, valve 2 is kept at a fixed opening (61°), and valve 1 is closed. Then, valve 1 is opened to induce the cross-flow. During this process, when valve 1 is opened, the ambient pressure rapidly increases and then gradually decreases. Finally, the Electronic Control Unit (ECU) and HSV camera are actuated when the ambient pressure and cross-flow velocity reach the predetermined thresholds. The timing of valve 1, cross-flow velocity, ambient pressure, camera, and injection trigger is exhibited with ambient pressure P_a=0.4 MPa and cross-flow velocity U_x=5 m/s, as seen in Figure 2.6.
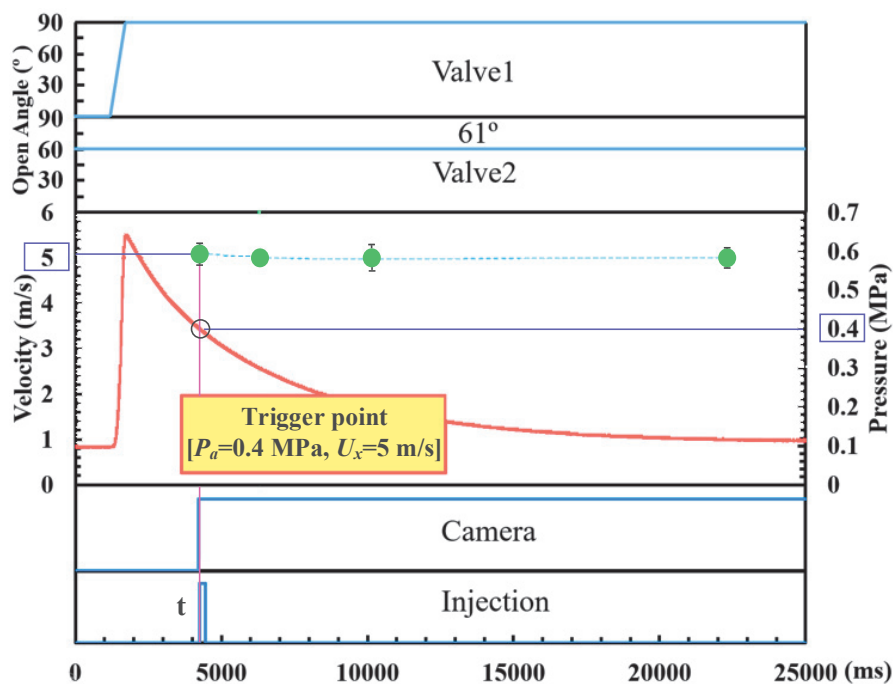
Figure 2.6 Example condition for trigger.

2.3 Fuel Supply System

The injection system comprises a high-pressure Nitrogen (N_2) tank, an accumulator, an injector driver, an injector, a computer, and a delay generator, as in Figure 2.7. The experiment employs a 0.15 mm-diameter single-hole injector. The operational procedure is as follows: Firstly, set the parameters of the injector driver and the delay generator. Secondly, open the valve of the high-pressure N_2 tank to supply the injector with the preset pressure. Finally, under the control of the delay generator, fuel is injected for the experiment.

Despite gasoline being used in actual engines, Researchers commonly employ gasoline surrogates in experiments and evaluations to limit the intricate chemical and physical properties of the gasoline, thereby simplifying the research process and yielding clearer experimental results. Normal heptane, iso-octane, and toluene are commonly employed as gasoline surrogates. In this experiment, toluene was employed as a substitute fuel because it is the most common aromatic compound found in gasoline [125, 126]. The experiments were conducted at room temperature

and atmospheric pressure, with the injection pressure maintained at a constant 10 MPa. Experiments were conducted three times under each experiment condition, with the calculation of the average value and standard deviation of the data. The standard deviation values were denoted as error bars in this work.
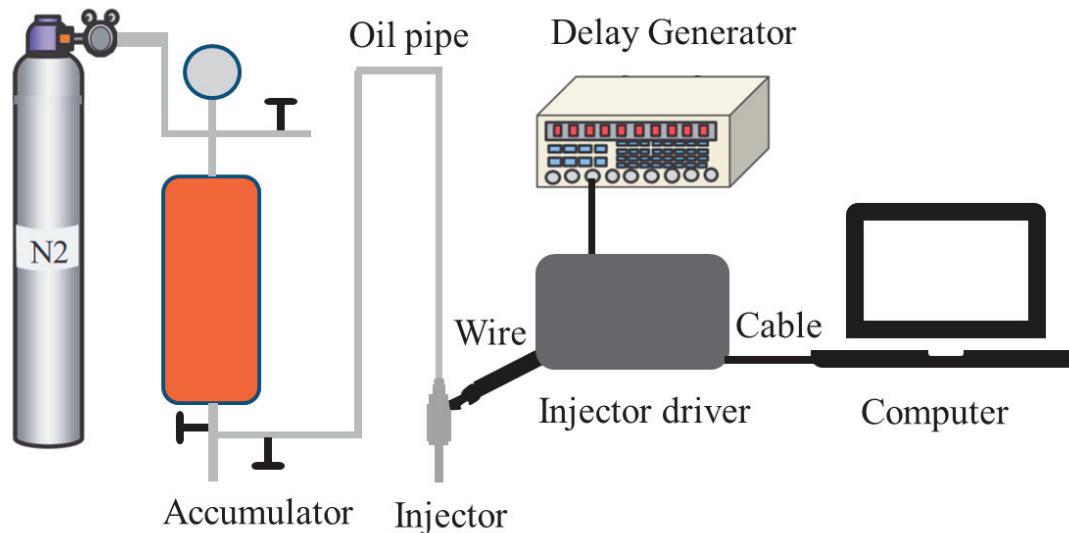
Figure 2.7 Apparatus arrangement diagram of fuel supply system.

2.4 Optical Measurement Methods

The PIV technique is utilized to assess cross-flow field uniformity at different velocities, providing insights into the influence of cross-flow on fuel adhesion and spray dispersion. The continuous wave laser-Mie scattering technique was constructed using a high-speed camera and laser sheet light to observe the wall-impingement spray structure in the vertical plane. The fuel adhesion characteristics of the wall spray were examined using the RIM method.

2.4.1 PIV (Particle Image Velocimetry)

This study utilized a PIV system (Seika Corp., 2D PIV system) to measure the flow field uniformity at different cross-flow velocities. A Charge-Coupled Device (CCD) camera (PCO Inc., PCO1600) was positioned directly in front of the observation chamber. A dual-pulse Nd:YAG laser (New Wave Research Corp., DPIV-N50)

generated a laser sheet (1 mm thick, 532 nm wavelength) parallel to the crossflow direction. Mirrors were used to adjust the angle of the laser sheet so that it was parallel to the vertical plane. The laser sheet illuminated the tracers (olive oil) in the observation chamber [97, 102]. The tracers were introduced through a particle inlet and flowed into the observation chamber via crossflow. The interval between the dual pulses was 40 μs. The detailed optical setup is shown in Figure 2.8.
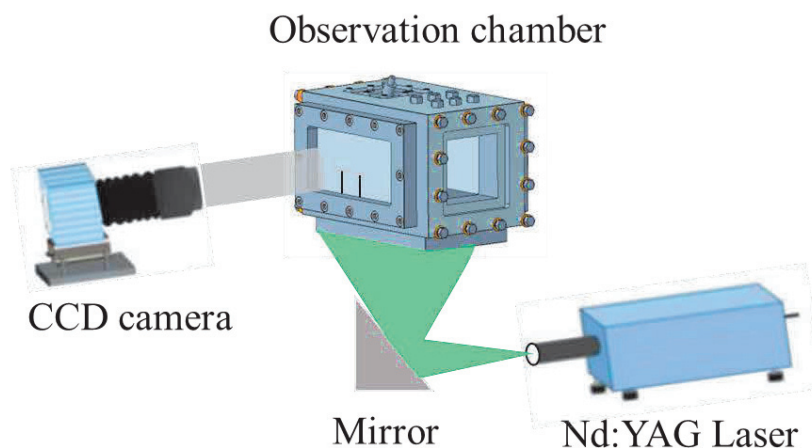
Figure 2.8 Optical arrangement for PIV.

Uniform cross-flow field

The PIV technique was used to monitor the uniformity of the cross-flow field. The PIV technique captures the motion of tracer particles in a flow field to obtain velocity information. By analyzing the particle image sequence, the velocity vectors at different locations were calculated, and the direction and magnitude of the velocity vector in the cross-flow field were displayed using a vector distribution diagram, allowing for further investigation of the flow field characteristics and uniformity. Figure 2.9 shows the cross-flow velocity vector distribution diagrams. The velocity data extracted from positions x = 0 mm and x = 60 mm are also presented in Figure 2.9. Comparing and analyzing the velocity distributions at different positions allows for the assessment of the uniformity of the cross-flow field on the x-axis. The results indicate that the velocity vector distribution is stable.
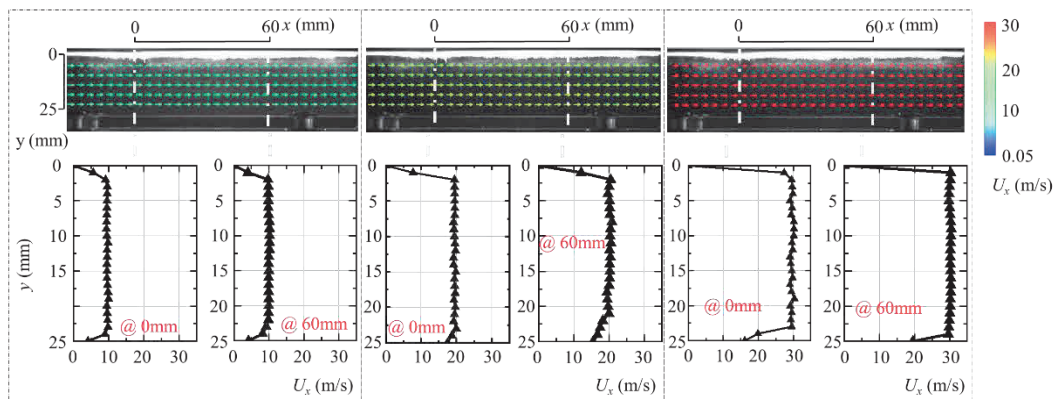
(a) D_{imp}=25mm
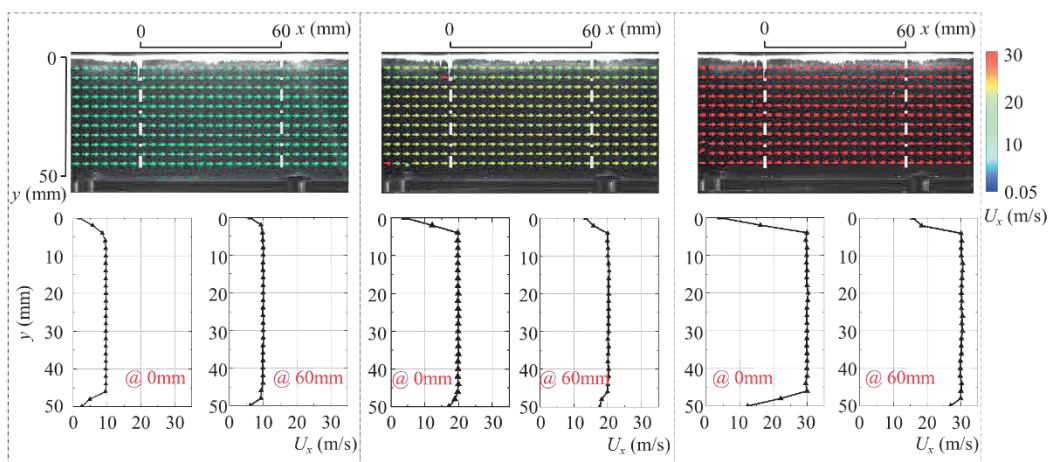
(b) D_{imp}=50mm
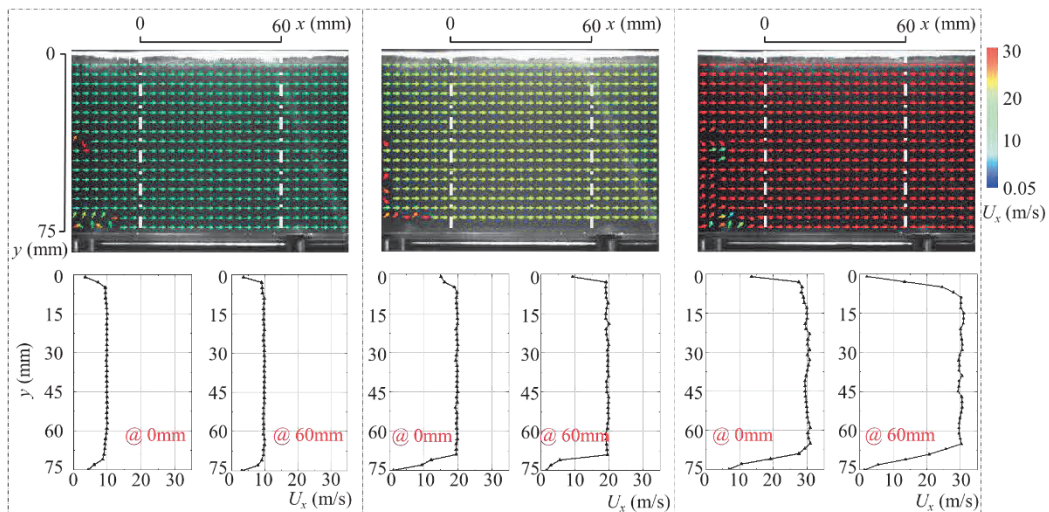
(c) D_{imp}=75mm

Figure 2.9 Velocity distributions of cross-flow field inside observation chamber.

2.4.2   Continuous Wave Laser-Mie Scattering Technique

The continuous wave laser-Mie scattering technique observe the wall-impingement spray structure in the vertical plane. The source of a 2 mm thick Continuous Wave (CW) laser (DPGL-2W, Japan Laser Corp.) sheet was used at the bottom of the observation chamber, and its emitted laser beam interacted with the particles in the spray, causing them to scatter a portion of the incident light. An HSV (Photron FASTCAM SA-Z) was positioned directly in front of the observation chamber to capture the developmental morphology of the spray from a lateral perspective. The optical arrangement for continuous wave laser-Mie scattering technique is shown in Figure 2.10. The detailed photography condition of continuous wave laser-Mie scattering technique is shown in Table 2.1.
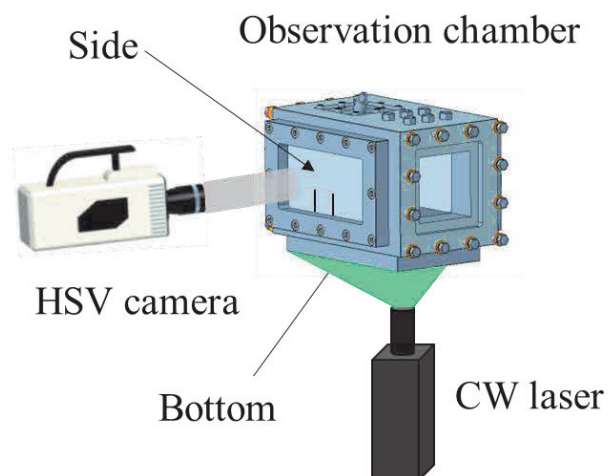
Figure 2.10 Optical arrangement for continuous wave laser-Mie scattering technique.

Table 2.1 Photography condition.

Photography condition			
Impingement distance D_{imp} [mm]	25	50	75
Frame rate [fps]	10000	10000	10000
Frame size [pixels]	1152×560	1024×520	1024×520
Spatial resolution [pixels/mm]	5.3	5.3	5.3

2.4.3   RIM (Refractive Index Matching)

The optical system configuration of the RIM experiment for measuring the fuel adhesion distribution of the wall-impinging spray is shown in Figure 2.11. The HSV camera (Photron FASTCAM SA-Z) was positioned directly beneath the observation chamber. A Light Emitting Diode (LED) (Altec, LLBK1-LAW-0001) light was placed diagonally beneath the observation chamber. The detailed photography condition is shown in Table 2.2.
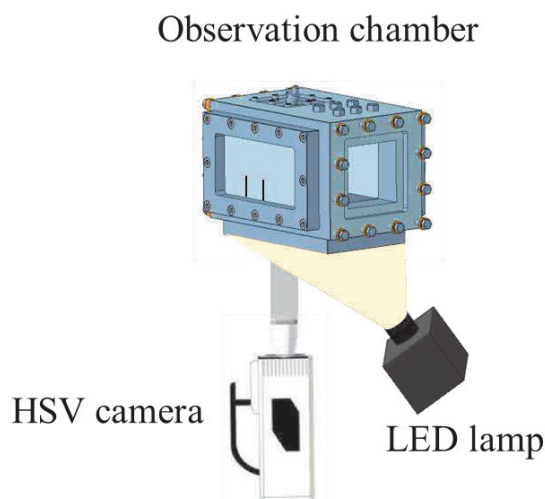
Figure 2.11 Optical system arrangement for RIM.

Table 2.2 Photography condition.

Photography condition			
Impingement distance D_{imp} [mm]	25	50	75
Frame rate [fps]	10000	10000	10000
Frame size [pixels]	960 × 448	960 × 448	960 × 448
Spatial resolution [pixels/mm]	9.6	10.2	10.7

RIM principle and calibration

Drake et al. [22] studied the correlation between fuel adhesion thickness and transmittance. The refractive index of the quartz glass plate (1.46) differs significantly from that of air (1) but closely matches that of the gasoline fuel (1.43-1.49). When the fuel no attaches to the plate, the significant refractive index difference between air and quartz glass leads to a reduction in the transmitted light and an increase in scattered light, resulting in a brighter wall in the captured images. Conversely, when the fuel attaches to the plate, the fuel and quartz glass have similar refractive indexes. This results in an increase in the transmitted light and a decrease in the scattered light, causing the captured images to appear darker on the wall. The transmitted light intensity was inversely proportional to the fuel adhesion thickness. The RIM principle is illustrated in Figure 2.12.
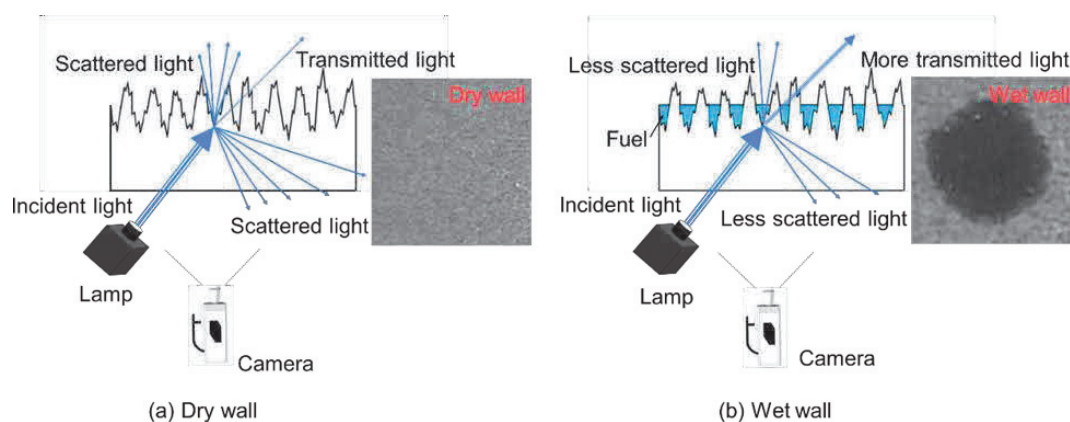
Figure 2.12 RIM principle.

In this study, The RIM method was employed to quantify the distribution of the fuel adhesion characteristics. I_{dry} (x, y) is the surface brightness of a dry quartz flat-wall, and I_{wet} (x, y) is the surface brightness of a wet quartz flat-wall after fuel adhesion. The change in transmittance ΔI (x, y) is described by Equation (1).

$$\Delta I(\mathrm{x}, \mathrm{y}) = \left[1 - \frac{I_{dry}(\mathrm{x}, \mathrm{y})}{I_{wet}(\mathrm{x}, \mathrm{y})}\right] \times 100\% \qquad (1)$$

The change in transmittance is induced by fuel adhesion, based on the RIM method principle; hence, the transmittance ΔI (x, y) is calculated as a function of the fuel adhesion thickness h (x, y).

$$h(\mathrm{x}, \mathrm{y}) = f[\Delta I(\mathrm{x}, \mathrm{y})] \qquad (2)$$

According to the RIM experimental principle [47, 127], the function "f" is affected by the arrangement of the optical system and upper surface roughness of the quartz glass. Therefore, calibrating the functional relationship between the transmittance and fuel adhesion thickness is essential.

Atmospheric pressure and room temperature were applied in the calibration experiments. Toluene and tridecane were combined in the ratio of 9:1. A microliter syringe was used to inject the fuel mixture onto the surface of the flat quartz wall instead of an injector system. Because the refractive indices are approximated to quartz glass, the employment of the two fuel mixtures, which are toluene with high volatility but low viscosity and tridecane with low volatility but high viscosity, would produce uniform fuel adhesion [103]. All fuel adhesion characteristics were recorded using the HSV camera.

The calibration process is depicted in Figure 2.13 and can be divided into several stages.

I) Brightness stabilization stage: When the mixture fuel does not adhere to the flat-wall surface, the brightness of the dry wall is stable, $\Delta I = 0$.

II) Mixture fuel adhesion and diffusion stage: Surface tension forces the fuel mixture

to diffuse rapidly when the fuel comes into an interface with a flat-wall, producing a phenomenon called fuel adhesion. The brightness of the scattered light transmitted rapidly increased through the flat-wall, which caused a dramatic decrease in the average brightness and a significant increase in ΔI.

III) Toluene evaporation stage: The light component, toluene, was the first to evaporate. Consequently, with the increase in the average brightness and scattered light intensity, ΔI drops quickly.

IV) Tridecane evaporation stage: The rate of increase in average brightness reduces followed by a slight decrease in ΔI until complete evaporation of the droplet. This stage illustrates the process by which the tridecane heavy component evaporates.

The calibration points images for these two distinct boundary point evaporation stages, III) and IV), were collected, and then Equation (1) was applied to calculate ΔI (x, y). The volume of the tridecane corresponded to the matching fuel value. In addition, the fuel adhesion area was measured. The average fuel adhesion thickness h (x, y) can be derived by assuming that the fuel adhesion thickness is uniform at this moment.
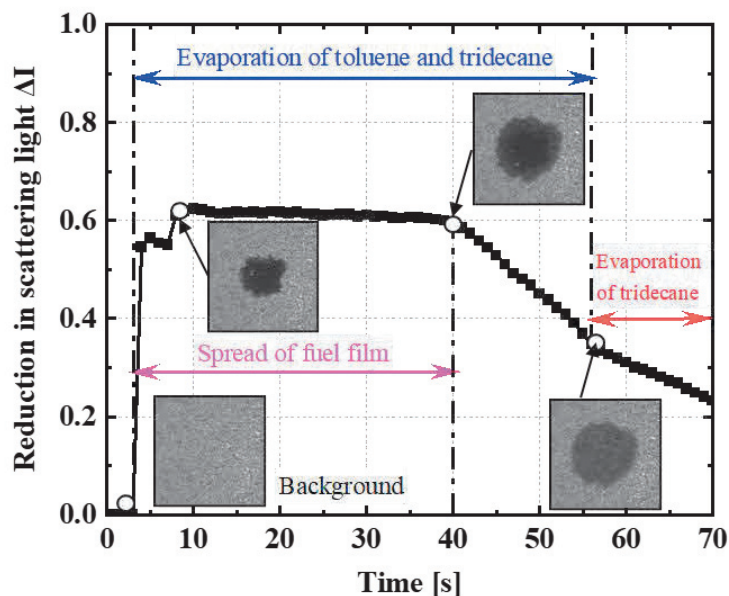
Figure 2.13 Calibration principle.

The RIM calibration experiments used a fuel blend consisting of 90% toluene (high volatility and low viscosity fuel) [128] and 10% tridecane (low volatility and high viscosity fuel) [129]. The volatility (expressed as vapor pressure) and viscosity of Tridecane and Toluene at 25°C are shown in Table 2.3.

Table 2.3 Fuel properties.

Fuel	Toluene	Tridecane
Vapor pressure	28.4 mm Hg	0.0375 mm Hg
Viscosity	0.560 mPa·s	1.724 mPa • s

The experiments involved varying the fuel volumes to 0.1, 0.2, 0.4, 0.8, 1, 2, 3, 4, and 5 ml. Each experiment was repeated three times. The critical points during the toluene-based fuel and tridecane volatilization stages were selected as the calibration data. Calibration curves were derived by fitting the calibration data obtained for each condition. The fuel adhesion thickness h is the vertical axis, and the horizontal axis represents the scattered light ΔI. Based on the RIM method, the fuel adhesion thickness can be calculated after calibration. As a result, the fuel adhesion thickness is derived as a function of light transmission ΔI. Since three impingement distances were studied, the RIM optical system arrangement was changed three times and thus there are three calibration curves. The black, red, and blue curves represent the calibration curves with impingement distances of 25, 50, and 75 mm, respectively. Further information regarding the calibration curve is displayed in Figure 2.14.
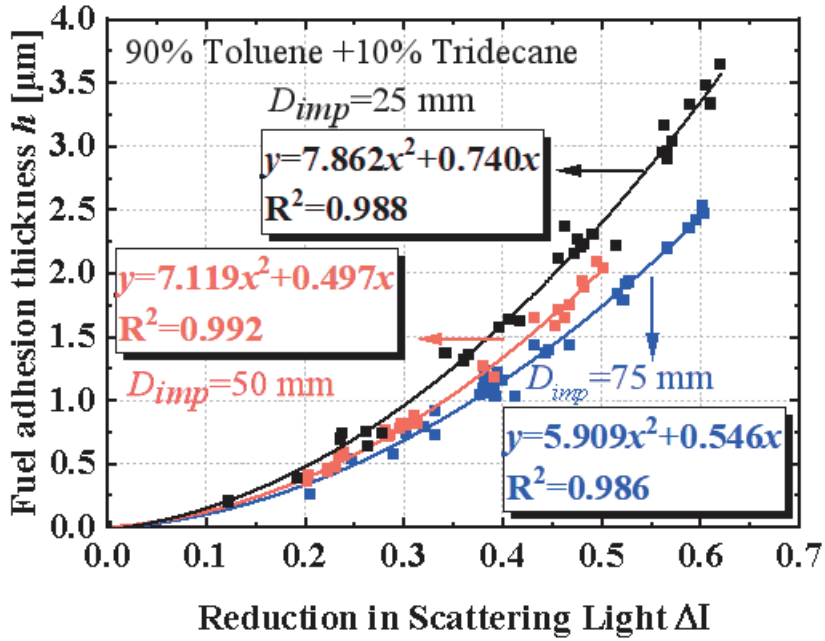
Figure 2.14 Calibration curve.

This research defines the early stage as 0 to 10 ms and the later stage as 10 to 100 ms. During the experimental analysis, after the fuel adhered to the flat wall, a white region appeared. Due to Mie scattering above the flat wall, not all figures can be used. Because of the limitations of the RIM method, we apply it only during the RIM available times in both the early and later stages. Figure 2.15 shows the measurable periods for fuel adhesion observation. Black, blue, and red represent the measurable periods for 25 mm, 50 mm, and 75 mm RIM distances, respectively. Since three impingement distances were studied, the RIM optical system was adjusted three times, resulting in three distinct measurable periods.

47
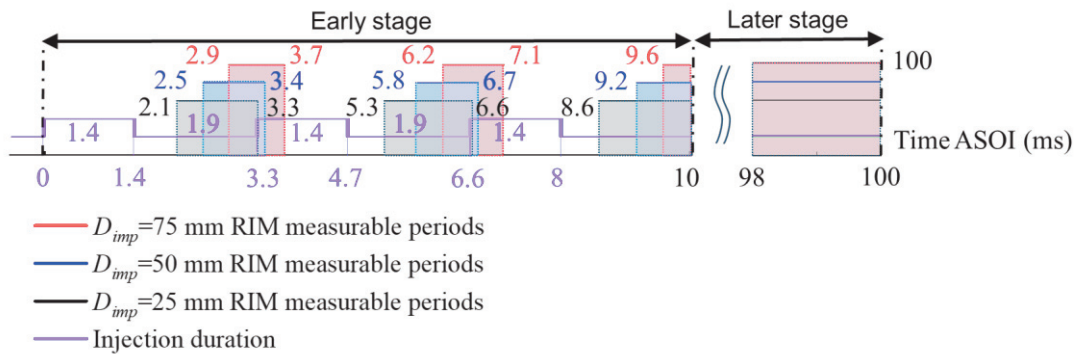
Figure 2.15 Measurable periods for fuel adhesion observation.

2.5 Summary

This chapter first introduces the high-pressure wind tunnel and the experimental platform, then explains the experimental control system, and subsequently presents the fuel supply system. Finally, it provides a detailed description of the optical system required for this experiment. The optical system mainly includes PIV, continuous wave laser-Mie scattering technique, and the RIM. The PIV technique is used to evaluate the uniformity of the cross-flow field; continuous wave laser-Mie scattering technique is used to observe the spray structure; and the RIM method is employed to examine the fuel adhesion characteristics.

CHAPTER 3 FUEL ADHESION CHARACTERISTICS OF SPLIT INJECTION IN CROSS-FLOW UNDER BASELINE CONDITIONS

3.1 Introduction

This study compared the wall-impingement distance of 75 mm as the baseline, the wall-impingement spray behavior, and fuel adhesion characteristics under different cross-flow velocities and injection strategies at wall-impingement distances of 25 and 50 mm were compared. This chapter employs the Continuous wave laser-Mie scattering technique to ensure high-resolution observations of the dynamic behavior of sprays. These techniques provide detailed images of spray morphology and aid in quantifying the diffusion and penetration characteristics of sprays. The RIM method is used to study the fuel adhesion characteristics of wall-impinging sprays. The behavior of the spray in a cross-flow, before and after wall impingement, and its effect on fuel adhesion are described in detail. Quantitative analysis of images captured by high-speed cameras reveals the changes in vertical and horizontal penetration and fuel adhesion characteristics over time. These findings are of significant reference value for applications such as combustion processes and pollution control.

3.2 Experimental Conditions

The experimental setup utilized a wind tunnel to provide a uniform cross-flow field to study the behavior of split injection of wall-impingement spray and fuel adhesion under cross-flow conditions. Continuous wave laser-Mie scattering technology was employed to observe the spray structure in the vertical plane. The RIM method is used to study the fuel adhesion characteristics. Toluene was used as a substitute fuel. The injection pressure is 10 MPa. The experiment employed a single-hole injector with a nozzle diameter of 0.15 mm. Table 3.1 provides a detailed description of the experimental conditions.

Table 3.1 Experimental conditions.

Ambient condition	
Ambient pressure, P_a [MPa]	0.1
Ambient temperature, T_{tem} [℃]	25
Cross-flow velocity, U_x [m/s]	10
Injection condition	
Injector type	Single hole
Hole diameter, D [mm]	0.15
Test fuel	Toluene
Injection pressure, P_{inj} [MPa]	10
Injection splitting strategies T_{inj}	Triple stage injection
Injection mass for $1^{st}, 2^{nd}$, and 3rd stage, m [mg]	2, 2, 2
Impingement condition	
Impingement distance, D_{imp} [mm]	75
Surface roughness, R_f [μm]	Ra 7.7
Shape of impingement wall [mm^2]	Rectangle 125× 70
Impingement wall	Frosted quartz glass

The effects of triple injection (T_{inj}) strategy, on the wall-impingement spray were

studied. The total injection mass remained at 6 mg. The control pulses and injection duration are shown in Figure 3.1.
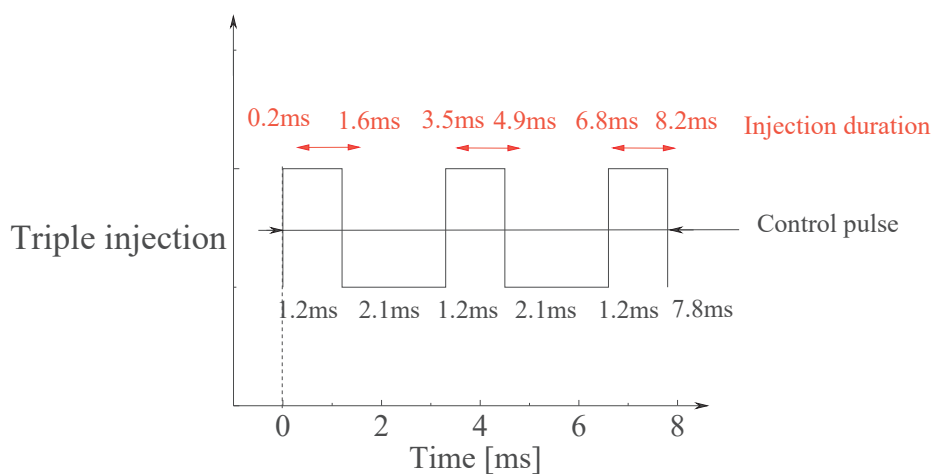
Figure 3.1 Control pulses and injection duration for triple injection strategy.

3.3 Image processing

For each set of experimental conditions, measurements were taken three times, and the average value was calculated. Figure 3.2 illustrates the processing of Mie scattering images. The nozzle tip is positioned at the coordinate (0,0). During the processing of the Mie scattering images, the background image is subtracted from the original image to create a binary image, using a threshold set at 5%. Next, edge detection is performed on the binary image to delineate the macroscopic outline of the impinging spray. The penetration is categorized into vertical and horizontal penetration. Vertical penetration is defined as the maximum distance the spray extends from the nozzle tip in the vertical direction. Horizontal penetration is defined as the maximum distance from the nozzle tip to the theoretical turning point in the horizontal direction.

51
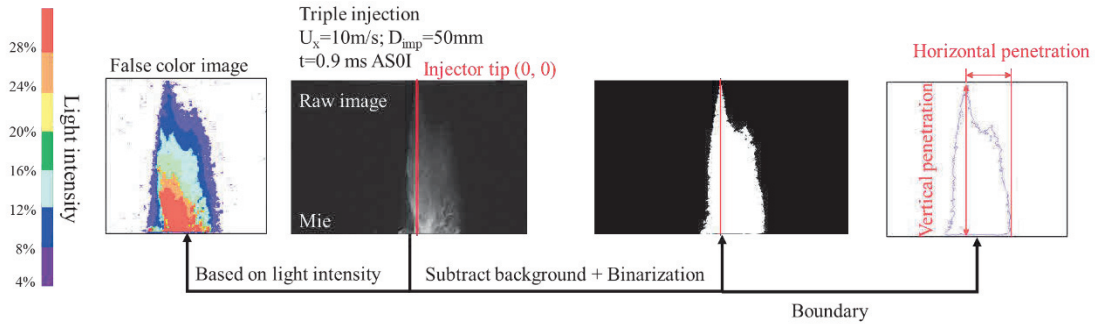
Figure 3.2 Image processing for impingement spray.

The image processing for fuel adhesion is divided into two steps. First, the scattering light difference ΔI (x, y) (Equation 1) is calculated based on the presence of fuel adhesion on the wall. Then, ΔI (x, y) is substituted into the calibration curve to obtain the fuel adhesion thickness h (x, y). The origin (0, 0) is marked with a red cross in the image and is defined as the intersection point within the flat-wall directly below the injector in Figure 3.3.
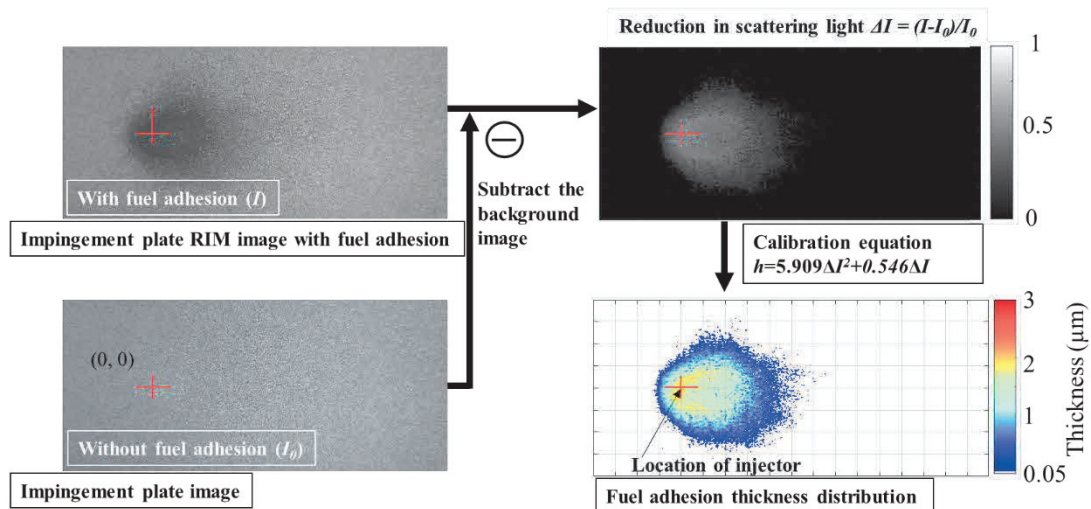
Figure 3.3 Image processing for fuel adhesion

3.4 Results and discussion

3.4.1 Wall-impingement spray in vertical plane

Figure 3.4 describes the formation process of the spray hitting the wall during triple injections under cross-flow conditions (U_x = 10 m/s), with a wall-impingement

distance of 75 mm. The 0.3, 1.4, 4.7, 8.0, and 10 ms ASOI time points represent the stages before the spray hits the wall, during of first injection, the second injection, the third injection, and after the third injection. Under the effect of cross-flow, the spray diffuses and moves downstream. In the second and third segments, the spray will not collide with the previous spray.

Figure 3.4 Side view of wall-impingement spray

Figure 3.5 shows the change in the spray vertical penetration over time, and the red line is the impingement distance. The red hollow line represents the triple strategy in the cross-flow field. The spray vertical penetration increases linearly over time until spray reaches the impingement distance of 75mm. Figure 3.6 shows the change in spray horizontal penetration over time. The spray horizontal penetration increases linearly first, and then gradually stabilizes.
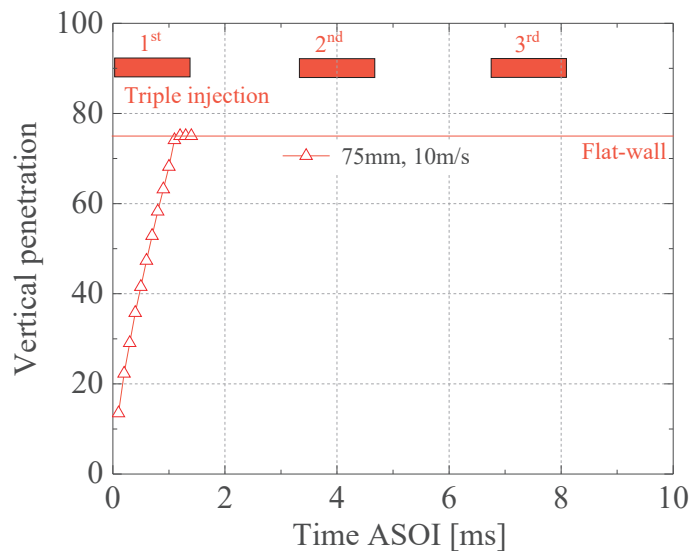
Figure 3.5 Spray vertical penetrations.
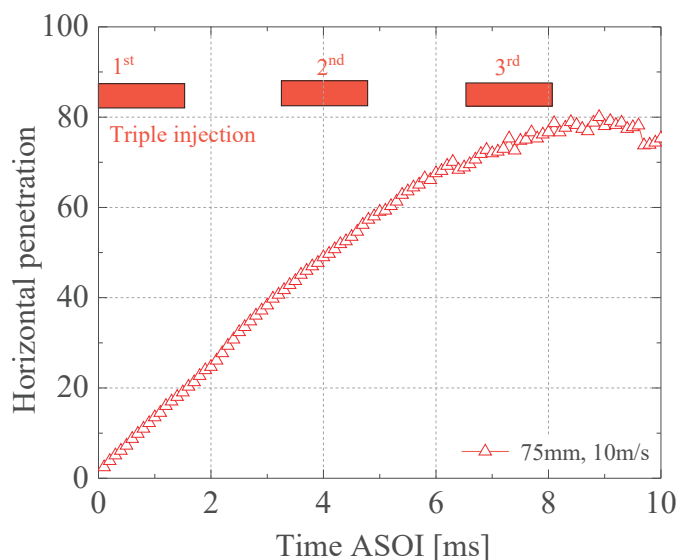
Figure 3.6 Spray horizontal penetrations.

3.4.2 Formation and propagation of fuel adhesion

Figure 3.7 illustrates side view of wall-impingement spray and fuel adhesion at early stage. The color bar in the false-color image uses different threshold ranges (4%, 8%, 12%, 16%, 20%, 24%, 28%) to distinguish the intensity of scattered light in the vertical plane above the spray. The color bar, derived from RIM methods, represents variations in fuel adhesion thickness within the range of 0.05 to 3.0 μm.
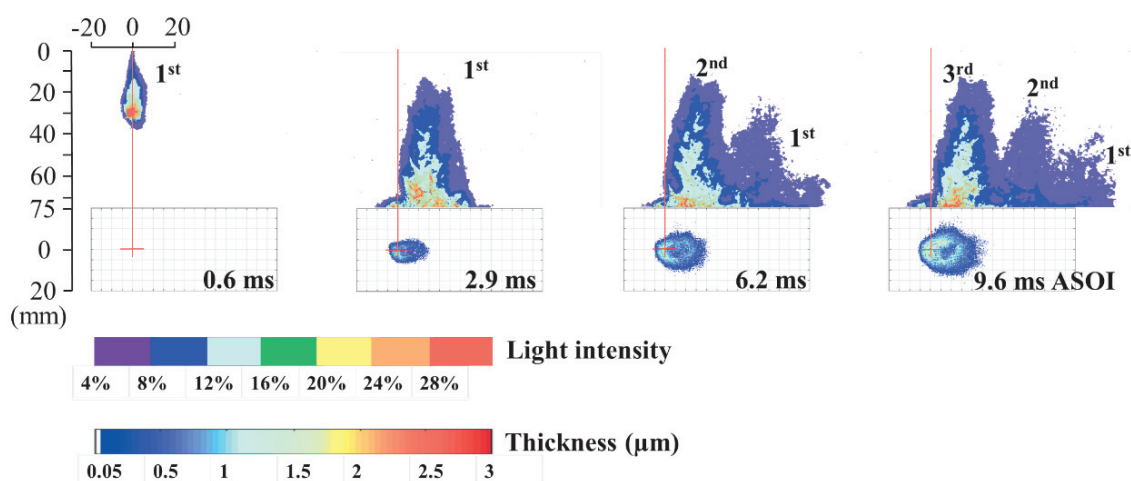
Figure 3.7 Side view of wall-impingement spray and fuel adhesion at early stage.

As can be seen from the figure, the fuel adhesion length on the impingement wall is

always shorter than the length of the vertical spray. This is because not all spray droplets will be completely adhered to the impingement wall. Spray droplets evaporate and rebound after impacting the wall, resulting in only a portion of the spray droplets finally adhering to the wall.

Figure 3.8 illustrates development of fuel adhesion at later stage. Under cross-flow conditions, the fuel adhesion characteristics of the triple injection strategy at 10 ms, 20 ms, and 100 ms ASOI are shown in Figure 3.8. The fuel adhesion near the coordinate origin is thicker, whereas the fuel adhesion at the edge is thinner. The fuel adhesion area first increases and then decreases.
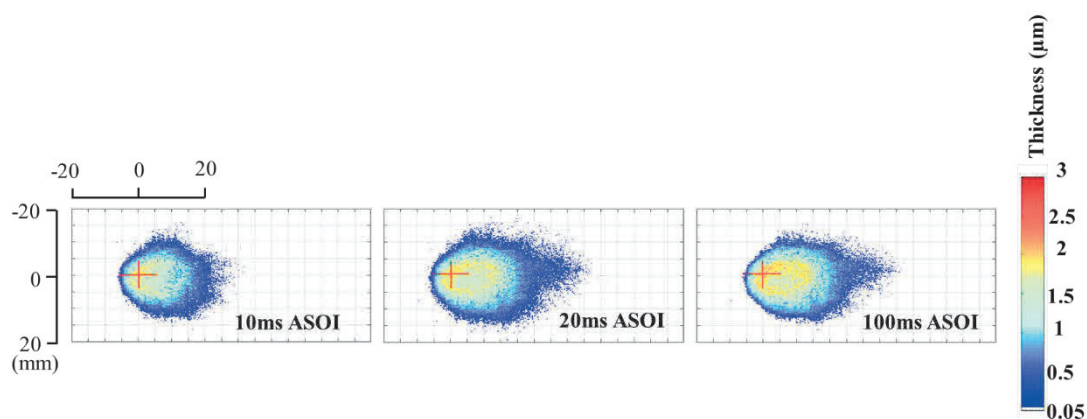
Figure 3.8 Development of fuel adhesion at later stage.

3.4.3 Fuel adhesion area, thickness, and mass

Figure 3.9 depicts the change of the fuel adhesion area over time under cross-flow conditions. The red hollow symbol has a wall-impingement distance of 75 mm and a triple injection strategy under cross-flow conditions. The fuel adhesion area increases first and then decreases. This is because the spray droplets in the air gradually adhere to the wall surface in the early stage, and then the cross-flow promotes the evaporation of the fuel adhesion edge.
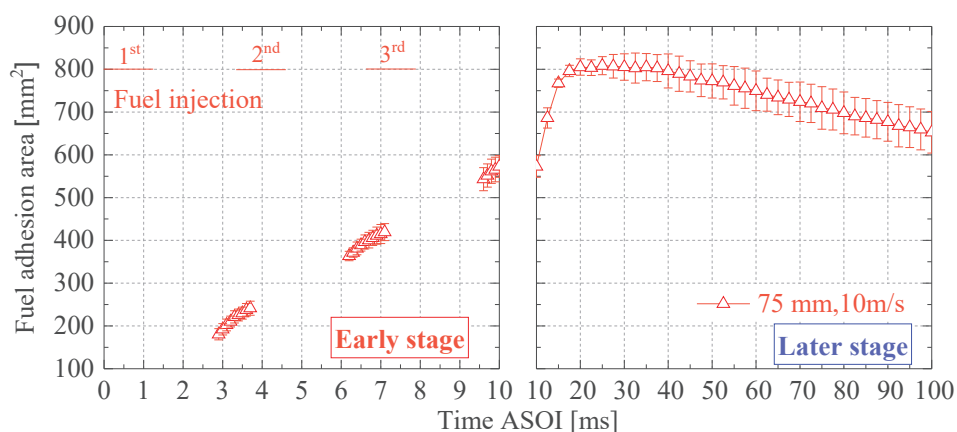
Figure 3.9 Development of fuel adhesion area at later stage.

Figure 3.10 shows the change in average fuel adhesion thickness over time under cross-flow conditions. In the early stage, the average fuel adhesion thickness of each segment injection increases first and then decreases, because the spray droplets in the air initially concentrate on the wall surface, resulting in an increase in the average fuel adhesion thickness. Subsequently, the spray droplets in the air gradually adhere to the edge of fuel adhesion, increasing the fuel adhesion area, so the average fuel adhesion thickness decreases. In the later stage, the average fuel adhesion thickness gradually increases, because there are no spray droplets in the air at this time, and the cross-flow promotes the evaporation of the thinner fuel adhesion at the edge, and the fuel adhesion area decreases, which in turn leads to an increase in the average fuel adhesion thickness.
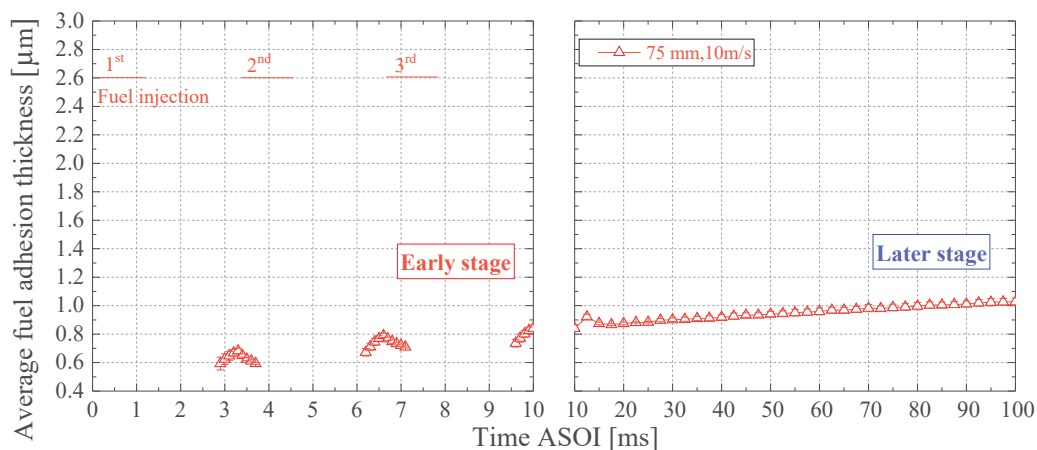
Figure 3.10 Development of average fuel adhesion thickness at later stage.

Figure 3.11 shows the change of fuel adhesion mass and mass ratio over time under cross-flow conditions. The horizontal axis, the left vertical axis, and the right vertical axis represent the time ASOI, fuel adhesion mass, and fuel adhesion mass ratio (the ratio of the fuel adhesion mass to injection mass), respectively. The fuel adhesion mass increases first and then decrease. This is because the spray droplets in the air gradually adhere to the wall surface at first, and then the spray droplets disappear. The cross-flow promotes the evaporation of the fuel adhesion, so the fuel adhesion mass decreases.
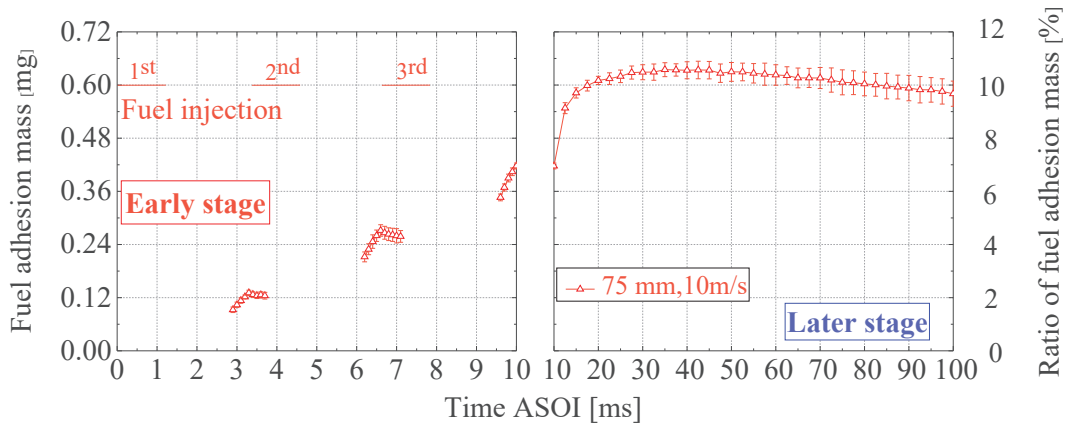
Figure 3.11 Development of fuel adhesion mass at later stage.

3.4.4 Fuel adhesion distribution

Figure 3.12 shows the relationship between the Probability Density Function (PDF) and the fuel adhesion thickness at 10 ms and 100 ms ASOI. The horizontal axis represents the PDF, and the vertical axis represents the fuel adhesion thickness.

There are two peaks. The peak in the thinner area of T=10ms ASOI is larger than that in T=100ms ASOI; The peak in the thicker area of T=10ms ASOI is smaller than that in T=100ms ASOI because cross-flow promotes evaporation in the edge of the fuel adhesion area.
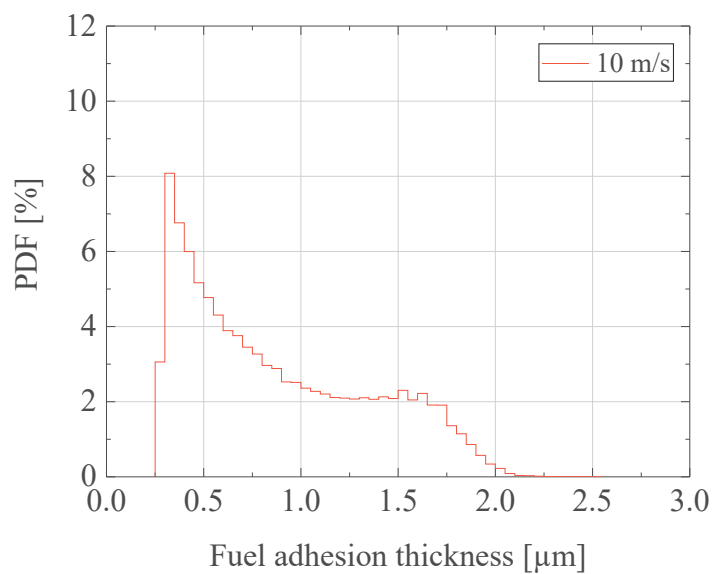
(a) T = 10 ms ASOI.
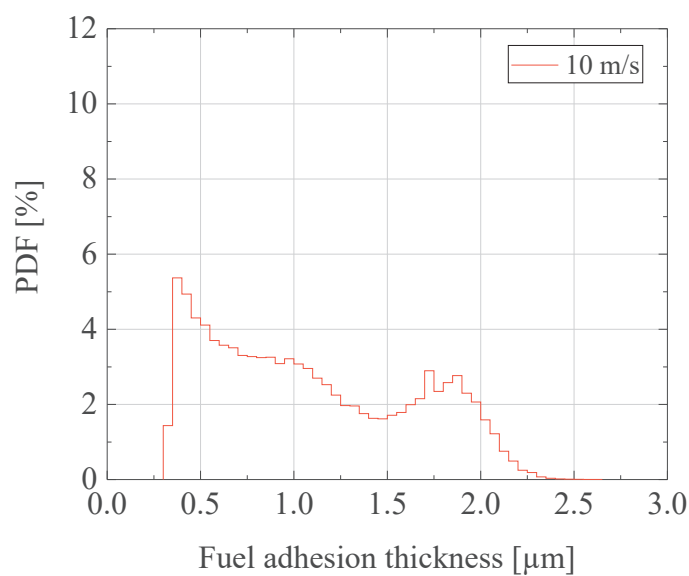
(b) T = 100 ms ASOI.

Figure 3.12 Connection between the PDF and thickness fuel adhesion.

3.4.5 Mechanism of fuel adhesion formation

Figure 3.12 illustrates the mechanism of fuel adhesion development. The blue line boundary represents the spray profile after the injection is completed, and the red

dotted line represents the axis of the injector. The blue broad line at the bottom represents the impact wall, and the upper of the impingement wall represents fuel adhesion. Figure 3.12 shows triple injection under cross-flow conditions (U_x=10m/s). The fuel adhesion length is much smaller than the spray length. Because the droplets in the spray will volatility, splash, and rebound. The spray droplets will not all adhere to the wall. Under cross-flow conditions, the droplets evaporate more, and the droplets flow with the cross-flow and will not reattach to the wall.
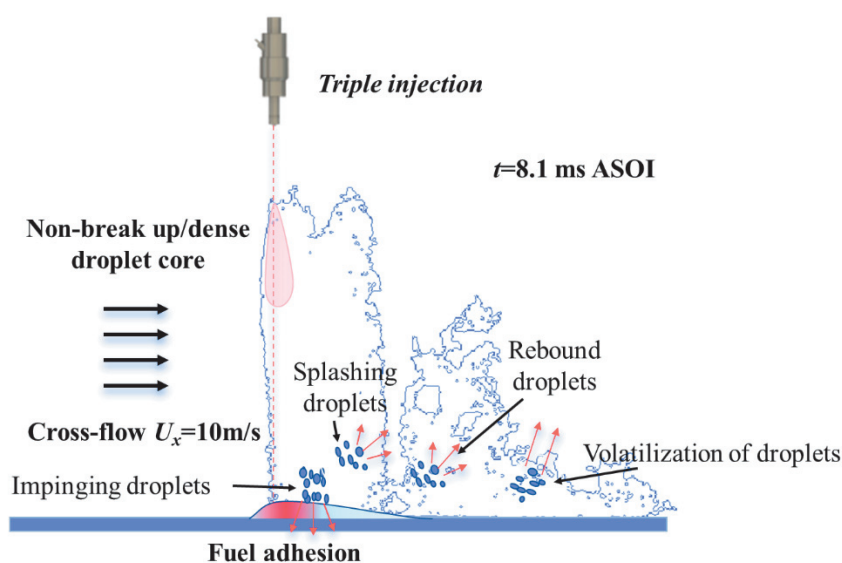
Figure 3.13 Mechanism of fuel adhesion formation.

3.5 Summary

This chapter uses continuous wave laser-Mie scattering technology to observe the dynamic behavior of the spray. The RIM method is used to study the fuel adhesion characteristics of the wall-impingement spray. This study uses the wall-impingement distance of 75 mm as the baseline and describes in detail the behavior of the split spray before and after the wall-impingement in the cross-flow and its effect on the fuel adhesion. The specific findings are as follows.

(1) Under cross-flow, the spray diffuses downstream without colliding with previous segments. The length of fuel adhesion on the impingement wall is consistently shorter than the length of the vertical spray.

(2) Vertical penetration of the spray increases linearly until reaching 75mm impingement distance. Horizontal penetration of the spray initially increases linearly and then stabilizes over time.

(3) Fuel adhesion is thicker near the coordinate origin and thinner at the edges. The fuel adhesion area initially increases, then decreases.

Average fuel adhesion thickness at the early stage injections first increases, then decreases, while in the later stage, it gradually increases. Fuel adhesion mass initially increases and subsequently decreases.

CHAPTER 4 EFFECT OF VARIOUS SPLIT INJECTION STRATEGY ON FUEL ADHESION CHARACTERISTICS

4.1 Introduction

It is crucial to study the spray-wall impingement behavior and fuel adhesion characteristics within DISI engines. Although many researchers focus on the fuel adhesion characteristics of spray-wall impingement to prevent its formation, most studies have been conducted in static flow fields, necessitating further research in airflow fields. Currently, there is still a lack of studies in cross-flow fields, and injection strategies need optimization. While some research involves split injection strategies, the impact of split injection on fuel adhesion characteristics in cross-flow fields has not yet been studied, even though cross-flow fields play an important role during the exhaust phase.

To bridge the existing weak areas, this chapter specifically examined the effect of split injection on wall-impingement spray and fuel adhesion characteristics under static flow and cross-flow field conditions. An optical arrangement was constructed using a high-speed camera and laser sheet light to observe the wall-impingement spray structure in the vertical plane. The fuel adhesion characteristics of the wall spray were examined using the RIM method.

4.2 Experimental Conditions

The experimental setup provides a uniform cross-flow field through a wind tunnel to investigate the wall-impingement spray behavior and fuel adhesion characteristics under cross-flow field conditions. A quartz glass plate of size 125×70 mm^2 was placed horizontally 75 mm below the injector tip inside the observation chamber to observe the wall-impingement spray and fuel adhesion characteristics. The flat-wall was manufactured with a surface roughness of 7.7 μm.

Table 4.1 Experimental conditions.

Ambient condition

Ambient pressure, P_a [MPa]	0.1
Ambient temperature, T_{tem} [℃]	25
Cross-flow velocity, U_x [m/s]	0, 30

Impingement condition

Impingement plate	Quartz glass
Shape of impingement plate [mm^2]	Rectangle 125×70
Impingement distance D_{imp} [mm]	75
Impingement angle [°]	0
Surface roughness, R_f [μm]	Ra 7.7

Injection condition

Injector type	Single hole		
Hole diameter D [mm]	0.15		
Test fuel	Toluene		
Injection pressure, P_{inj} [MPa]	10		
Injection strategies	Single injection [S$_{inj}$]	Double injection [D$_{inj}$]	Triple injection [T$_{inj}$]
Injection mass, m [mg]	6	3:3	2: 2: 2

In this experiment, toluene was employed as a substitute fuel because it is the most common aromatic compound found in gasoline. The diameter of the single-hole injector hole is 0.15 mm. The injection pressure is maintained at 10 MPa. The static flow field was simulated when the cross-flow velocity was set to 0 m/s. A medium engine load condition can be realized with the cross-flow velocity set to 30 m/s. Table 4.1 provides specific illustrations of the experimental conditions.

The continuous wave laser-Mie scattering technique observes the spray structure on the vertical plane. The frame rate, image size, and resolution are 10,000 fps, 1024 × 520, and 5.3 pixels/mm, respectively. The RIM experiment measures the fuel adhesion characteristic. The image size is 960 × 448 pixels with a resolution of 10.7 pixels/mm. The frame rate was set to 10,000 fps. Table 4.2 shows photography conditions.

Table 4.2 Photography conditions.

Photography condition		
Optical methods	Continuous wave laser-Mie scattering technique	RIM
Frame rate[fps]	10,000 fps	10,000 fps
Frame size [pixels]	1024 × 520	960 × 448
Image resolution [pixels/mm]	5.3	10.7

The injection strategies of single injection (S_{inj}), double injection (D_{inj}), and triple injection (T_{inj}) were investigated to better comprehend the wall-impacting spray and fuel adhesion characteristics. To maintain the total injection mass of 6 mg, the injection pulses for the three injection strategies were set to 3.65 ms, 6.0 ms, and 7.8 ms, respectively. The control pulses and injection duration of the three injection strategies are shown in Figure 4.1.
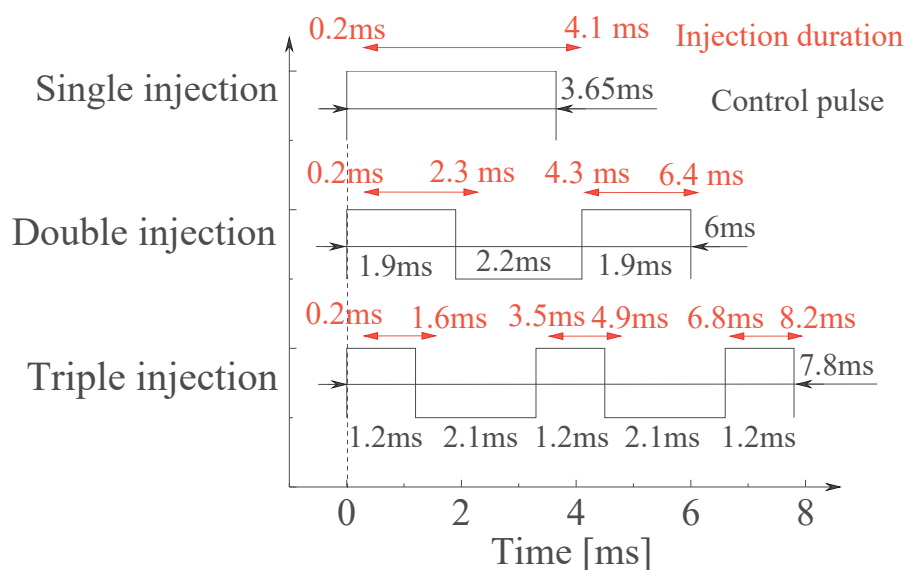
Figure 4.1 Control pulses and injection duration for different injection strategies.

4.3 Image processing

In this chapter, the fuel adhesion characteristics were analyzed in terms of fuel adhesion thickness, area, mass, and deformation. This process was divided into two steps. First, during the image processing of the RIM experiment, the difference ΔI (x, y) of the scattered light is calculated according to whether the wall has fuel adhesion or not by applying Equation (1). Second, to obtain the fuel adhesion thickness h (x, y) ΔI (x, y) is substituted in the calibration Equation (3). Additionally, the mass and area of the fuel adhesion, as well as other fuel adhesion characteristics, can be derived through image processing using the MATLAB code. Under the same experimental condition, the experimental results were obtained by averaging the three sets of experimental data.
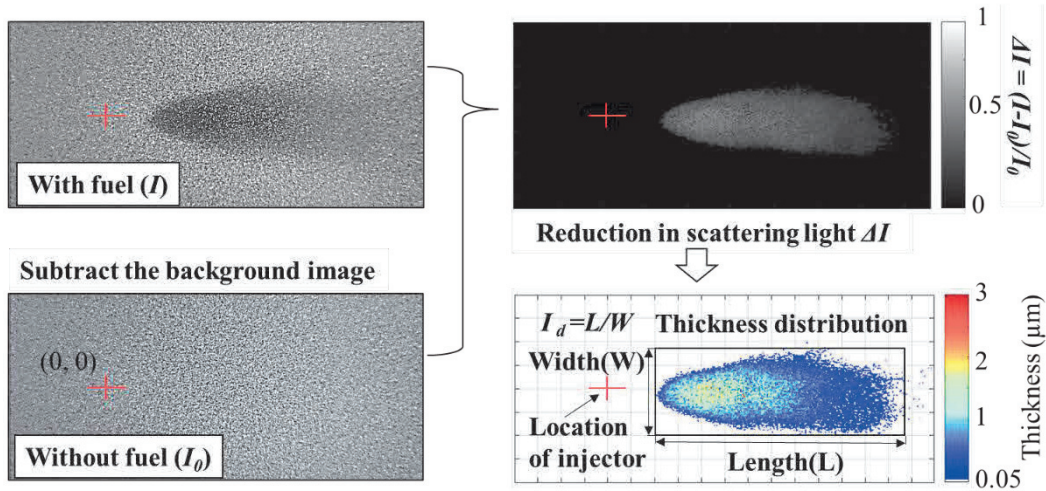
Figure 4.2 Image processing for fuel adhesion analysis.

The coordinate origin (0, 0), which is indicated in the images by the red crossing, is defined as the intersection point directly below the injector within the flat-wall in Figure 4.2. The length L and width W of the fuel adhesion are also defined in Figure 4.2. Furthermore, the deformation coefficient (I_d = length/width) was proposed to evaluate the effect of the cross-flow on the deformation of fuel adhesion.

4.4 Results and discussion

4.4.1 Wall-impingement spray in vertical plane

Figures 4.3 (a), (b), and (c) depict the development process of spray impingement on a wall at a constant impingement distance of 75 mm under static-flow conditions (U_x = 0 m/s) for single, double, and triple injection, respectively. In Figure 4.3 (a), the time points of 0.8, 2.8, 4.0, and 9.0 ms After Start of Injection (ASOI) represent the moments when the first injection spray has not yet contacted the wall, the first injection spray has contacted the wall, the end of the first injection, and the post-evaporation stage of the spray, respectively at single injection. In Figure 4.3(b), the time points of 5.0, 6.0, 6.3, and 9.0 ms ASOI denote the instances during the double injection where the second spray has not yet reached the wall, the ongoing second injection, the end of the second injection, and the post-evaporation stage of the spray,

respectively at double injection. Similarly, Figure 4.3(c) illustrates the triple injection event at 7.4, 8.0, 8.1, and 9.0 ms ASOI, corresponding to the moments before the third spray reaches the wall, during the third injection, at the end of the third injection, and during the post-evaporation stage, respectively at double injection.

From the split injection figures, it is evident that when the second and third sprays have not yet reached the wall, they collide with the residual spray from the previous injection stages. This also provides support for the later analysis of fuel adhesion. During the injection process, the wall jet vortex in the single injection is higher compared to the split injection. At the end of the injection, when the spray has deposited on the wall or evaporated, the single injection results in more spray deposition/evaporation on the wall compared to the split injection. Because the single injection ends earlier.
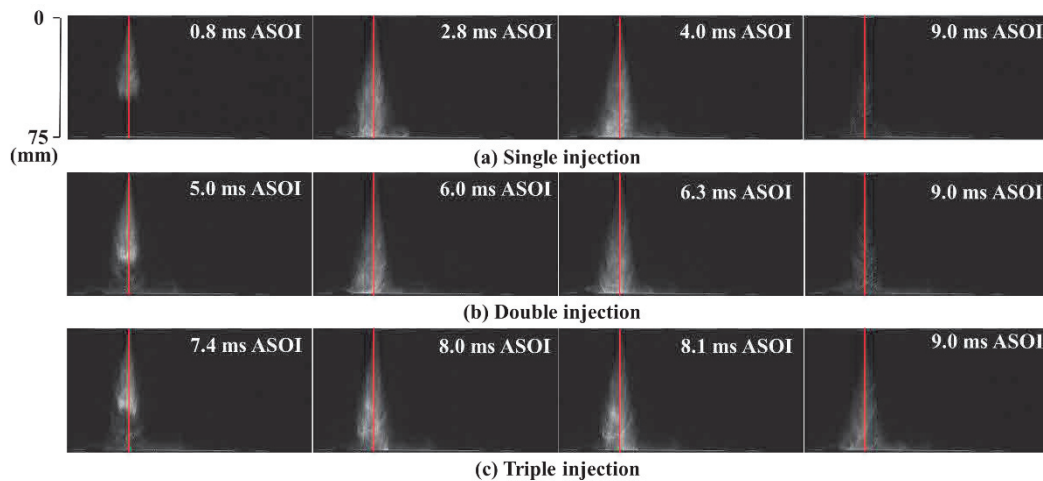
Figure 4.3 Side view of wall-impingement spray of different injection strategies. (Static flow field)

Figures 4.4 (a), (b), and (c) depict the impact of single, double, and triple injections on the development process of wall-impinging spray at a constant impingement distance of 75 mm under cross-flow conditions ($U_x = 30$ m/s). The time points in these figures correspond to the same stages as those in Figure 4.3. From the split injection images, it can be seen that when the second and third sprays have not yet reached the wall, they do not collide with the residual spray from the first and second injections. This is

because the spray moves downstream under the influence of cross-flow. During the injection process, the spray area of the split injection is smaller than that of the single injection because the fuel mass in each stage of the single injection is greater than that in the split injection.
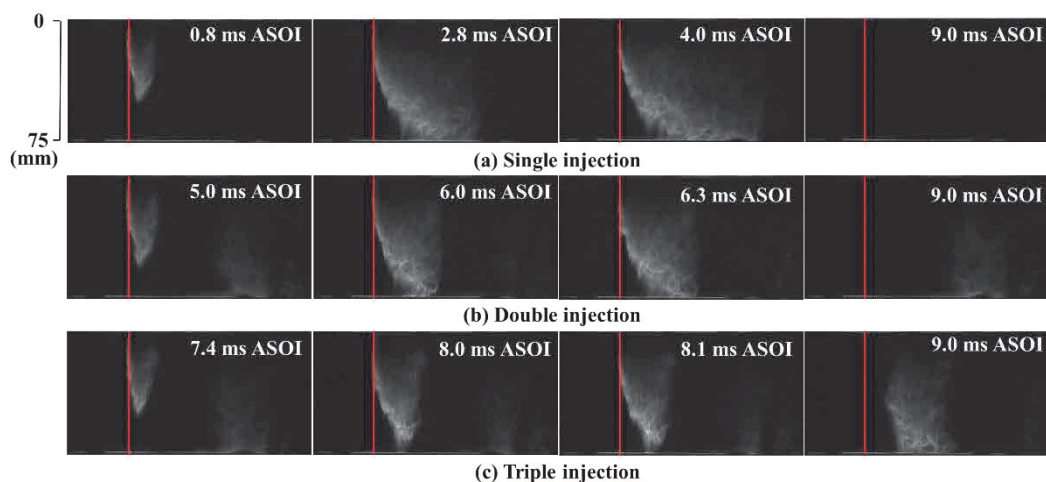
Figure 4.4 Side view of wall-impingement spray of different injection strategies. (Cross-flow flow field)

Figure 4.5 shows the variation of vertical penetration of spray over time, with the black line being the impingement distance. Black, blue, and red represent single, double, and triple injection strategies, respectively. The solid line and hollow line represent the static flow field and the cross-flow field, respectively. Under different injection conditions, the time when the spray hits the wall is basically the same. Under cross-flow conditions, the increased rate of vertical penetration in the triple injection is the lowest.
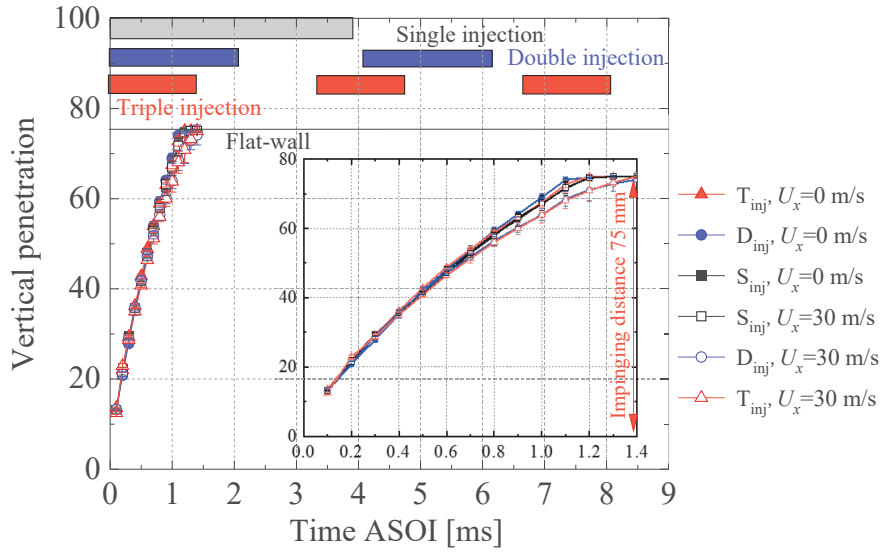
Figure 4.5 Spray vertical penetrations.

Figure 4.6 shows the change of spray horizontal penetration over time.
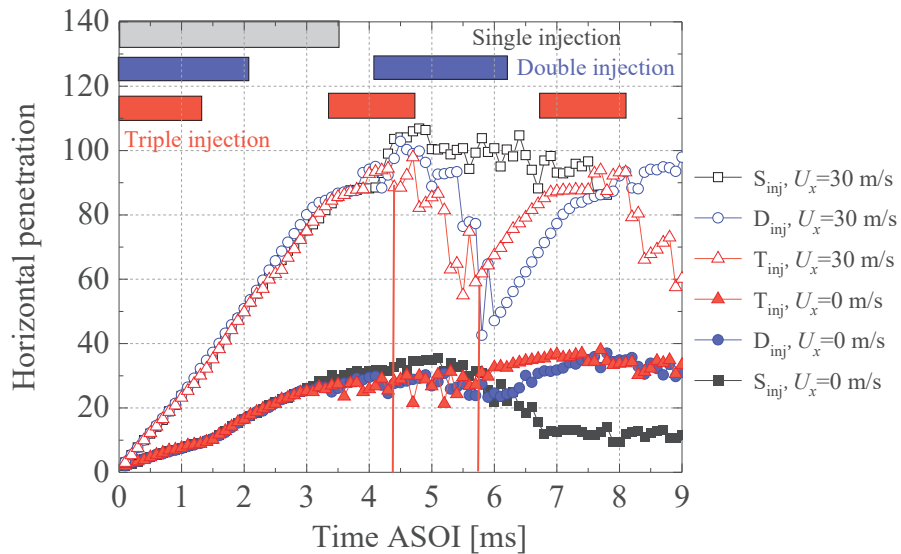
Figure 4.6 Spray horizontal penetrations.

As can be seen from Figure 4.6, in each injection process, the spray horizontal penetration first rises smoothly and then fluctuates over time. This is because the spray continues to diffuse during injection and just after injection, resulting in increased spray horizontal penetration. In the later stage of injection, the spray

evaporates and diffuses, resulting in fluctuations in spray horizontal penetration. Under cross-flow conditions, the fluctuation of split injection spray drops sharply because the previous spray disappears under the action of cross-flow. Details are shown in Figure 4.7. Figure 4.7 shows the spray detail at the highest and lowest values of horizontal penetration for the first injection in the triple injection.
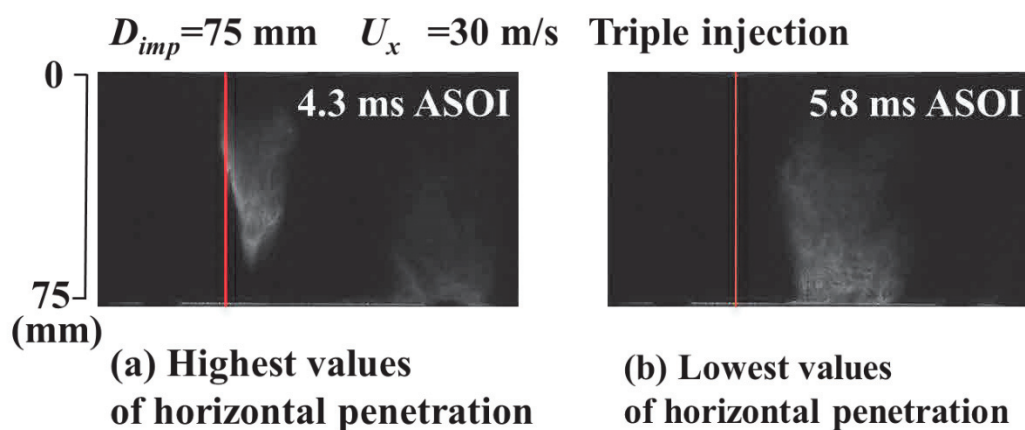
Figure 4.7 Detail of spray.

4.4.2 Formation and propagation of fuel adhesion

Figure 4.8 shows the effect of the development process of the wall-impingement spray and the fuel adhesion of different strategies at the same wall-impingement distance of 75 mm under static flow field conditions ($U_x = 0$ m/s). The color bar of the pseudo-color images uses different threshold ranges (4%, 8%, 12%, 16%, 20%, 24%, and 28%) to distinguish the vertical plane spray of light intensities on the upside. The color bar of the pseudo-color images, which were obtained from the RIM experiment, represents varying fuel adhesion thicknesses from 0.05 to 3.0 μm on the downside.
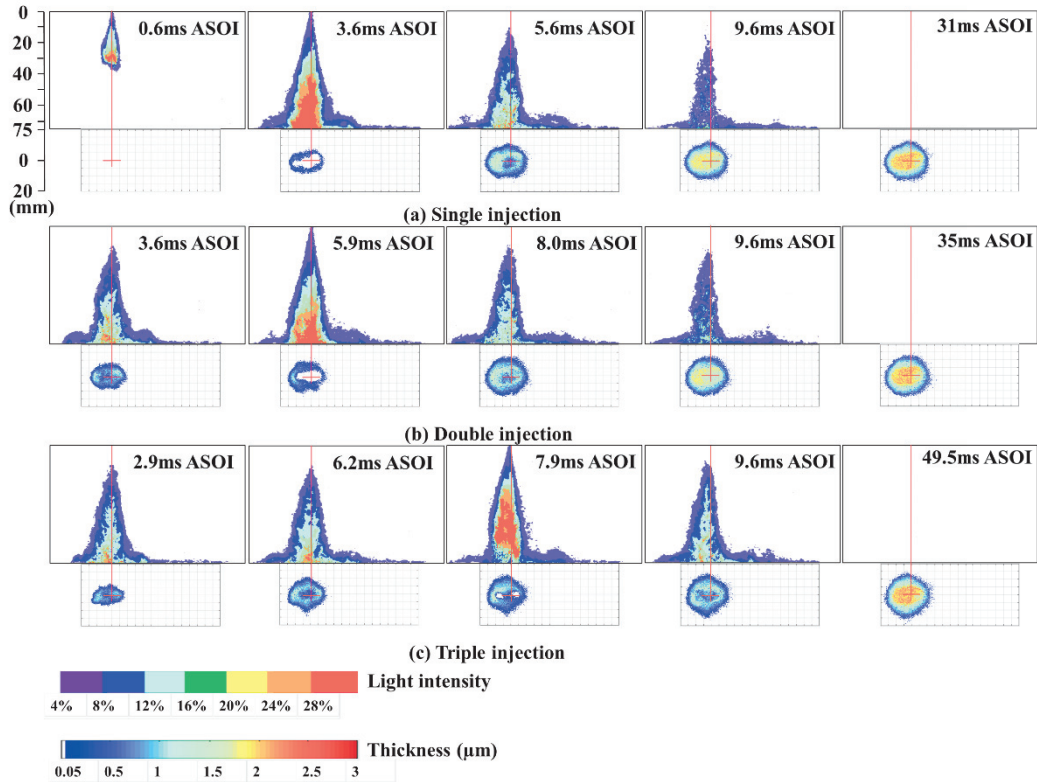
Figure 4.8 Side view of wall-impingement spray and fuel adhesion of different injection strategies at early stage. (Static flow field)

The white region appears under static flow field conditions in Figure 4.8, such as 3.6 ms ASOI of a single injection, 5.9 ms ASOI of double injection, and 7.9 ms ASOI of triple injection. Owe to the limitations of the RIM method, the spray scattering light error ($I_0 < I$) exists during injection, which results in the formation of the white region. In this study, the time before 10 ms ASOI is referred as the early stage. The white region in the early stage was observed to have affected all the fuel adhesion characteristics, except for the fuel adhesion area. In this paper, the end time of spray impingement injection is defined as the time when there is no spray image in the wall-impingement spray side view.

Figure 4.8 (a) shows the spray formation for a single injection at 0.6 ms, 3.6 ms, 5.6 ms, 9.6 ms, and 31 ms ASOI. Notably, fuel adhesion does not exist on the flat-wall because the spray does not reach the flat-wall at 0.6 ms ASOI, the fuel adhesion does not exist on the flat-wall. The spray structure and fuel adhesion at 3.6 ms ASOI are

shown during the single injection. The first available image without the white region is 5.6 ms ASOI. The end time of spray impingement at single injection condition is 31 ms ASOI. The results of the double injection for 3.6 ms, 5.9 ms, 8 ms, 9.6 ms, and 35 ms ASOI are shown in Figure 4.8 (b). The image of 3.6 ms is the first available image before the next injected spray reaches the flat-wall. The spray structure and fuel adhesion at 5.9 ms ASOI are shown during the second injection. The image at 8.0 ms ASOI is the first available image for calculating the second injection. The end time of spray impingement at double injection is 35 ms ASOI. Images acquired at triple injection are shown in Figure 4.8 (c). Similar to double injection, images at 2.9 ms, 6.2 ms, 9.6 ms, and 49.5 ms ASOI are all available images within the triple injection. The spray structure and fuel adhesion at 7.9 ms ASOI are shown during the third injection. The end time of spray impingement at triple injection is 49.5 ms ASOI.

Figure 4.9 shows the effect of the development process of the wall-impingement spray and the fuel adhesion characteristics of different strategies at the same wall-impingement distance of 75 mm under cross-flow field conditions (U_x =30 m/s). Despite the absence of an obvious white region under cross-flow field conditions, a spray scattered light error ($I_0 < I$) still exists during injection. The available fuel adhesion figures for single injection, double injection, and triple injection are 5.6 ms, 8.0 ms, and 9.6 ms ASOI, respectively. The end time of spray impingement at single injection, double injection, and triple injection is 9.0 ms, 11.5 ms, and 13.5 ms ASOI, respectively. A detailed analysis of the timing selection is shown in Figure 4.8. To eliminate the influence of the white area on the adhesion characteristic analysis, the time after 10 ms ASOI was judged to be preferable, which corresponds to the next later stage.
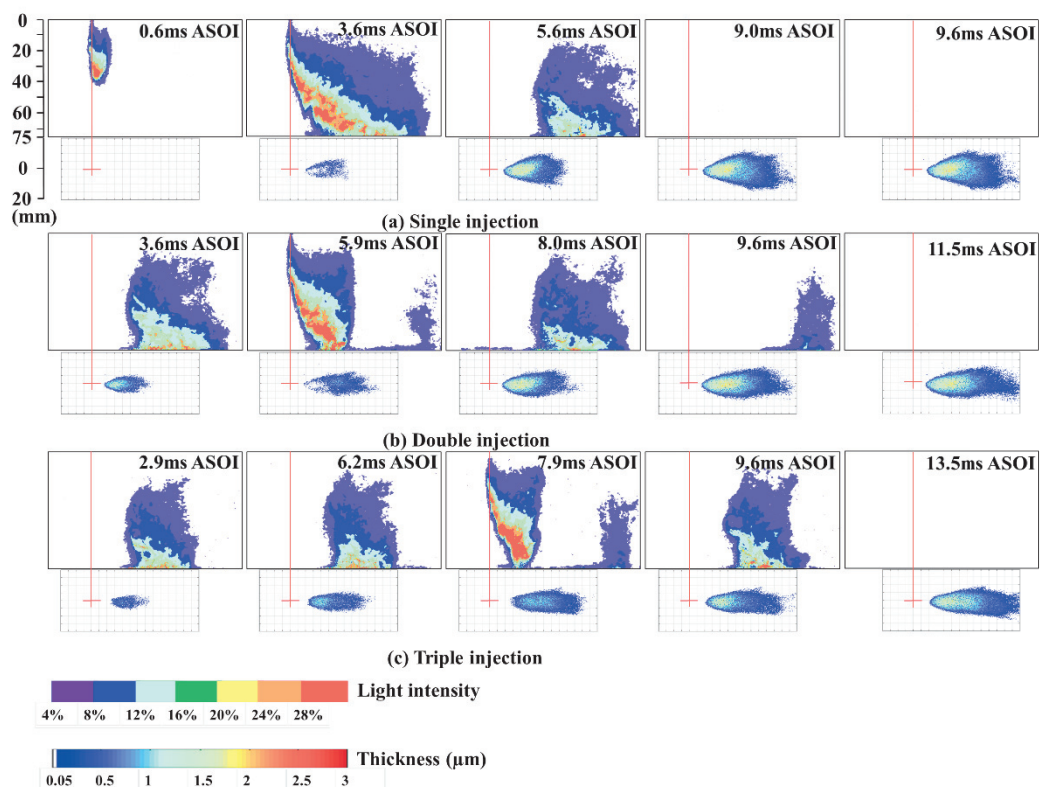
Figure 4.9 Side view of wall-impingement spray and fuel adhesion of different injection strategies at early stage. (Cross-flow field)

From the vertical plane spray structure, the wall-impingement spray was symmetrical under static flow field conditions. Under cross-flow field conditions, numerous tiny droplets can be blown downstream followed by the enhancement of the diffusion of the wall-impingement spray, resulting in an asymmetrical distribution. The wall-impingement spray area is enlarged. From the figure obtained by the RIM method, the fuel adhesion shape is almost a circle under the static flow field conditions, whereas the fuel adhesion shape is a slender strip under cross-flow field conditions. The fuel adhesion length on the flat-wall was shorter than the width of the vertical spray regardless of the injection strategy employed. This is because the post-rebounded droplets accounted for a considerable proportion, resulting in a smaller fuel adhesion area adhered to the flat-wall.
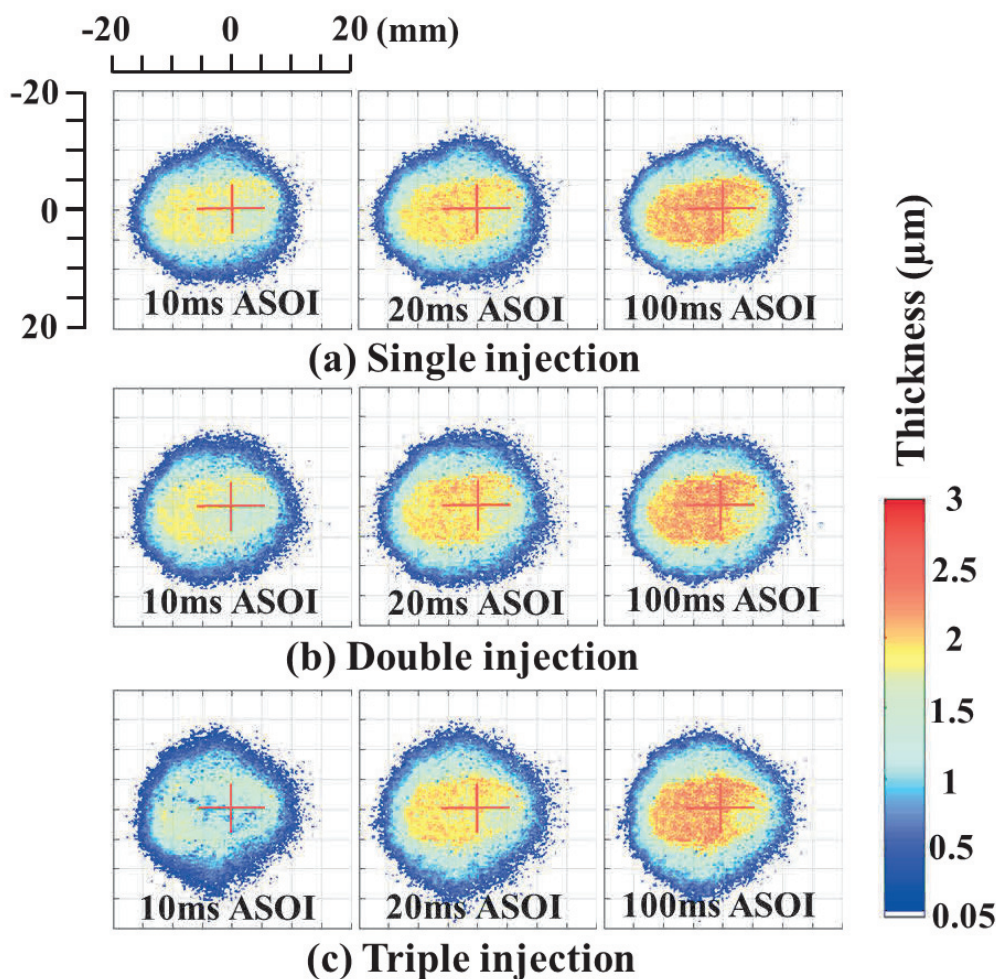
Figure 4.10 Development of fuel adhesion of different injection strategies at later stage. (Static flow field)

Under static flow field conditions, the fuel adhesion characteristics of the different injection strategies at 10 ms, 20 ms, and 100 ms ASOI are shown in Figure 4.10. The color bar of the pseudo-color images represents the varying fuel adhesion thicknesses from 0.05 to 3.0 μm on the right. The results showed that the fuel adhesion thickness increased with time. This is because many droplets adhere to the flat-wall over time. The fuel adhesion near the coordinate origin is thicker, whereas the fuel adhesion at the edge is thinner. Meanwhile, the fuel adhesion thickness of the triple injection was observed to be the thinnest at 10 ms ASOI.
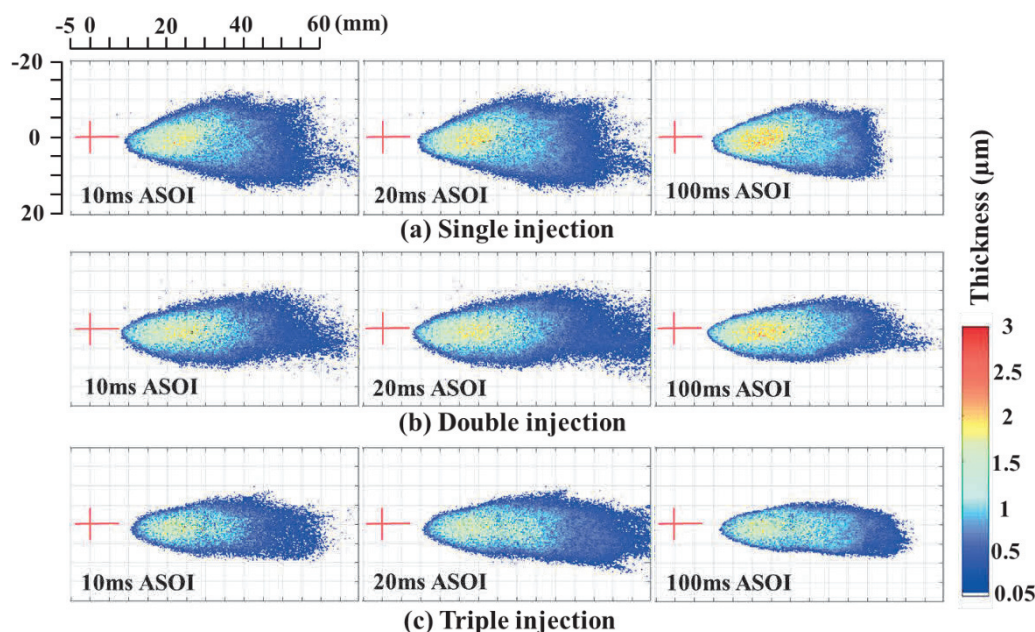
Figure 4.11 Development of fuel adhesion of different injection strategies at later stage. (Cross-flow field)

Under cross-flow field conditions, the fuel adhesion characteristics of the different injection strategies at 10 ms, 20 ms, and 100 ms ASOI are shown in Figure 4.11. The upstream boundary of fuel adhesion is clearly evident, whereas the downstream boundary of fuel adhesion under cross-flow field conditions can be observed to be chaotic. Simultaneously, the fuel adhesion width gradually decreased with the increasing number of injections. Compared with the static flow field, the fuel adhesion thickness in the central region was significantly stable over time, whereas the edge disappeared under cross-flow field conditions. This can be attributed to the fact that many droplets are blown away by the cross-flow, the possibility of adhering to the fall-wall is greatly reduced, and the cross-flow promotes the evaporation of fuel adhesion. In addition, the fuel adhesion thickness under cross-flow field conditions can be observed to be lower. A more quantitative analysis of fuel adhesion characteristics is necessary to comprehend further fuel adhesion phenomena using different injection strategies.

4.4.3 Fuel adhesion area, mass, and thickness

Figure 4.12 depicts the development of the fuel adhesion area over time at a later stage under the static flow and cross-flow field conditions. The horizontal axis represents time ASOI. The vertical axis represents the fuel adhesion area. The solid symbols of different colors show the results of different strategies under static flow field conditions. The hollow symbols of different colors show the results of the different strategies under cross-flow field conditions. Black, blue, and red represent the single, double, and triple injection strategies, respectively.
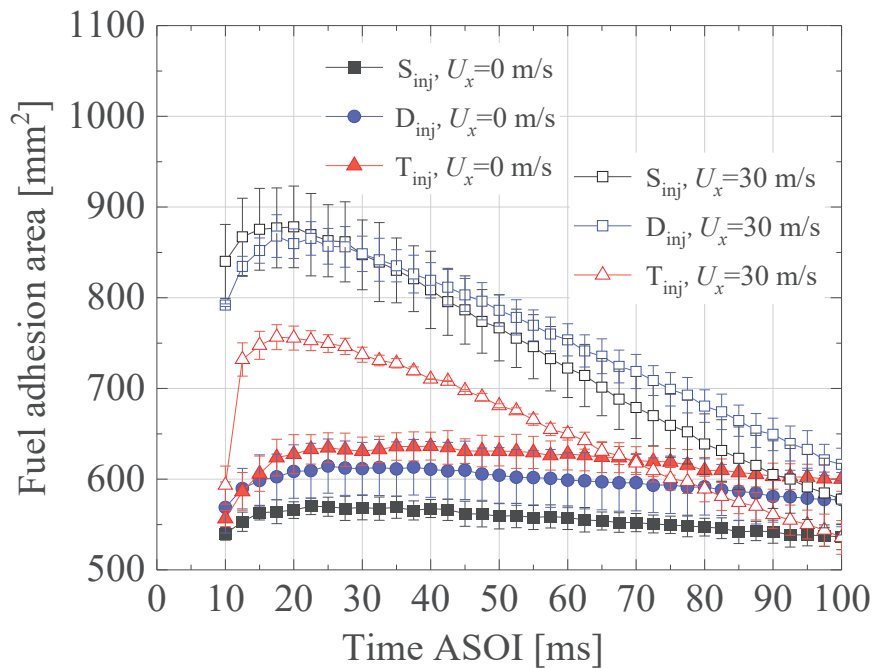
Figure 4.12 Development of fuel adhesion area at later stage.

From this result, the fuel adhesion areas can be observed to rapidly increase during the 10-20 ms ASOI. During this stage, the spray injection has just finished, and the breakup droplets remaining in the ambient will continue to adhere to the flat-wall. At the beginning of the development of fuel adhesion, the fuel adhesion area under cross-flow field conditions was larger than that under static flow field conditions. The cross-flow promoted the diffusion of the spray, resulting in an increase in the fuel adhesion

area adhered to the flat-wall. After 20 ms ASOI, the fuel adhesion area slightly decreased under static flow field conditions, while the fuel adhesion area decreased dramatically with time under cross-flow field conditions. This is because cross-flow enhances the evaporation of fuel adhesion.

Under the static flow field conditions, the fuel adhesion area of the triple injection is the largest, whereas, under cross-flow field conditions, the fuel adhesion area of the triple injection is the smallest. In a static flow field with split injection, the spray from the second injection increases the ductility of fuel adhesion on the wetted flat-wall caused by the first injection. The third injection followed the same procedure. Therefore, the fuel adhesion area of triple injection under a static flow field was the largest. However, the spray can be exposed to the ambient above the flat-wall for a longer time with the split injection strategies under cross-flow field conditions. This indicates that the cross-flow can more effectively promote the evaporation of the spray during split injection and promote the evaporation of split injection fuel adhesion, especially at the edges where the fuel adheres. Therefore, triple injection further improved the reduction in the fuel adhesion area under cross-flow field conditions. Interestingly, the fuel adhesion area of the double injection is the largest under cross-flow conditions. Breakup and atomization of droplets in the air will be improved very much in the cross-flow field conditions by split injections. However, the present results show that only the triple injection highlights the above-mentioned influences of cross-flow. Although the double injection has narrowed the fuel adhesion area obtained by the single injection (especially in the early stage, it can be seen that the data are all within the error-bar range). However, the reduction of fuel adhesion caused by the cross-flow is not enough to offset the increase in the ductility of fuel adhesion on the wet plate caused by the first injection. This indicates that the fuel adhesion area of the double injection mainly follows the principle under the static field. In other words, the spray from the second injection increases the ductility of fuel adhesion on the wetted plate caused by the first injection. Consequently, the double injection area is the largest.

Figure 4.13 depicts the development of the fuel adhesion mass over time at a later stage under the static flow and cross-flow field conditions. The horizontal axis, the left vertical axis, and the right vertical axis represent the time ASOI, fuel adhesion mass, and fuel adhesion mass ratio (the ratio of the fuel adhesion mass to injection mass), respectively. The solid and hollow symbols of different colors show the fuel adhesion mass and fuel adhesion mass ratio of different strategies under static flow field and cross-flow field conditions, respectively. The results show that the fuel adhesion mass remains stable under static flow field conditions, while the fuel adhesion mass gradually decreases with time under cross-flow field conditions, which is also attributed to the fact that the cross-flow promotes the evaporation of fuel adhesion.
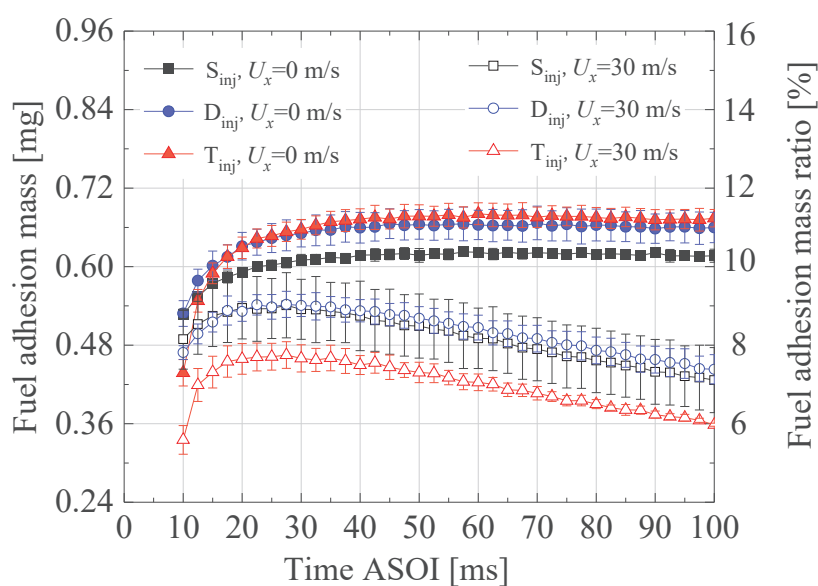
Figure 4.13 Development of fuel adhesion mass at later stage.

In the static flow field, the fuel adhesion mass of the triple injection was the largest, whereas that of the triple injection was the smallest in the cross-flow field. The relative velocity between the surrounding air and droplets generates aerodynamic forces, leading to a reduction in droplet velocity [130]. In a static flow field with split injection, the kinetic energy of the droplets of the first injection in the ambient environment was reduced because of the aerodynamic forces before the second

injection. During the second injection, the breakup droplets of the second injection collided with those of the first injection, resulting in an increase in the kinetic energy of the first injection droplets in the vertical direction. Subsequently, the first injection droplets are pushed to the outer spray region, accelerating their adhesion on the flat-wall. The third injection is the same as the above injection pattern, which resulted in the triple injection exhibiting the largest fuel adhesion mass under a static flow field. Conversely, the single injection demonstrated the smallest fuel adhesion mass.

The same phenomenon occurred when the second injection spray collided with the droplets from the first injection in the cross-flow field. Owing to the exchange of momentum between the droplet and cross-flow, the velocity of the spray droplets increased horizontally [98]. The cross-flow enables split injection spray droplets to obtain both the vertical and more horizontal kinetic energies. Meanwhile, each segment injection mass of the triple injection is sufficiently small, so the fuel spray is more likely to be blown downstream by the cross-flow. Additionally, the fuel spray of the split injection is more likely to be atomized and evaporated under cross-flow field conditions. The above reasons prevent the fuel from adhering to the flat-wall in the cross-flow field, resulting in a lower fuel adhesion mass of the triple injection under cross-flow field conditions.

Figure 4.14 and Figure 4.15 depicts the development of the fuel adhesion thickness over time at a later stage under the static flow and cross-flow field conditions. The horizontal axis represents time ASOI. The vertical axis represents the average fuel adhesion thickness, as shown in Figure 4.14. The vertical axis represents the maximum fuel adhesion thickness in Figure 4.15.
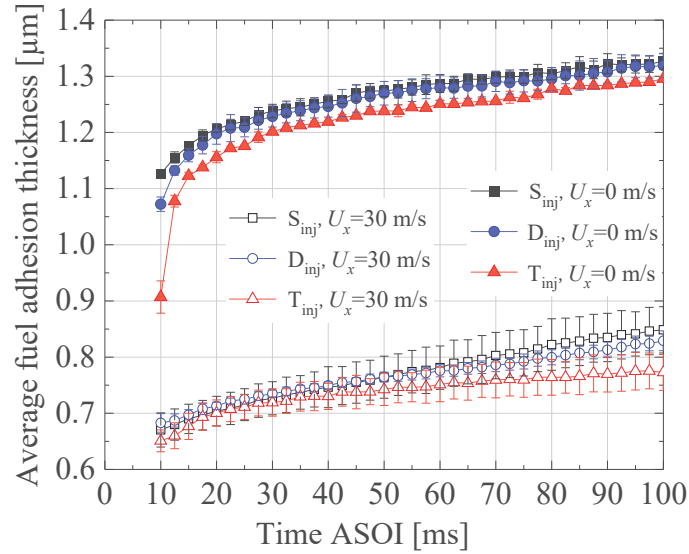
Figure 4.14 Development of average fuel adhesion thickness at later stage.

As shown in Figure 4.15, the maximum fuel adhesion thickness gradually increased with the ASOI time. The maximum fuel adhesion thickness under cross-flow field conditions was slightly smaller than that in the static flow field, but the maximum fuel adhesion thickness under the two statuses was the same at approximately 100 ms ASOI.
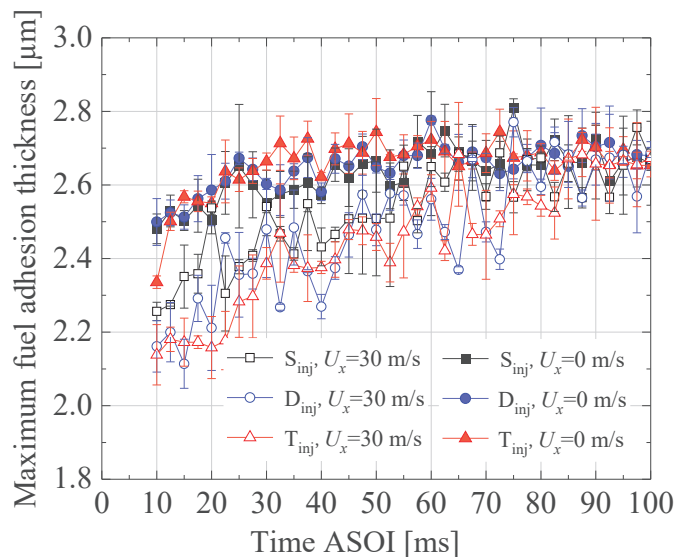
Figure 4.15 Development of maximum fuel adhesion thickness at later stage.

As shown in Figure 4.14, the average fuel adhesion thickness under cross-flow field conditions is much smaller than that under the static flow field conditions. The main reason is because the fuel adhesion area is increased under cross-flow conditions in which the diffusion of fuel adhesion is promoted. The average fuel adhesion thickness increased over time, but the rate of increase gradually decreased. The first reason is that residual break up droplets in the ambient environment will continue to adhere to the flat-wall. The second reason is that the fuel adhesion area decreases with the evaporation of fuel adhesion. The increased rate of average fuel adhesion thickness under cross-flow field conditions was larger than that under static flow field conditions. The main reason for this is that the fuel adhesion area decreases rapidly, and the thinner fuel adhesion in the edge region evaporates quickly under cross-flow field conditions, as shown in Figure 4.11.

Additionally, the results show that the average fuel adhesion thickness of the triple injection is the smallest under static flow and cross-flow field conditions. Under static flow field conditions, more wall-jet vortex can be generated with split injection strategies, and more spray droplets are rolled up, resulting in thinner fuel adhesion. As mentioned in the description of Figure 4.13, because each segment injection mass of triple injection is sufficiently small, the fuel spray is more likely to be blown downstream by the cross-flow, thus avoiding adherence to the flat-wall under cross-flow field conditions. Meanwhile, the fuel spray is more likely to be atomized and evaporated because of the longer exposure time under cross-flow field conditions. These reasons result in the smallest fuel adhesion thickness of triple injection under cross-flow field conditions.

4.4.4 Fuel adhesion deformation

Figure 4.16 length the deformation of the fuel adhesion over time at a later stage under static flow and cross-flow field conditions. The horizontal axis represents time ASOI. The vertical axis represents the fuel adhesion length, as shown in Figure 4.16. The vertical axis in Figure 4.17 represents the fuel adhesion width. The vertical axis

represents the deformation coefficient I_d in Figure 4.18. To quantitatively evaluate the effects of split injection on the fuel adhesion morphology, an indicator "deformation coefficient I_d " is proposed to describe the fuel adhesion deformation (I_d =length/width), which is already defined in Figure 4.2. When I_d approaches 1, the fuel adhesion shape approaches a circle.
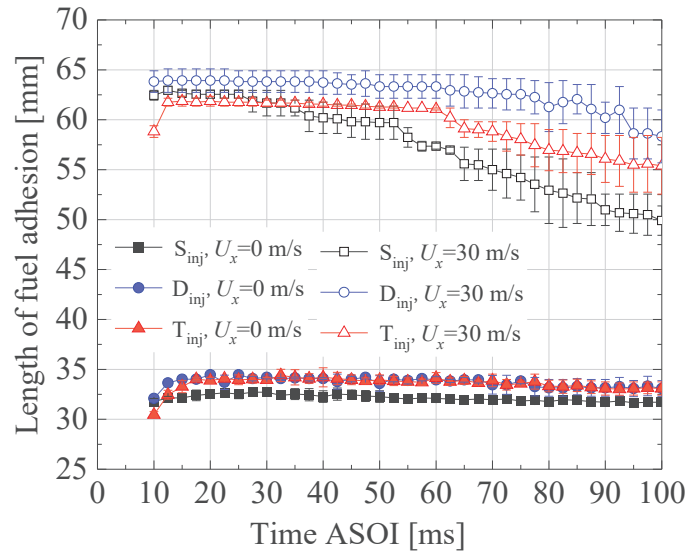
Figure 4.16 Length of fuel adhesion at the later stage.
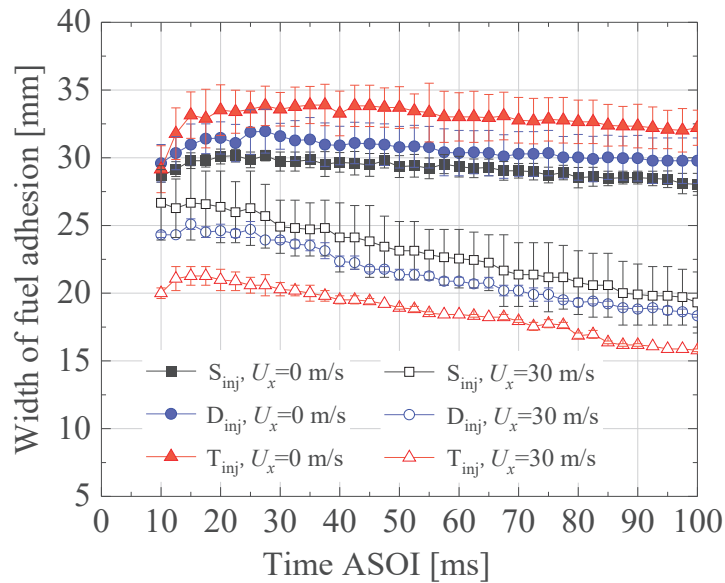
Figure 4.17 Width of fuel adhesion at the later stage.

Under cross-flow field conditions, the fuel adhesion length was longer than that in the static flow field; however, the opposite was true for the fuel adhesion width. Therefore, the deformation coefficient I_d under cross-flow field conditions is larger than that in the static flow field, and a value larger than 1 indicates that the fuel adhesion can easily exhibit a slender strip shape. The cross-flow promotes the shape of fuel adhesion and becomes elongated, as shown in Figure 4.11. Both the length and width of the fuel adhesion decreased with time in the cross-flow field, whereas the length and width of the fuel adhesion remained stable in the static flow field. It can be proved again that the cross-flow promotes the rapid evaporation of thinner fuel adhesion in the fuel adhesion edge region.
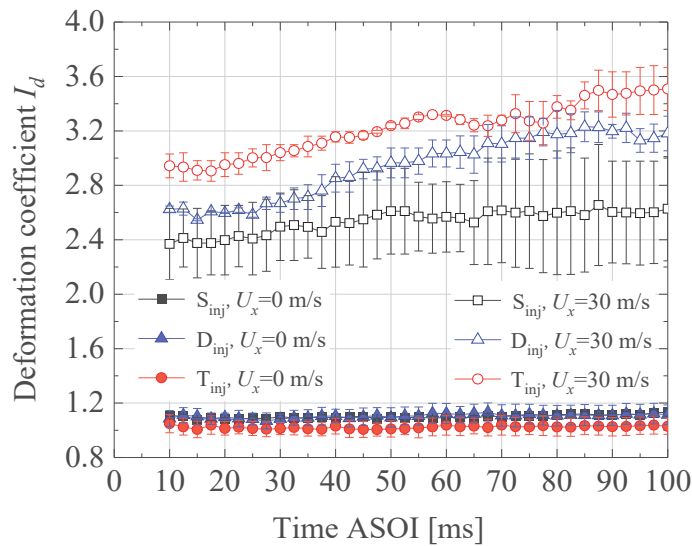
Figure 4.18 Deformation coefficient of fuel adhesion at the later stage.

As shown in Figure 4.18, split injection can lead to an increase in the deformation coefficient under cross-flow field conditions, implying that the fuel adhesion becomes elongated. Comparing the three injection strategies, the I_d of double and triple injections increased almost linearly. However, I_d is stable after 50 ms ASOI at the single injection; furthermore, notably the variation in I_d is considerably large currently. In addition, I_d is almost equal to 1 under static flow conditions, implying that the fuel adhesion shape is close to a circle.

4.4.5 Fuel adhesion distribution

Figure 4.19 shows the relationship between the thickness and mass of the fuel adhesion for different injection strategies at 10 ms and 100 ms ASOI under static flow and cross-flow field conditions. The horizontal axis represents the fuel adhesion thickness, and the vertical axis represents the fuel adhesion mass.
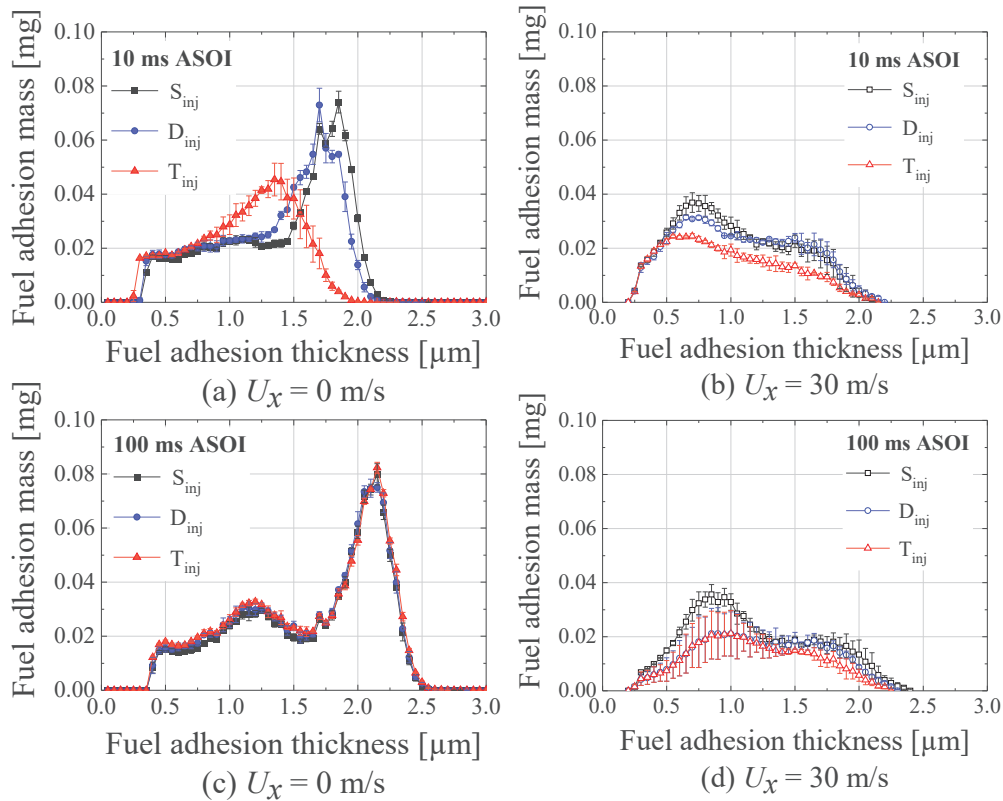
Figure 4.19 Relationship between the thickness and mass of fuel adhesion at later stage.

It can be observed that the fuel adhesion mass presents two peaks along the fuel adhesion thickness direction: a higher peak appears in the thinner fuel adhesion thickness, and a lower peak appears in the thicker fuel adhesion thickness. Interestingly, the fuel adhesion concentrated on thicker peaks under the static flow field conditions and on thinner peaks under cross-flow field conditions. This is because the cross-flow can promote the dispersion and evaporation of fuel adhesion,

and a thinner fuel adhesion can be observed under cross-flow field conditions. With the split strategies effect, the fuel adhesion mass becomes more uniform with the increase of injection split times under cross-flow field conditions. Moreover, the peak value of the split injection decreased while the peak value of a single injection remained almost unchanged over time. Additionally, under a static flow field, the peak value of the split injection shifted to thicker peaks with time.

4.4.6 Mechanism of fuel adhesion formation

Figure 4.20 illustrates different mechanisms of fuel adhesion development. The purple line boundary represents the spray profile after the injection is completed, and the red dotted line represents the axis of the injector. The blue broad line at the bottom represents the impingement wall, and the upper surface of the impingement wall represents fuel adhesion. Figure 4.20 (a), and (b) respectively represent single injection under static flow and cross-flow conditions. Under cross-flow conditions, more volatilization of droplets, and the droplets flow with cross-flow, not reattach to the wall, resulting in a large fuel adhesion area and a thin thickness. Figure 4.20 (c), and (d) respectively represent triple injection under static flow and cross-flow conditions. Under static flow conditions, the high velocity droplets of the third injection will collide with the low-velocity droplets of the first/second injection, thereby accelerating the droplets in the air to adhere to the wall surface, and the evaporation of the droplets in the air is reduced, resulting in a larger fuel adhesion mass compared to single injection. Under cross-flow conditions, the high velocity droplets of the third injection will not collide with the droplets of the first/second injection, because the droplets of the first/second injection are blown downstream by the cross-flow. Under cross-flow conditions, more droplets evaporate and the droplets flow with cross-flow, not reattach to the wall, resulting in the least fuel adhesion mass triple injection under cross-flow conditions.

Single injection

Non-break up/dense droplet core

t=4.0 ms ASOI

Splashing droplets

Impinging droplets

Volatilization of droplets

Fuel adhesion

(a) U_x=0m/s, single injection.

Single injection

Non-break up/dense droplet core

t=4.0 ms ASOI

Cross-flow U_x=30m/s

Splashing droplets

More volatilization of droplets

Impinging droplets

Thin fuel adhesion

Droplets flow with the cross-flow, do not reattach to wall.

(b) U_x=30m/s, single injection.

Non-break up/dense droplet core

Triple injection

t=8.1 ms ASOI

High velocity droplets of third injection

Low velocity droplets of second/first injection

Splashing droplets

Impinging droplets

Volatilization of droplets

Fuel adhesion

(c) U_x=0m/s, triple injection.

Triple injection

3rd

Non-break up/dense droplet core

t=8.1 ms ASOI

High velocity droplets of third injection

Cross-flow U_x=30m/s

Splashing droplets

More volatilization of droplets

2nd

Impinging droplets

Low velocity droplets of second injection

Thin fuel adhesion

Droplets flow with the cross-flow, do not reattach to wall.
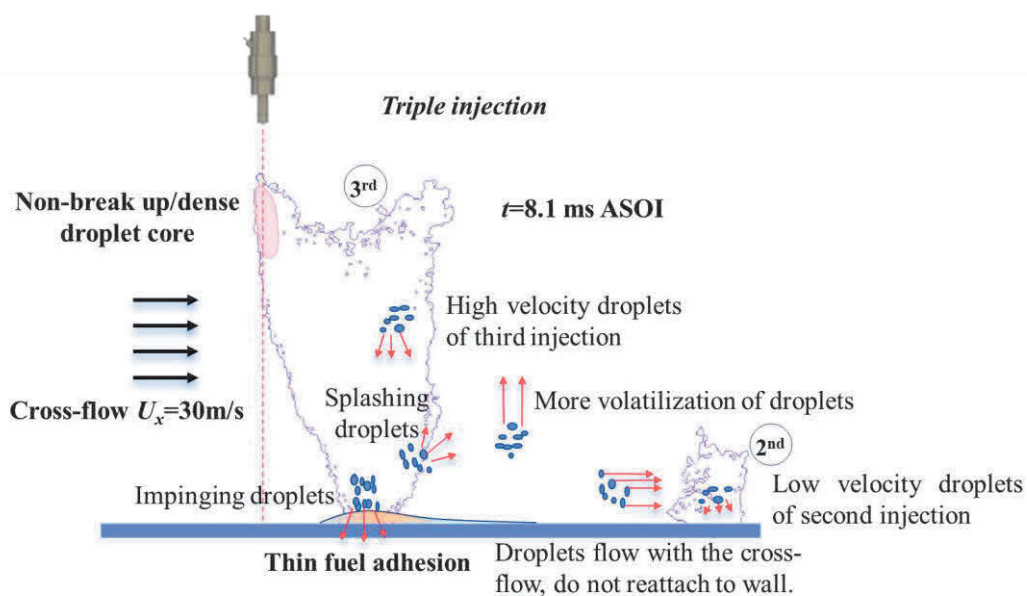
(d) U_x=30m/s, triple injection.

Figure 4.20 Mechanism of fuel adhesion formation.

4.5 Summary

Fuel adhesion caused by spray impingement has a significant impact on the performance of DISI engines. In this chapter, the RIM method is mainly employed to investigate the effect of split injection on wall-impingement spray and the fuel adhesion characteristics under static flow and cross-flow field conditions. The specific findings are as follows.

(1) Under static-flow conditions, the second and third sprays collide with the residual spray from previous injections before reaching the wall. However, under cross-flow conditions, the second and third sprays do not collide with the residual spray from the first and second injections before reaching the wall.

(2) Initially, the fuel adhesion area increased and then slightly decreased with time in the static flow field. However, in the cross-flow field, the fuel adhesion area initially increased and then decreased dramatically with time because cross-flow can promote the diffusion and evaporation of fuel adhesion. Additionally, triple injection further reduces the fuel adhesion area in the cross-flow field because the fuel spray is more likely to be atomized and evaporated during a long exposure time. In contrast, the fuel adhesion area of triple injection is the largest in the static flow field because split injection increases the ductility of fuel adhesion on a wetted flat-wall.

(3) The fuel adhesion mass is stable in the static flow field at a later stage, whereas it gradually decreases with time in the cross-flow field because the cross-flow encourages the evaporation of fuel adhesion. Additionally, the fuel adhesion mass of the triple injection is the smallest in the cross-flow field because the injection mass of each segment decreases with the increase in the number of injections, and the fuel spray of each segment has enough time to be atomized and blown downstream far from the wall. In contrast, the fuel adhesion mass of the triple injection is the largest in the static flow field because the droplet kinetic energy of the previous injection increased by later injection, accelerating their adhesion to the flat-wall.

(4) The average fuel adhesion thickness in the cross-flow field is much smaller than that in the static flow field, which is also attributed to the cross-flow promoting the evaporation of fuel adhesion. Additionally, the average fuel adhesion thickness of the triple injection is the smallest under static flow and cross-flow field conditions.

(5) The fuel adhesion deformation coefficient I_d is close to 1 in the static flow field, whereas it is quite large in the cross-flow field, implying that the cross-flow has a significant impact on the distribution of fuel adhesion. Under the static flow field conditions, the distribution of the fuel adhesion thickness is concentrated near the thicker peak, whereas the distribution shifts to a thinner peak in the cross-flow field. Meanwhile, the peak value of split injection decreased with time under cross-flow field conditions.

CHAPTER 5 EFFECT OF VARIOUS CROSS-FLOW VELOCITY ON FUEL ADHESION CHARACTERISTICS

5.1 Introduction

In engines, air and fuel mix through injection and interact with Although some related investigations have been conducted on the impact of cross-flow on fuel adhesion properties, the influence of cross-flow velocity on fuel adhesion of split and wall-impingement spray remains unexplored. The impact of cross-flow velocity on the impingement spray and fuel adhesion in the context of the split injection strategy has been largely overlooked. Therefore, this chapter investigates the impingement spray and fuel adhesion based on the following three aspects. First, the continuous wave laser-Mie scattering technique is utilized to spray properties in the vertical plane. Second, the RIM method is employed to evaluate the fuel adhesion. Third, the effects of varying cross-flow velocities on fuel adhesion and spray in the split injection strategy are investigated. This chapter has significant implications for enhancing the design and optimization of fuel injection strategies, thereby improving the combustion efficiency of engines and lower emissions.

5.2 Experimental Conditions

Experiments were conducted three times under each experiment condition, with the calculation of the mean and standard deviation of the data. The standard deviation values were denoted as error bars in this work. The experimental conditions are listed in Table 5.1. PIV technology was used to detect the uniformity of the flow field at different cross-flow velocities. To study the side view of the macroscopic sprays, the continuous wave laser-Mie scattering technique was applied. The RIM method was employed to obtain the fuel adhesion image.

Table 5.1 Experimental conditions.

Ambient condition	
Ambient pressure, P_a [MPa]	0.1
Ambient temperature, T_{tem} [℃]	25
Cross-flow velocity, U_x [m/s]	0, 10, 20, 30
Injection condition	
Injector type	Single hole
Hole diameter, D [mm]	0.15
Test fuel	Toluene
Injection pressure, P_{inj} [MPa]	10
Injection splitting strategies T_{inj}	Triple stage injection
Injection mass for $1^{st}, 2^{nd}$, and 3rd stage, m [mg]	2, 2, 2
Impingement condition	
Impingement distance, D_{imp} [mm]	75
Surface roughness, R_f [μm]	Ra 7.7
Shape of impingement wall [mm^2]	Rectangle 125× 70
Impingement wall	Frosted quartz glass

5.3 Image processing

Figure 5.1 depicts the image processing of spray/fuel adhesion during triple injection

with an impingement distance of 75 mm, a cross-flow velocity of 10 m/s, and a duration of T=10.2 ms ASOI). The red intersection position indicates the vertical projection point of the injector on the impingement wall.
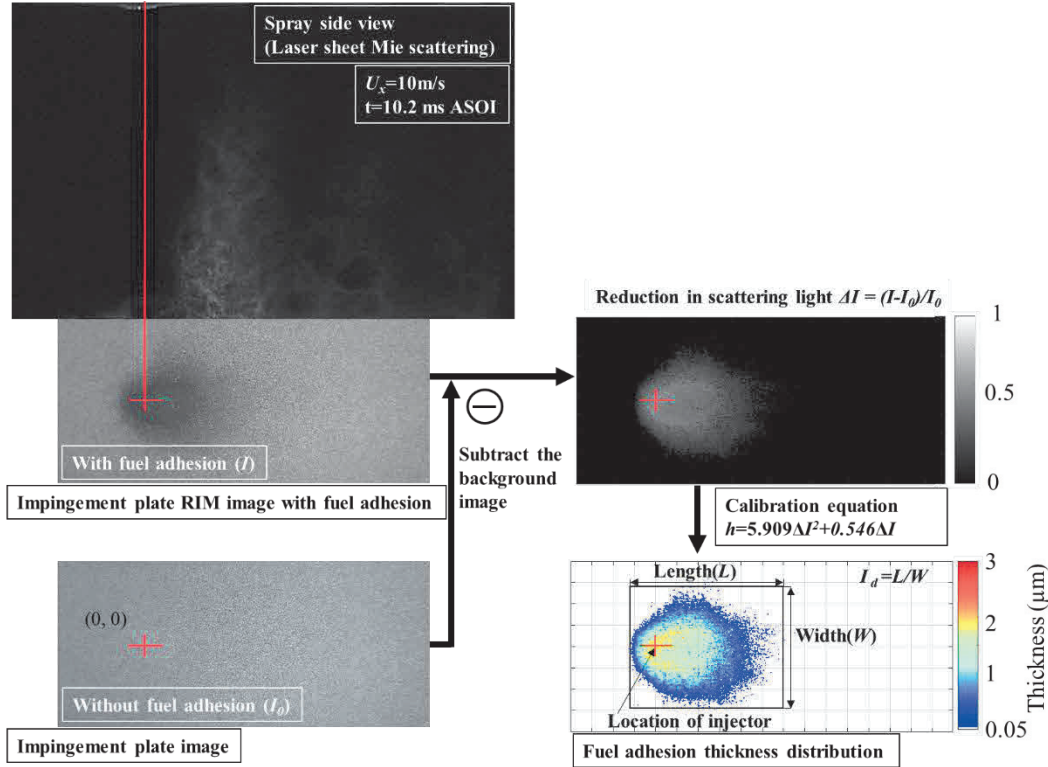
Figure 5.1 Image processing for spray fuel adhesion analysis.

In this study, the characteristics of fuel adhesion are examined in view of fuel adhesion area, mass, and thickness as assessment criteria. The experimental results represent the average values of three experiments under the same experimental condition. During the picture-processing process, the background image was first obtained by capturing the wall without fuel adhesion. Subsequently, an image of the impingement wall with fuel adhesion was acquired. By applying the light intensity values of both images to Equation (1), ΔI could be calculated, which represents the difference in light intensity. The calibration curve allows for a correlation between the changes in light intensity and the corresponding fuel thickness. Next, ΔI was utilized in conjunction with the calibration curve to calculate fuel adhesion thickness; the length along the x-axis direction and the width along the z-axis direction were also

defined in the image of fuel adhesion. Internal code processed in MATLAB was employed to determine the fuel adhesion characteristic. The intersection points projected directly by the nozzle on the glass plate below the nozzle are defined as the origin (0,0), which is indicated as a red cross in the spray and fuel adhesion images.

5.4 Results and Discussions

5.4.1 Wall-impingement spray in vertical plane

Figures 5.2 (a), (b), (c), and (d) illustrate the impact of different cross-flow velocities (0, 10, 20, 30 m/s) on the development process of wall-impinging spray under triple injection conditions at a constant impingement distance of 75 mm. In Figure 5.2, the time points of 0.8, 1.4, 4.7, 8.0, and 10 ms ASOI represent the stages when the spray has not yet contacted the wall, during the first injection, during the second injection, during the third injection, and during the post-evaporation stage of the spray, respectively. It can be seen from the figure that the higher the cross-flow velocity, the faster the spray moves downstream and the larger the spray area because the cross-flow promotes the diffusion of the spray downstream.
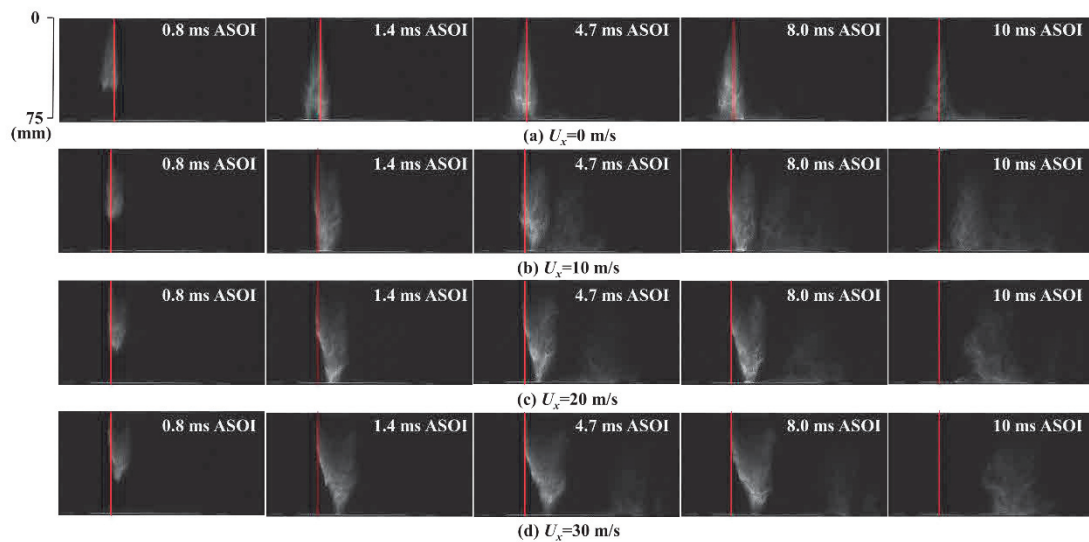
Figure 5.2 Side view of wall-impingement spray of different Cross-flow velocity.

Figure 5.3 shows the change in the vertical penetration of spray over time, and the

black line is the impingement distance. The black, blue, purple, and red hollow lines represent cross-flow velocities of 0, 10, 20, and 30 m/s, respectively. Under different cross-flow velocities, the time for the spray to hit the wall is basically the same, because cross-flow only promotes the horizontal propagation of spray and does not affect vertical propagation.
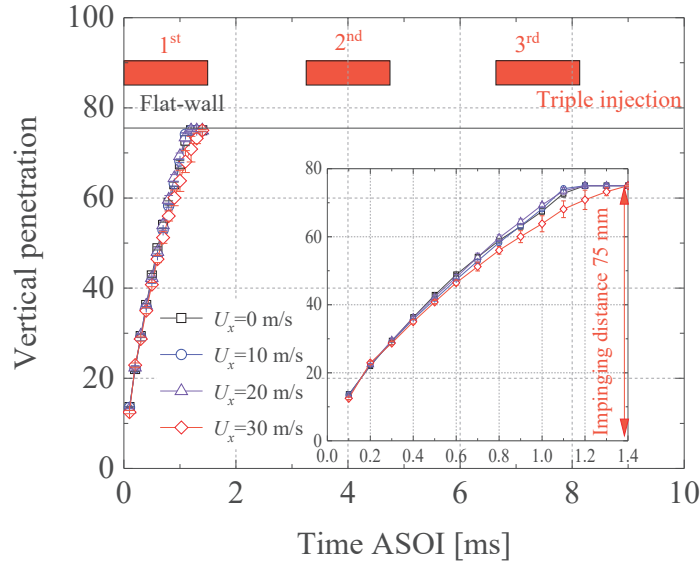
Figure 5.3 Spray vertical penetrations.

Figure 5.4 shows the change of spray horizontal penetration over time. With the increase of cross-flow velocity, spray horizontal penetration increases. This is because the spray promotes the lateral downstream propagation of the spray. The spray horizontal penetration of each stage of spray is first smooth upward and then fluctuates, which is consistent with Figure 4.6. However, when the cross-flow velocity is 10m/s, the spray horizontal penetration increases almost smoothly. This is because the previous stage spray is connected to the current stage spray without space interval. The detailed picture is shown in Figure 5.5.
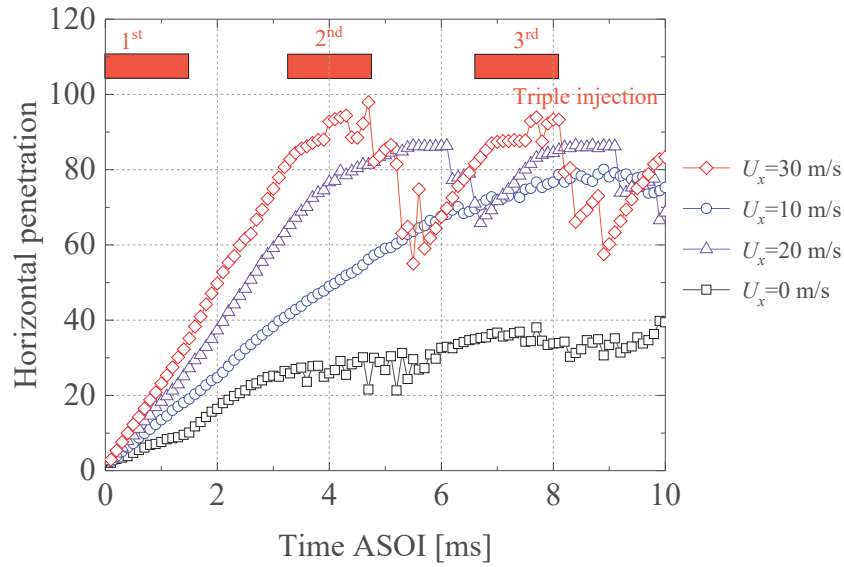
Figure 5.4 Spray horizontal penetrations.

Figure 5.5 (a), (b), and (c) respectively show the first spray, the first and second sprays, and the first, second, and third sprays. It can be seen from the figure that the sprays are almost connected as one.
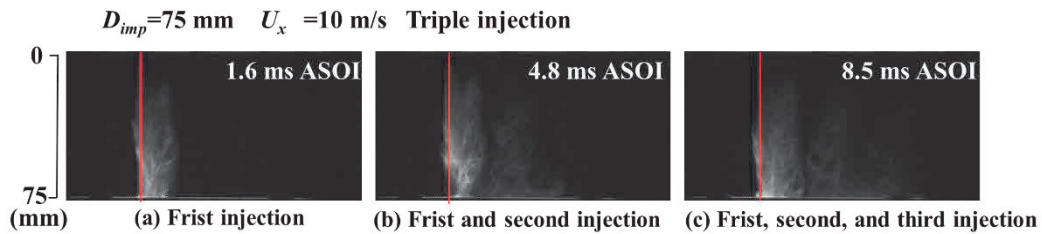
Figure 5.5 Detail of spray.

5.4.2   *Early stage analyses*

Figure 5.6 depicts the spray and fuel adhesion with white zone. When the RIM experiment was conducted, the Mie scattering of the spray caused the brightness value of the white zone in the fuel adhesion image to be higher than the background brightness of the impingement wall, that is, ΔI is less than 0. Therefore, the fuel adhesion analysis was distorted when the white zone appeared. This study does not analyze the period in which the white area ($\Delta I < 0$) appears.

94

To better analyze the development of spray and fuel adhesion, this study defines the 0-10 ms ASOI as the early stage, and the 10-100 ms ASOI as the later stage. After examining the origin images, the RIM measurable periods in the early stages are shown in Figure 5.7. All images in the later stage were available.
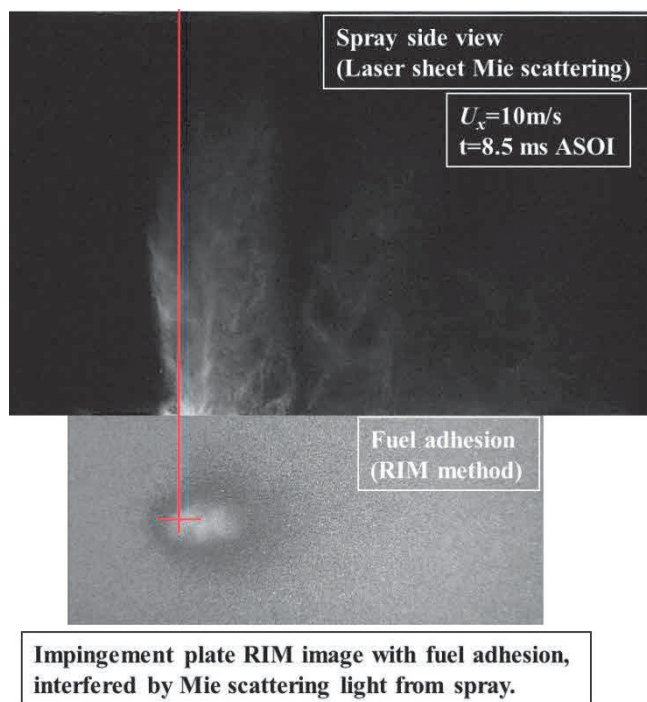
Figure 5.6 Fuel adhesion with white zone.
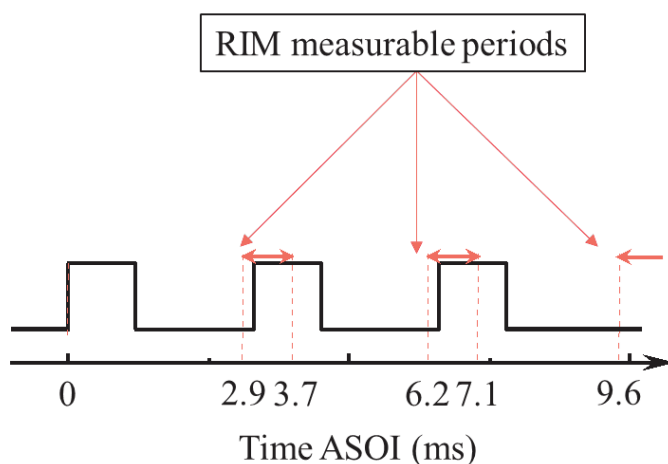
Figure 5.7 Measurable periods for fuel adhesion observation in early stage.

Figures 5.8 illustrate the fuel adhesion and side-view spray in the early stage with different velocities (0, 10, 20, and 30 m/s) in the triple injection. The color bars above,

with threshold ranges of 4%, 8%, 12%, 16%, 20%, 24%, and 28%, were determined based on the percentage of light intensity from the impingement wall spray, while those below reflects the fuel adhesion thickness, which spans from 0.05 to 3.0 μm. Figure 5.8 showed that at 0.6 ms ASOI, no fuel adhered to the impingement wall. The ASOI at 2.9, 6.2 and 9.6 ms represents where the first, second, and third injections just reached the time when no white area exists on the wall, respectively, marking the starting point for obtaining fuel adhesion data.
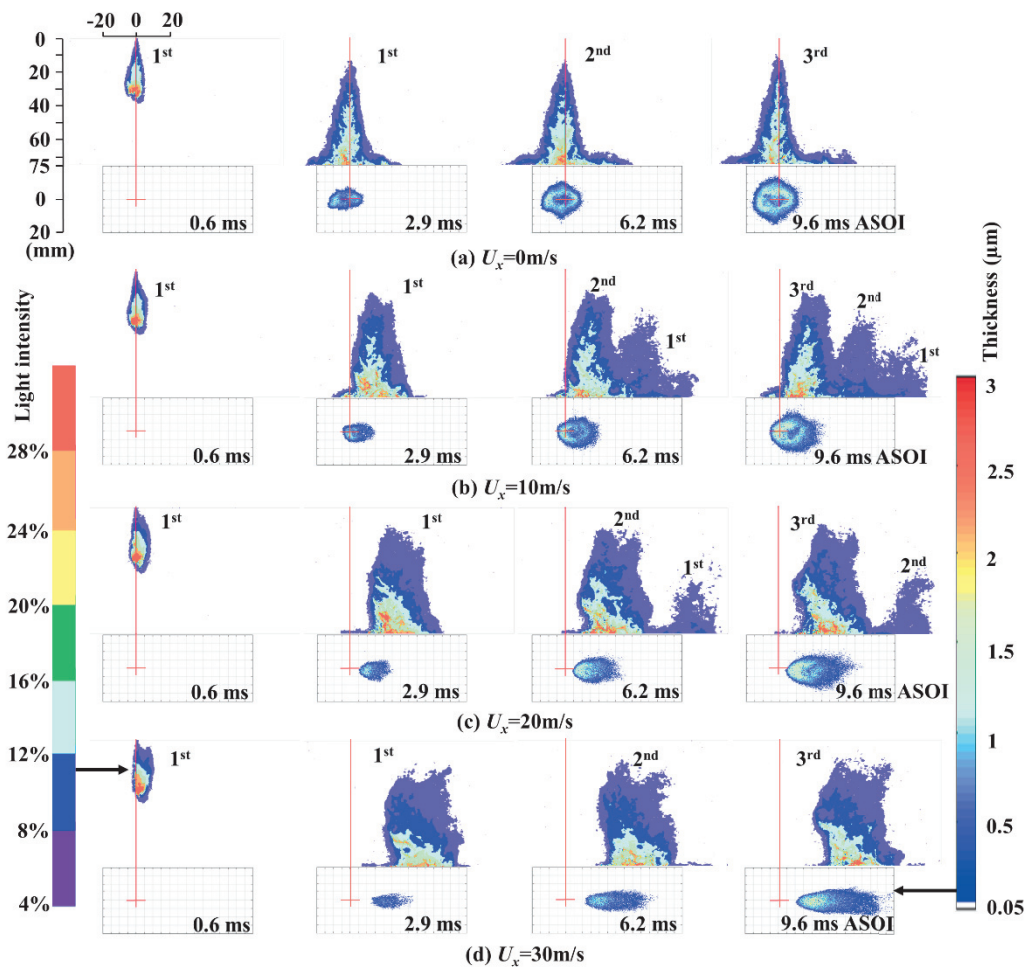
Figure 5.8 Fuel adhesion and spray characteristic in early stage.

As shown in Figure 5.8, when the cross-flow velocity was low (0-10 m/s), the cross-flow caused sprays of different segments to overlap and cross in space, thereby interfering with each other. Conversely, when the cross-flow velocity was high (20-30 m/s), a stronger cross-flow separated the spray of different segments in the space; this

is because the strong cross-flow causes the sprays of each segment to move downstream quickly, thereby avoiding the crossing and overlapping of the sprays of each segment. As cross-flow velocity increased, the fuel adhesion length lengthened; this is attributed to the increased lateral velocity and kinetic energy of the fuel droplets caused by higher cross-flow velocities, which enable them to overcome adhesion and friction forces and facilitate fuel adhesion to move laterally. Additionally, the width of the spray is much bigger than the length of the fuel adhesion, as not all spray droplets adhere to the wall, and splashing and rebound occur when the spray droplets hit the wall [131].

When studying the fuel adhesion characteristics, the black, blue, purple, and red dotted lines represent the fuel adhesion at velocities of 0, 10, 20, and 30 m/s, respectively.

In the early stage, the fuel adhesion area with time is shown in Figure 5.9. Figure 5.9 illustrates that the fuel adhesion area growth rate rose in the early stages as the cross-flow velocity rose. This is because, with a rise in the cross-flow velocity, the spray droplets accelerate to spread in the cross-flow direction, which leads to rapid adhesion of the spray droplets to the wall.
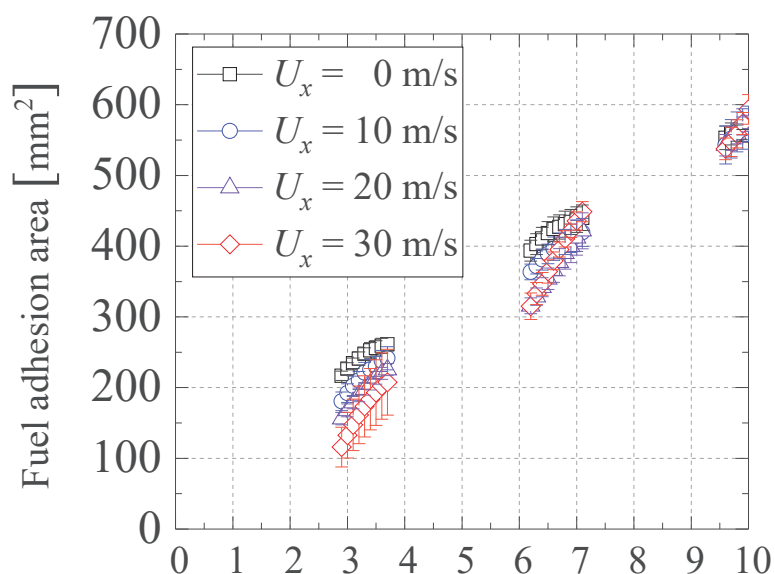
Figure 5.9 Process of fuel adhesion area in early stage.

The fuel adhesion area declined with rising cross-flow velocity. Because of the large wall-impingement distance (D_{imp} = 75 mm), the cross-flow has a longer-lasting impact on the spray droplets. The higher cross-flow velocities encourage the rapid diffusion of spray droplets, whereas the higher cross-flow also encourages the atomization, breakup, and volatilization of the droplets, which ultimately blows tiny droplets downstream and decreases the fuel adhesion area. Even though a high cross-flow could accelerate the fuel adhesion volatilization, the volatilization speed is much slower than that of the completely broken-up spray droplets in the air; therefore, the fuel adhesion volatilization is negligible in the early stage.
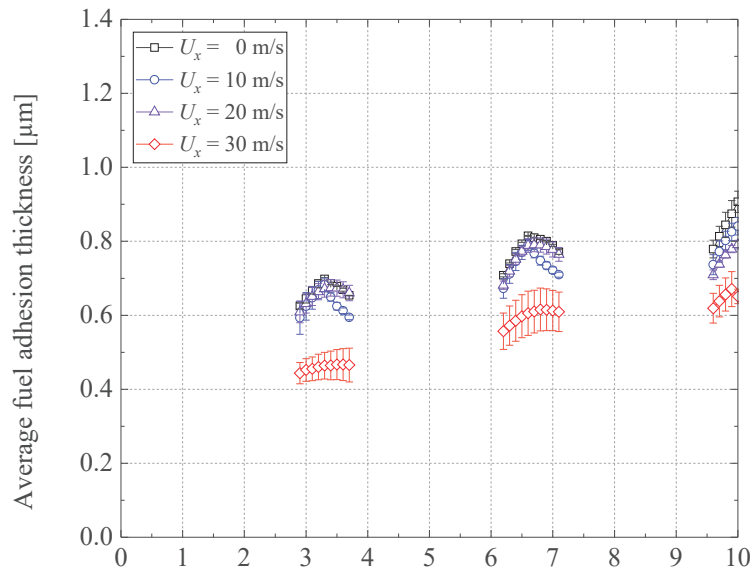
Figure 5.10 Process of fuel adhesion thickness in early stage.

Figure 5.10 illustrates the change in the average fuel adhesion thickness with time for the triple injection in the early stage. Figure 5.10 demonstrates a trend of the average fuel adhesion thickness first increasing and then decreasing during the triple injection strategy in the early stage. This is attributed to the gradual improvement in the quantity of suspended droplets during the fuel injection process, which raises the

average fuel adhesion thickness. Subsequently, the thinner fuel adhesion region begins to expand to the periphery, increasing the average fuel adhesion area, and consequently decreasing the average fuel adhesion thickness.
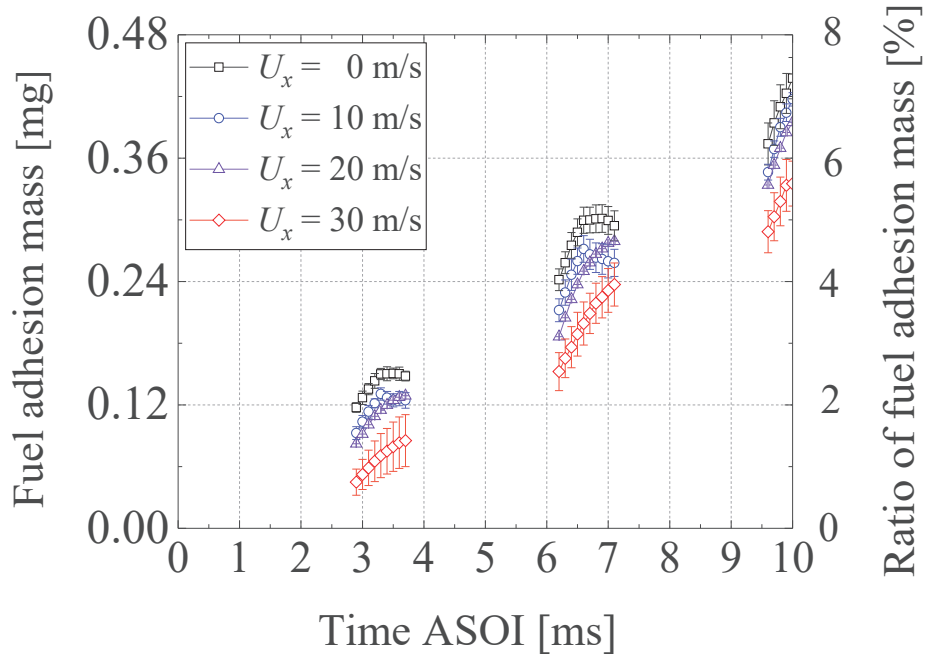
Figure 5.11 Process of fuel adhesion mass and mass ratio in early stage.

Figure 5.11 depicts how the fuel adhesion mass ratio (fuel adhesion mass/total injected mass) and mass have changed over time in the early stage. ASOI time is represented by the horizontal axis. Figure 5.11 demonstrates that during the early stage, the fuel adhesion mass increased over time. This is because the number of suspended droplets in the air gradually increases over time and continuously adheres to the wall, leading to a rise in the fuel adhesion mass. fuel adhesion mass declined as cross-flow velocity rose. This is because the fuel adhesion area and thickness declined with rising cross-flow velocity, leading to a decrease in the fuel adhesion mass.
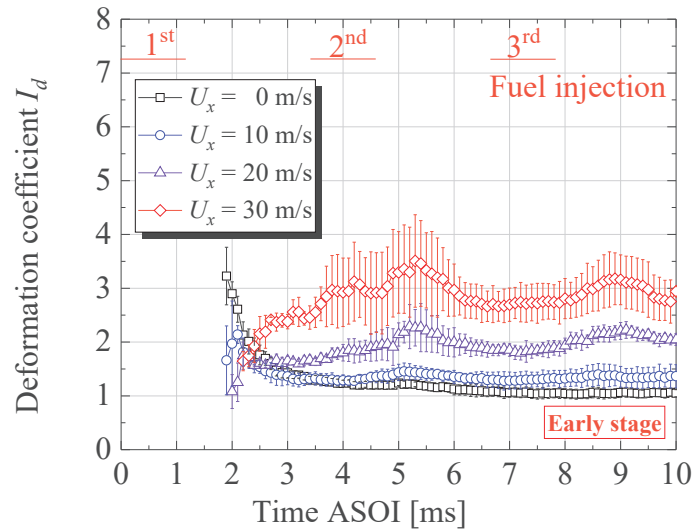
Figure 5.12 Process of fuel adhesion deformation coefficient I_d in early stage.

Figure 5.122 shows the Process of fuel adhesion deformation coefficient I_d with time in the early stage. The fuel adhesion deformation coefficient increases with the increase of cross-flow velocity. This is attributed to the increased lateral velocity and kinetic energy of fuel droplets caused by higher cross-flow velocities, enabling them to overcome adhesion and friction forces, and facilitating adhesion to lateral positions farther away from the impingement point.

5.4.3   Later stage analyses

The evolution of the fuel adhesion at different velocities of 0, 10, 20, and 30 m/s in the later stage is depicted in Figure 5.13. The color bar on the right represents different fuel adhesion thicknesses ranging from 0.05 to 3.0 μm. As shown in Figure 5.13, higher cross-flow velocities accelerate the drift and dispersion of spray droplets; therefore, the fuel adhesion thickness reduced as cross-flow velocities rose in the thicker wall-impingement region, while the fuel adhesion area in the thinner edge region increased. This was because the cross-flow carried the spray droplets farther away from the center region of the injection, reducing the fuel adhesion thickness on the impingement wall. In addition, the overall position of the fuel adhesion shifted

towards the direction of the cross-flow with increasing cross-flow velocity because of the effect of cross-flow on the spray movement in the early stage. Meanwhile, the fuel adhesion length lengthened and the fuel adhesion width narrowed under the impact of the cross-flow; this is because the spray droplets are created by a higher cross-flow velocity to slide or roll in the horizontal direction on the impingement wall instead of spreading over a wider area, resulting in a reduced fuel adhesion width.
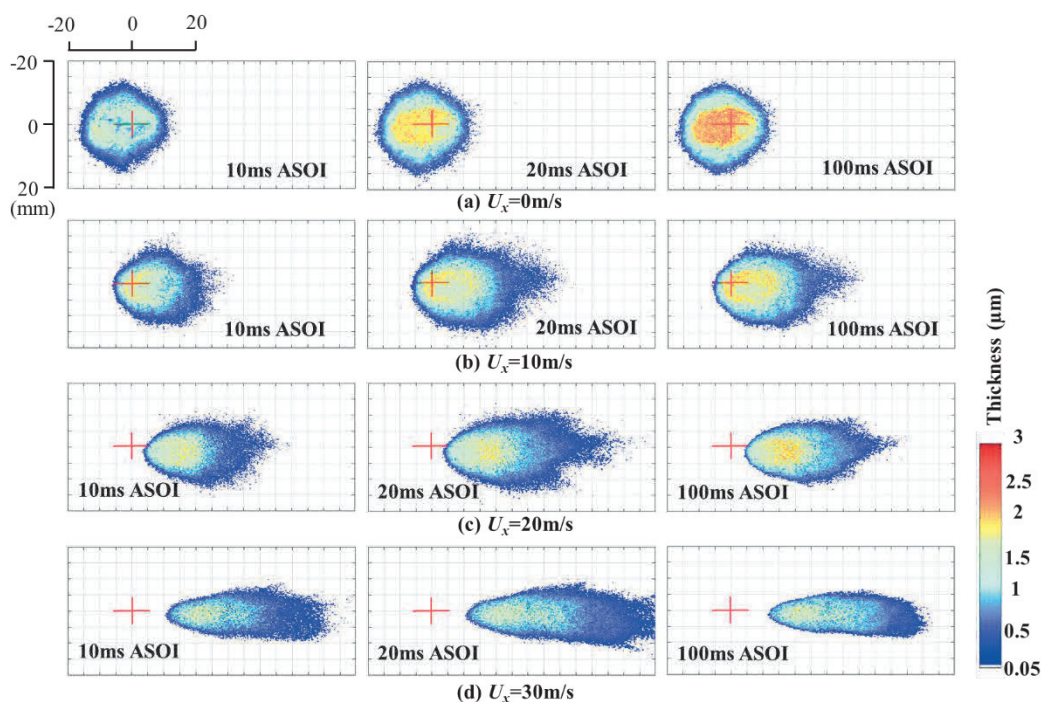
Figure 5.13 Process of fuel adhesion characteristic in later stage.

Figures 5.14 show the change with time for the fuel adhesion area in the later stage. As shown in Figure 5.14, under the triple injection conditions, the fuel adhesion area remained stable under no cross-flow conditions during the later stage. However, the fuel adhesion area first grew, then shrank under cross-flow conditions. When the cross-flow velocity rose, the rate of decrease in the fuel adhesion area intensified; this is attributed to the fact that there were still several spray droplets in the air initially which then adhered to the wall, leading to a rise in the fuel adhesion area. Subsequently, a few spray droplets were present in the air. Without cross-flow conditions, the fuel adhesion volatilized very slowly; therefore, the fuel adhesion area

shrank little. When the cross-flow velocity gradually rose, the rate of decrease in the fuel adhesion area also increased because the cross-flow promotes fuel adhesion volatilization; the higher the cross-flow velocity, the faster the volatilization. However, the rate of decrease of the fuel adhesion area did not always increase with the cross-flow velocity; that is, there was little difference in the rate of decrease of the fuel adhesion area between 20 and 30 m/s.
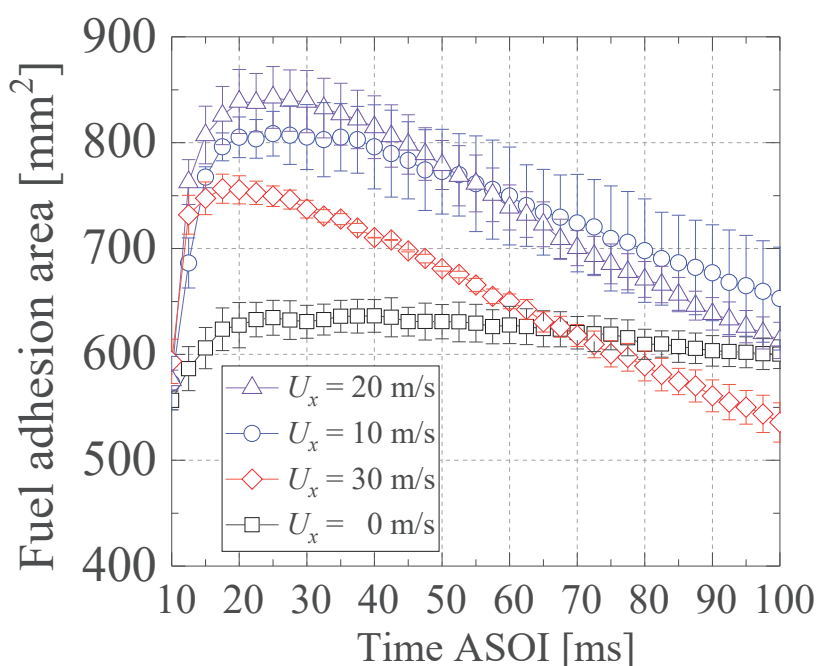
Figure 5.14 Process of fuel adhesion area in later stage.

Interestingly, the fuel adhesion area at 30 m/s was smaller than that at 10 and 20 m/s. To analyze the above phenomenon more intuitively, fuel adhesion at 25 and 75 ms ASOI is distributed in Figure 5.15. The fuel adhesion width at 30 m/s decreased sharply compared with that at 10 and 20 m/s. This is because, at a large impingement distance, higher cross-flow velocities raise the translational motion of the spray droplets in the air, imparting a greater horizontal velocity component upon impingement; this causes the spray droplets to slide or roll along the horizontal direction on the impingement wall rather than spread to a wider extent, causing the fuel adhesion width to narrow. Not only is the fuel adhesion area the result of the

combined effect of the length and width mentioned above, but a higher cross-flow makes the fuel spray bend significantly, and most droplets are blown downstream, resulting in a few droplets impinging on the flat-wall. In addition, when cross-flow velocity is 30 m/s, the fuel adhesion volatilizes faster. Therefore, the fuel adhesion area at 30 m/s was smaller than those at 10 and 20 m/s.
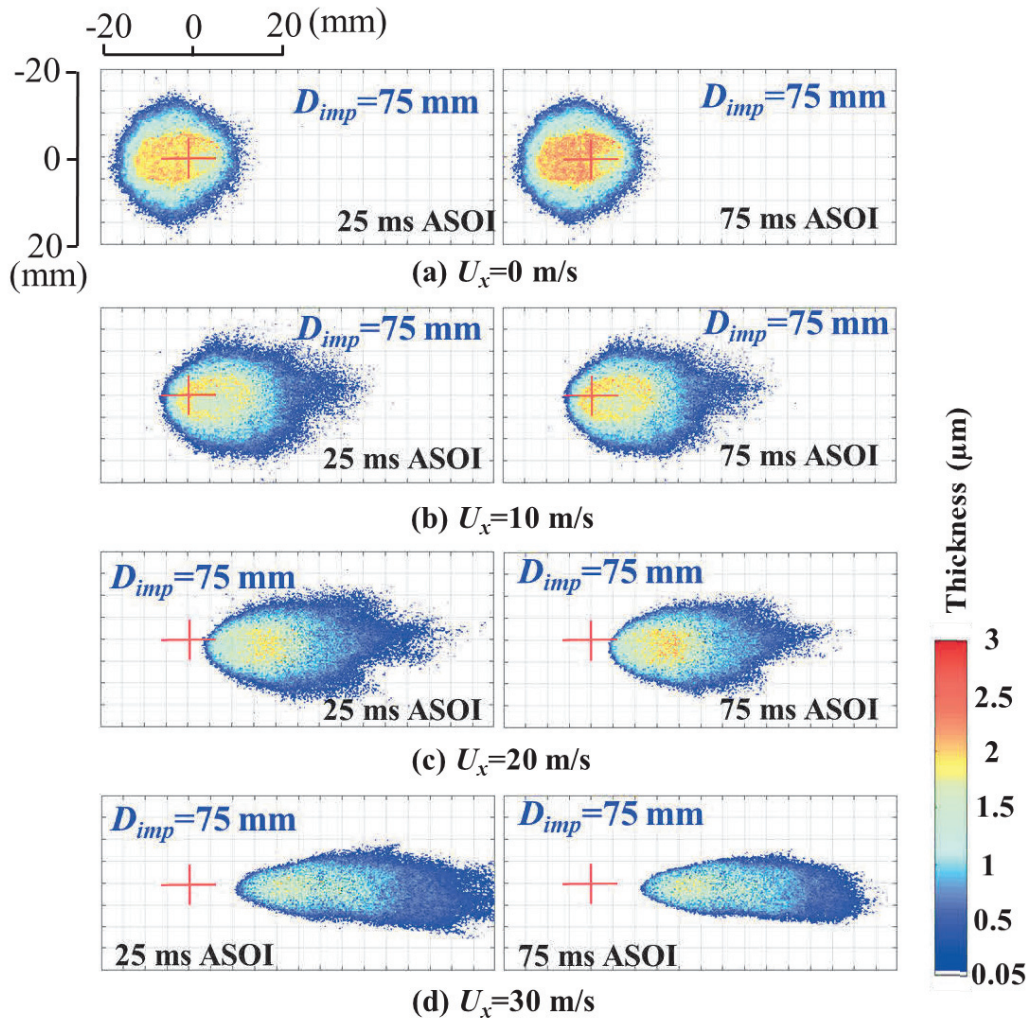
Figure 5.15 Detail of fuel adhesion in later stage.

Figure 5.16 illustrates the change over time for the average fuel adhesion thickness during the later stage. During the fuel adhesion process, as the cross-flow velocity rose, the fuel adhesion thickness reduced. The airflow near the fuel intensified as the cross-flow velocity increased. A higher cross-flow velocity results in greater air turbulence and eddy formation, which entrains or disperses the spray droplets, causing

the fuel to disperse into smaller droplets and reducing the likelihood of adhesion. In addition, higher cross-flow velocities encourage fuel adhesion to volatilize. In later stages, the average fuel adhesion thickness rose with time. This was attributed to a decline in the fuel adhesion area in the thinner edge region.
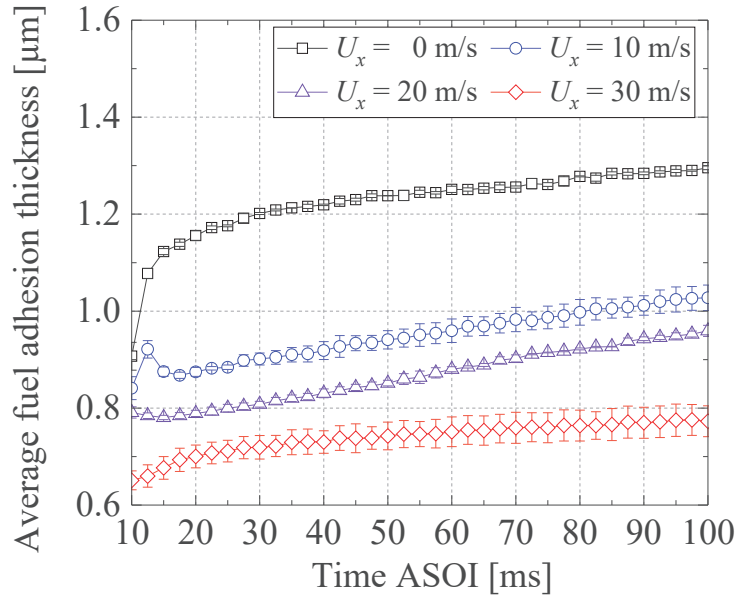
Figure 5.16 Process of fuel adhesion thickness in later stage.

Figure 5.17 illustrates the fluctuation in the fuel adhesion mass and adhesion mass ratio (fuel adhesion mass/total injection mass) with time during the late stage. ASOI time is represented by the horizontal axis. Fuel adhesion mass and mass ratio are represented by the left and right vertical axes, respectively. The fuel adhesion mass tends to stabilize and slightly increase under the no cross-flow condition in the later stage. This is because the movement of spray droplets in air is relatively stable and is less affected by external disturbances under no cross-flow conditions; consequently, the spray droplets are more likely to gradually adhere to the impingement wall and maintain a stable state, thereby slightly increasing the fuel adhesion mass. As the cross-flow velocities increase, the rate of decrease in the fuel adhesion mass also increases. Higher cross-flow velocity forces make it easier for the droplets to be blown away from the impingement point by the cross-flow, and the dispersal and

diffusion effects of the droplets reduce the chances of impingement on the impingement wall. These factors collectively contribute to the increased rate of decrease in the fuel adhesion mass.
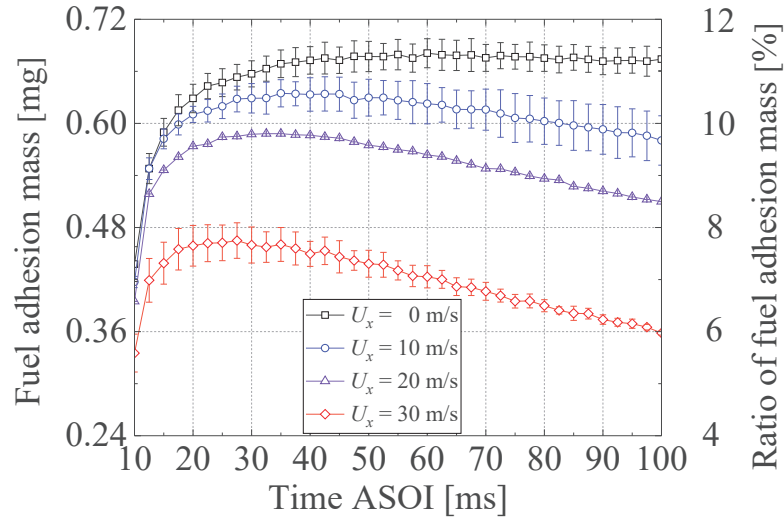
Figure 5.17 Process of fuel adhesion mass and mass ratio in later stage.

Figure 5.18 illustrates the temporal variation of the fuel adhesion deformation coefficient. As the cross-flow velocity increases, the fuel adhesion deformation coefficient also increases. This is because higher cross-flow velocities enhance the translational motion of fuel droplets in the air, resulting in greater kinetic energy. When these high-energy droplets come into contact with the impingement plate, they exhibit a larger horizontal velocity component after the collision. This causes the fuel droplets to slide or roll along the horizontal direction on the impingement plate, resulting in an elongated adhesion shape.
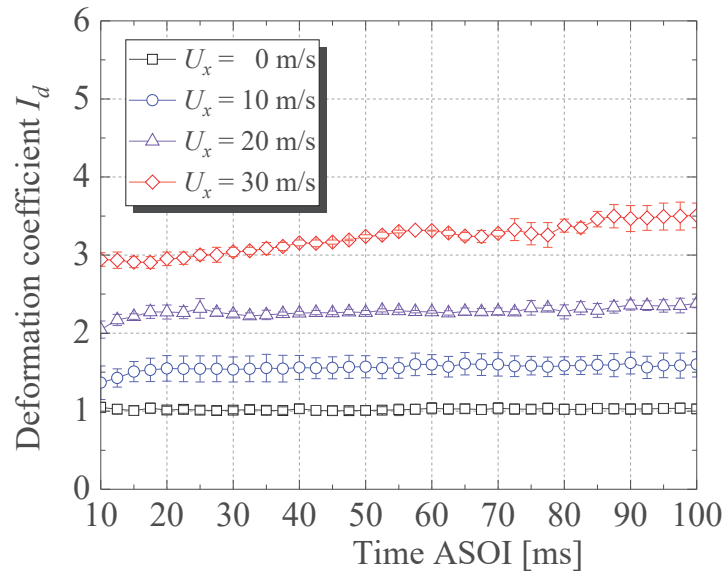
Figure 5.18 Process of fuel adhesion deformation coefficient I_d in later stage.

5.4.4 *Maximum fuel adhesion characteristics*

Figures 5.19 (a), (b), and (c) show the variations in the maximum fuel adhesion area, average thickness, and mass with the cross-flow velocity, respectively. Figure 5.19 (a) shows that the maximum fuel adhesion area is largest at U_x= 20 m/s. The findings are consistent with those presented in Figure 5.14. Figure 5.19 (b) shows that the maximum average fuel adhesion thickness reduces as cross-flow velocities rise, and the results are consistent with the results in Figure 5.16. Figure 5.19 (c) demonstrates that when cross-flow velocities rise, the maximum fuel adhesion mass falls. The maximum fuel adhesion mass at 20-30 m/s drops sharply. To analyze this mechanism, details of the fuel adhesion at the maximum fuel adhesion mass for cross-flow velocities of 20 and 30 m/s are shown in Figure 5.20. The fuel adhesion length for the 30 m/s condition increased but the width decreased sharply; this is because higher cross-flow velocities enhance the translational motion of spray droplets in air, resulting in greater kinetic energy. When these energetic droplets come in contact with the impingement wall, they exhibit a large horizontal velocity component after impingement. This causes the spray droplets to slide or roll in the horizontal direction

on the impingement wall, resulting in an elongated cohesive shape.
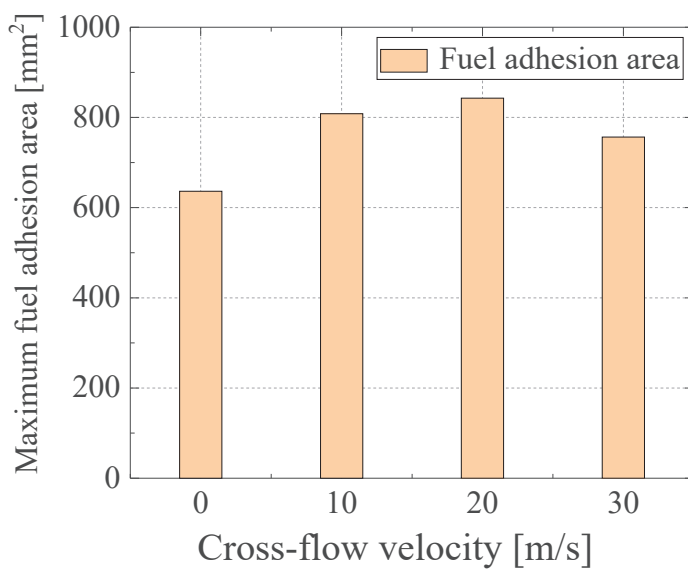
(a) Maximum fuel adhesion area.
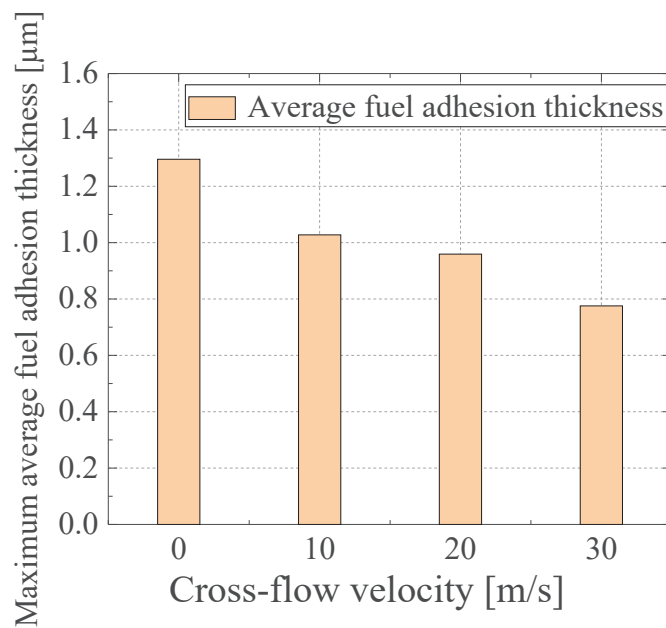
(b) Maximum average fuel adhesion thickness.
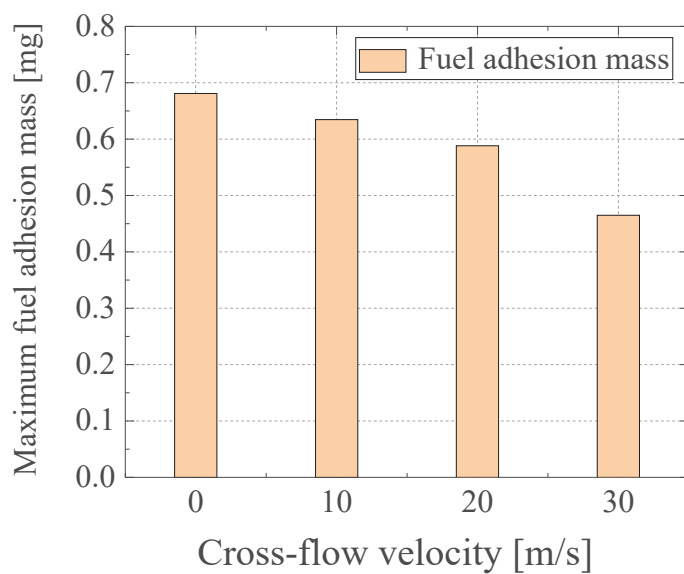
(c) Maximum fuel adhesion mass

Figure 5.19 Maximum fuel adhesion characteristics.
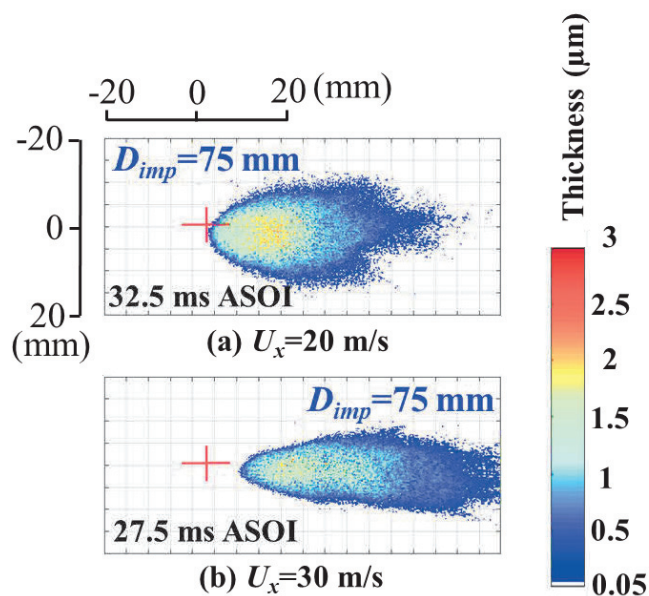
Figure 5.20 Detail of fuel adhesion at maximum fuel adhesion mass.

5.4.5 *Fuel adhesion distribution*

Figures 5.21 (a), and (b) show the connection between the fuel adhesion thickness and mass at two different times (10 and 100 ms ASOI).
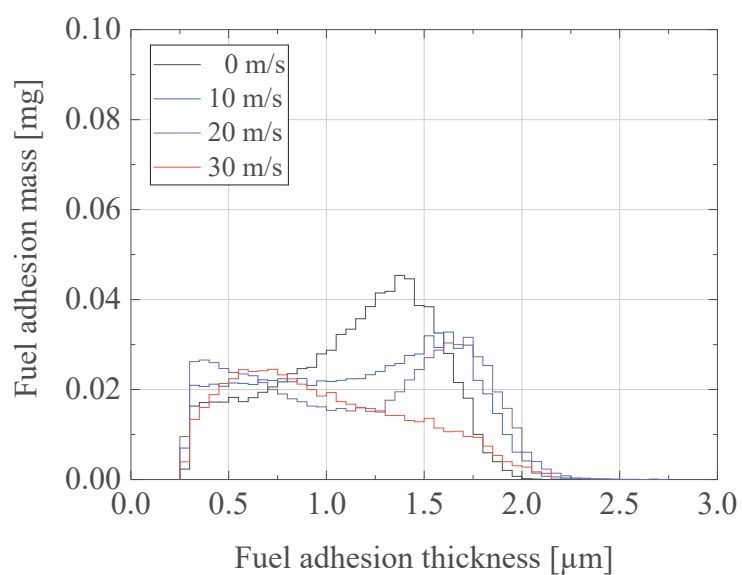
(a) T = 10 ms ASOI.
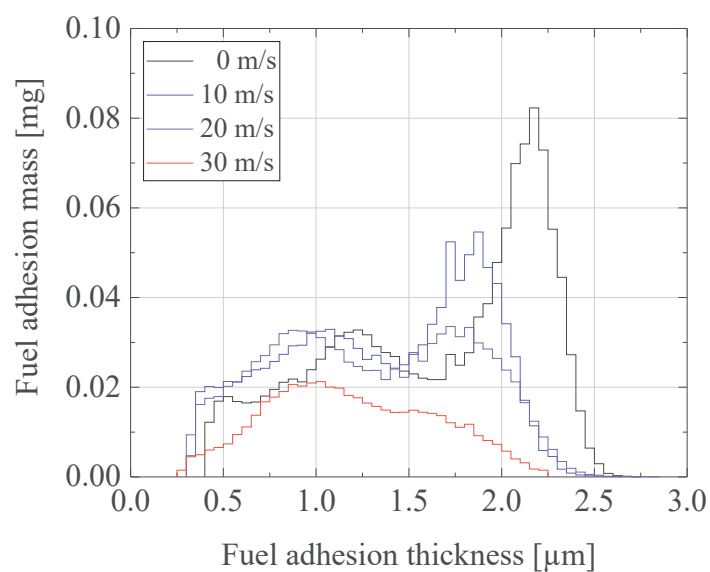
(b) T = 100 ms ASOI.

Figure 5.21 Connection between the thickness and mass of fuel adhesion.

Figures 5.21 (a) and (b) show that there were also two peaks during 0-20 m/s, whereas only one peak appeared in the thinner regions at 30 m/s. A large impingement distance and higher cross-flow velocity cause spray droplets to move in the air for a

longer time and produce more dramatic changes in airflow and turbulence effects; therefore, spray droplets are more uniformly produced in the spray region and adhere to the flat-wall, meaning that a thinner peak occurs. As the cross-flow velocity increases, the larger peaks show a decreasing trend, indicating that the fuel adhesion mass in the thicker region gradually decreases as the cross-flow velocity increases. This phenomenon can be attributed to the fact that higher cross-flow velocities create significant turbulence and shear forces, and the spray becomes more dispersed. The dispersed spray contributes to a more even distribution of fuel over the wall surface, resulting in a gradual decrease in the fuel adhesion mass in thicker areas. Especially in the 100 ms ASOI, when there is no cross-flow, the fuel adhesion mass in the thicker regions increases dramatically. This is because, in the absence of cross-flow, the spray droplets are not affected by the airflow and are more likely to adhere to the wall, resulting in increased fuel adhesion.

5.4.6   *Mechanism of fuel adhesion formation*

Figures 5.22 (a), and (b) illustrate the different mechanisms of fuel adhesion development under cross-flow velocities of 10 and 30 m/s. The purple line boundary represents the spray profile after the injection is completed, and the red dotted line represents the axis of the injector. The blue broad line at the bottom represents the impingement wall, and the upper surface of the impact plate represents the fuel adhesion. The higher the cross-flow velocity, the more droplets evaporate, and the droplets flow with cross-flow, not reattach to the wall, which will cause the fuel adhesion mass and thickness to decrease.
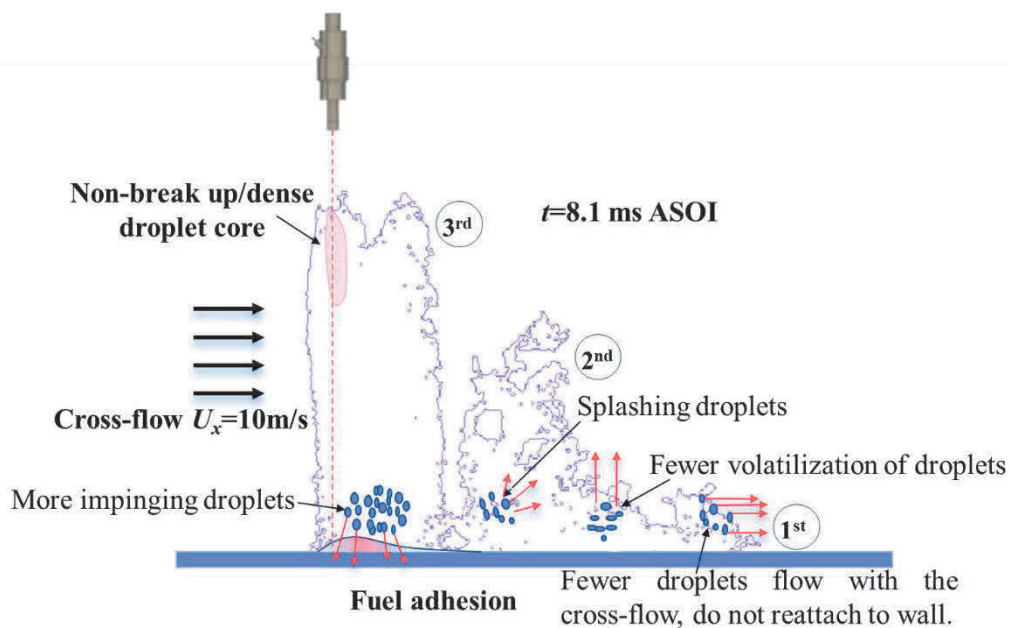
(a) U_x=10 m/s
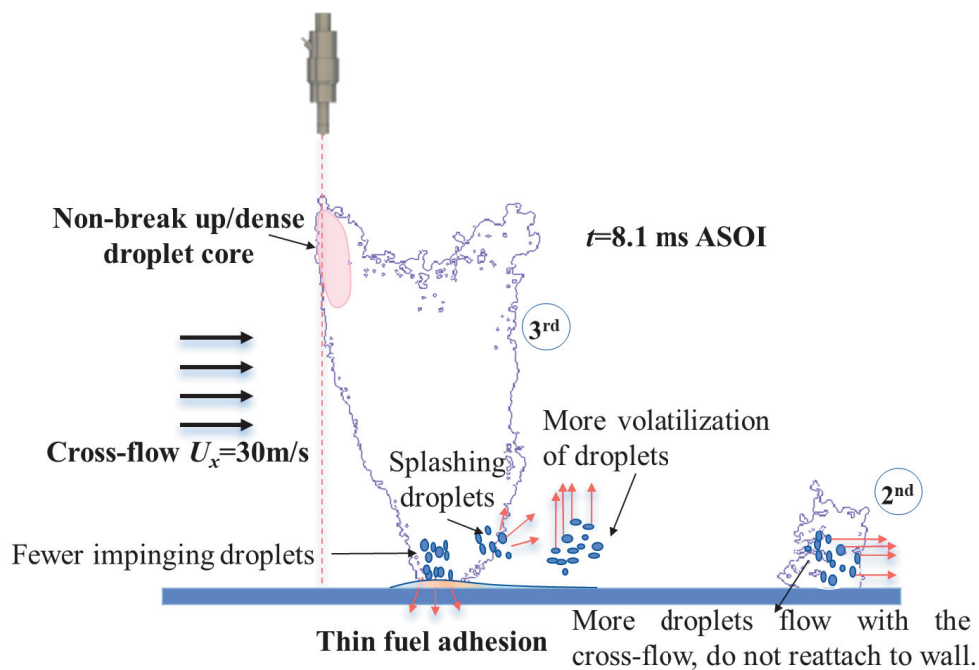
(b) U_x=30 m/s

Figure 5.22 Connection between the thickness and mass of fuel adhesion.

5.2 Summary

Effectively reducing the fuel adhesion caused by spray impingement on the wall is

crucial for enhancing DISI engines performance. The split injection examination, the continuous wave laser-Mie scattering technique, and the RIM methods were integrated with this chapter to analyze the spray distribution and fuel adhesion under different cross-flow velocities. The results are summarized as follows:

(1) Under cross-flow conditions, the horizontal penetration of split injection spray drops sharply because the previous spray disappears under the action of cross-flow. With the increase of cross-flow velocity, the faster the spray moves downstream, and the larger the spray area, the spray horizontal penetration increases, but the time for the spray to hit the wall is basically the same.

(2) In the early stage, the growth rate of the fuel adhesion area rose with increasing cross-flow velocity, whereas in the later stage, the decrease rate of the fuel adhesion area initially increased with increasing cross-flow velocity. However, when the critical velocity threshold (20 m/s) was exceeded, the decrease rate in the fuel adhesion area tended to stabilize.

(3) Increasing cross-flow velocities cause the fuel adhesion thickness to drop during the whole fuel adhesion process. As cross-flow velocity increases, intensified airflow enhances turbulence and eddy formation, dispersing spray droplets into smaller sizes and decreasing the likelihood of adhesion.

(4) During the later stage, the rate of reduction in the fuel adhesion mass increased as the cross-flow velocity rose. Stronger cross-flow forces facilitate downstream droplet movement, reducing impingement chances on the wall and contributing to an increased rate of fuel adhesion mass decrease.

CHAPTER 6 EFFECT OF VARIOUS IMPINGEMENT DISTANCE ON FUEL ADHESION CHARACTERISTICS

6.1 Introduction

The DISI engines have seen widespread adoption due to their notable attributes of low fuel consumption and high thermal efficiency. However, the compact internal volume and elevated injection pressure inherent to the DISI engines present challenges, leading to fuel adhesion on the piston surface and cylinder walls, resulting in pool fires and deposits. To address these challenges, a comprehensive study of spray-wall impingement dynamics within the DISI engine is crucial, with a particular focus on fuel adhesion characteristics. This chapter aims to bridge existing research gaps by conducting an in-depth investigation into the formation and propagation of fuel adhesion in wall-impinging sprays under cross-flow conditions, considering various wall-impingement distances. The specific focus is on analyzing the impact of different wall impingement distances on the fuel adhesion characteristics of split spray. Utilizing high-speed cameras and optical devices comprising laser sheets, the spray structure in a vertical plane will be observed, and the fuel adhesion characteristics will be studied using the RIM method. The study is structured to first analyze the early-stage impinging spray structure and fuel adhesion phenomena under cross-flow conditions and subsequently investigate fuel adhesion characteristics during the later stages of injection, including the area, average adhesion thickness, and mass of fuel adhesion.

6.2 Experimental Conditions

The experiments were conducted at room temperature and atmospheric pressure, with the injection pressure maintained at a constant 10 MPa. The transverse velocity of airflow was set at 10 m/s to simulate high-load conditions in an engine. Table 6.1 provides a more detailed overview of the experimental conditions.

Table 6.1 Experimental conditions.

Ambient condition	
Ambient pressure, P_a [MPa]	0.1
Ambient temperature, T_{tem} [℃]	25
Cross-flow velocity, U_x [m/s]	0, 10
Injection condition	
Injector type	Single hole
Hole diameter, D [mm]	0.15
Test fuel	Toluene
Injection pressure, P_{inj} [MPa]	10
Injection splitting strategies T_{inj}	Triple stage injection
Injection mass for $1^{st}, 2^{nd}$, and 3rd stage, m [mg]	2, 2, 2
Impingement condition	
Impingement distance, D_{imp} [mm]	25, 50, 75
Surface roughness, R_f [μm]	Ra 7.7
Shape of impingement wall [mm^2]	Rectangle 125× 70
Impingement wall	Frosted quartz glass

The frame rate is set to 10,000 fps. Table 6.2 shows photography conditions.

Table 6.2 Photography conditions.

Photography condition						
Optical methods<	Continuous wave laser-Mie scattering technique			RIM method		
Impingement distance D_{imp} [mm]	25	50	75	25	50	75
Frame rate [fps]	10,000	10,000	10,000	10,000	10,000	10,000
Frame size [pixels]	1152 × 560	1024 × 520	1024 × 520	960 × 448	960 × 448	960 × 448
Spatial resolution [pixels/mm]	5.3	5.3	5.3	9.6	10.2	10.7

6.3 Image processing

The experimental data represents the average values obtained from three repetitions under identical experimental conditions. The initial light intensity I_0 was obtained through background imagery. Subsequently, the fuel adhered to the impingement wall, resulting in the corresponding light intensity I, from which the change in light intensity ΔI was calculated. Combining the pre-established calibration curve in Figure 2.14 allows for the derivation of the thickness of the fuel adhesion. In addition to the fuel adhesion thickness, MATLAB is employed to obtain other characteristics of the fuel adhesion, such as the area and mass of the fuel adhesion. These characteristics are crucial for investigating the impact of the fuel adhesion process. In this experiment, the concepts of spreading and lateral spreading are introduced to describe the fuel adhesion distribution on the impingement wall. Define forward spreading, backward spreading, and lateral spreading as shown in Figure 6.1. The red cross symbol is positioned directly below the nozzle and serves as the origin point (0,0), intersecting

with the impingement wall, as detailed in Figure 6.1.
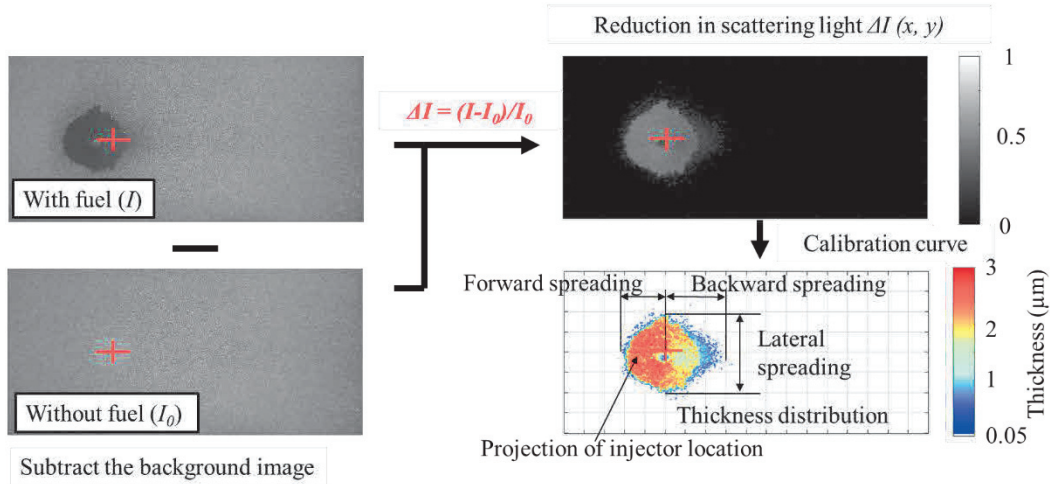
Figure 6.1 Image processing for fuel adhesion.

6.4 Results and Discussions

6.4.1 *Wall-impingement spray in vertical plane*

Figures 6.2 (a), (b), (c), and (d) illustrate the impact of different impingement distances (25, 50, 75 mm) on the development process of wall-impinging spray under triple injection conditions in a static-flow field (U_x = 0 m/s). In Figure 6.2, the time points of 0.3, 1.4, 4.7, 8.0, and 10 ms ASOI represent the stages when the spray has not yet contacted the wall, during the first injection, during the second injection, during the third injection, and during the post-evaporation stage of the spray, respectively. In the post-evaporation stage of the spray, as the impingement distance decreases, the spray evaporates/deposits more. As the impingement distance increases, the spray spreads more widely.
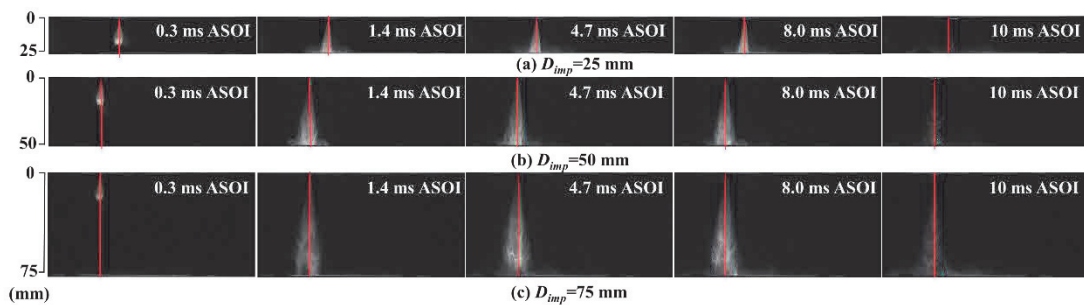
Figure 6.2 Side view of wall-impingement spray of different impingement distance. (Static flow field)
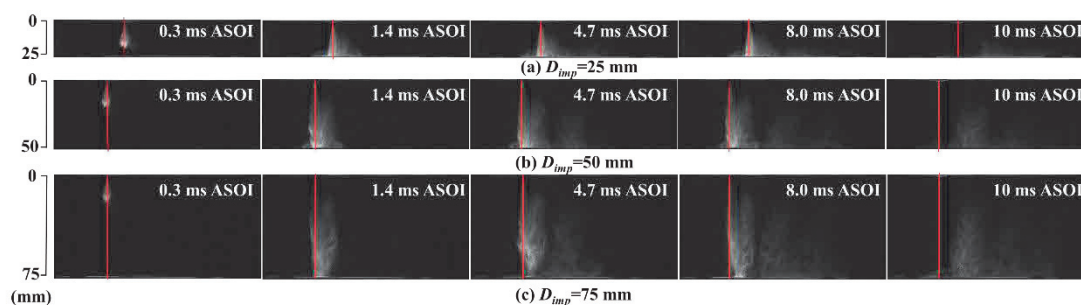
Figure 6.3 Side view of wall-impingement spray of different impingement distance. (Cross-flow flow field)

Figures 6.3 (a), (b), and (c) illustrate the impact of different impingement distances (25, 50, and 75 mm) on the development process of wall-impinging spray under triple injection conditions in a cross-flow field (U_x = 10 m/s). In cross-flow conditions the spray moves downstream. The smaller the impingement distance, the earlier the spray will hit the wall.

Figure 6.4 shows the change in vertical penetration of spray over time. The black, blue, and red lines represent the impingement distance of 25, 50, and 75 mm respectively. The solid line and hollow line represent the static flow field and the cross-flow field respectively. Under static flow and cross-flow conditions, the vertical penetration time of the same wall impingement distance is consistent. As the impingement distance increases, the impingement time also increases.
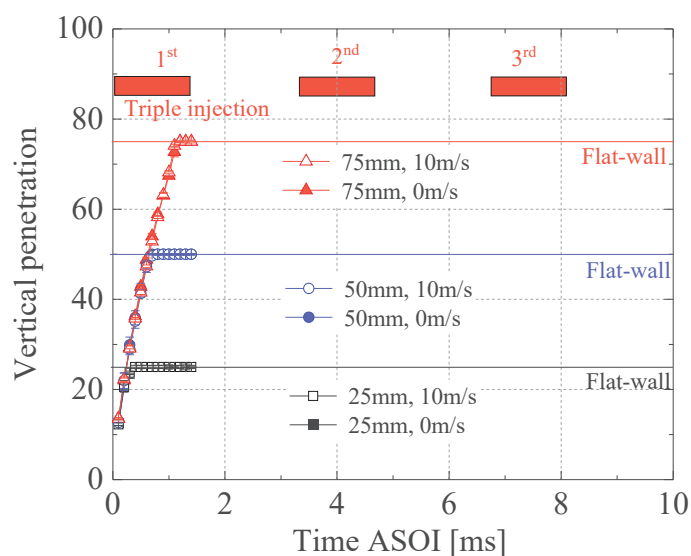
Figure 6.4 Spray vertical penetrations.

Figure 6.5 shows the change of spray horizontal penetration over time. Under cross-flow conditions, spray horizontal penetration increases. This is because cross-flow promotes the lateral diffusion of the spray. As the impingement distance increases, the spray horizontal penetration increases. This is because the higher the impingement distance, the longer the cross-flow affects the spray, resulting in higher spray horizontal penetration.
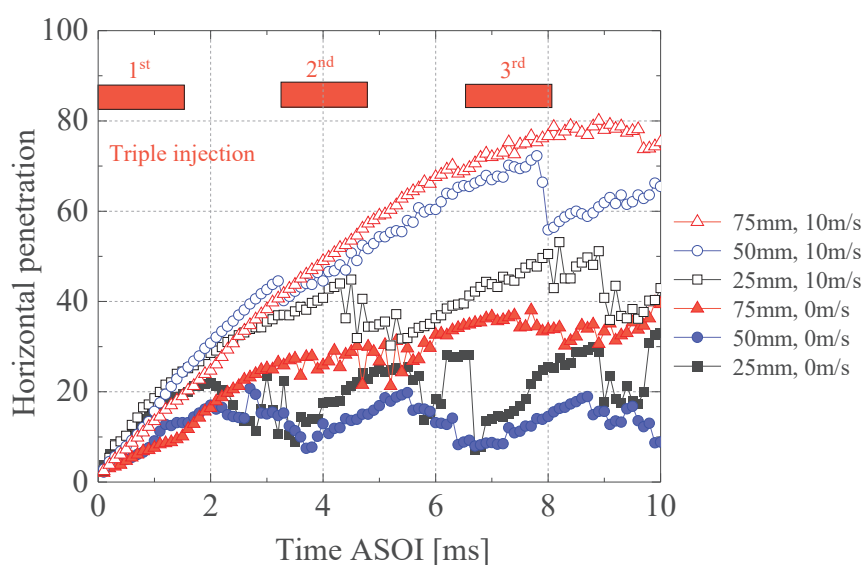
Figure 6.5 Spray horizontal penetrations.

6.4.2   Early stage analyses

Figures 6.6 and 6.7 (a), (b), and (c) respectively depict the early-stage split sprays and their fuel adhesion under static flow field and cross-flow conditions with impingement distances of 25mm, 50mm, and 75mm. Color bars representing fuel spray concentration and fuel adhesion thickness are positioned above and below, respectively. The first, second, third, and fourth columns of figures correspond to moments available for calculation during the first injection, and completion of the first, second, and third injections. From the figures, it can be observed that, regardless of the variation in impingement distance, the fuel adhesion length (the sum of forward spreading and backward spreading values) on the impingement wall is consistently smaller than the vertical length of the spray. This is attributed to the scale of the spray, encompassing pre-impingement and post-rebound, being much larger than the scale adhering to the impingement wall. Under the influence of cross-flow, the spray becomes asymmetrical and disperses downstream.
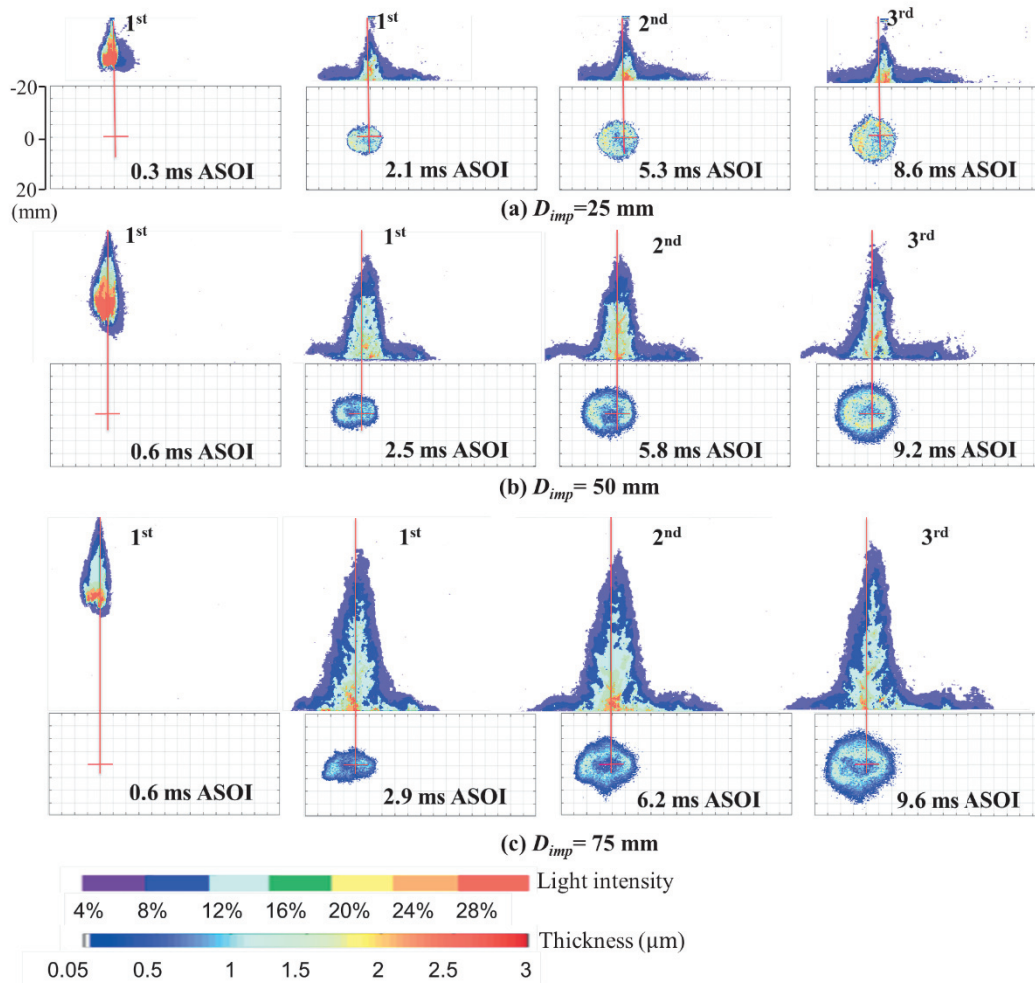
Figure 6.6 Side view of wall-impingement spray and fuel adhesion for different impingement distance at early stage (Static flow field).
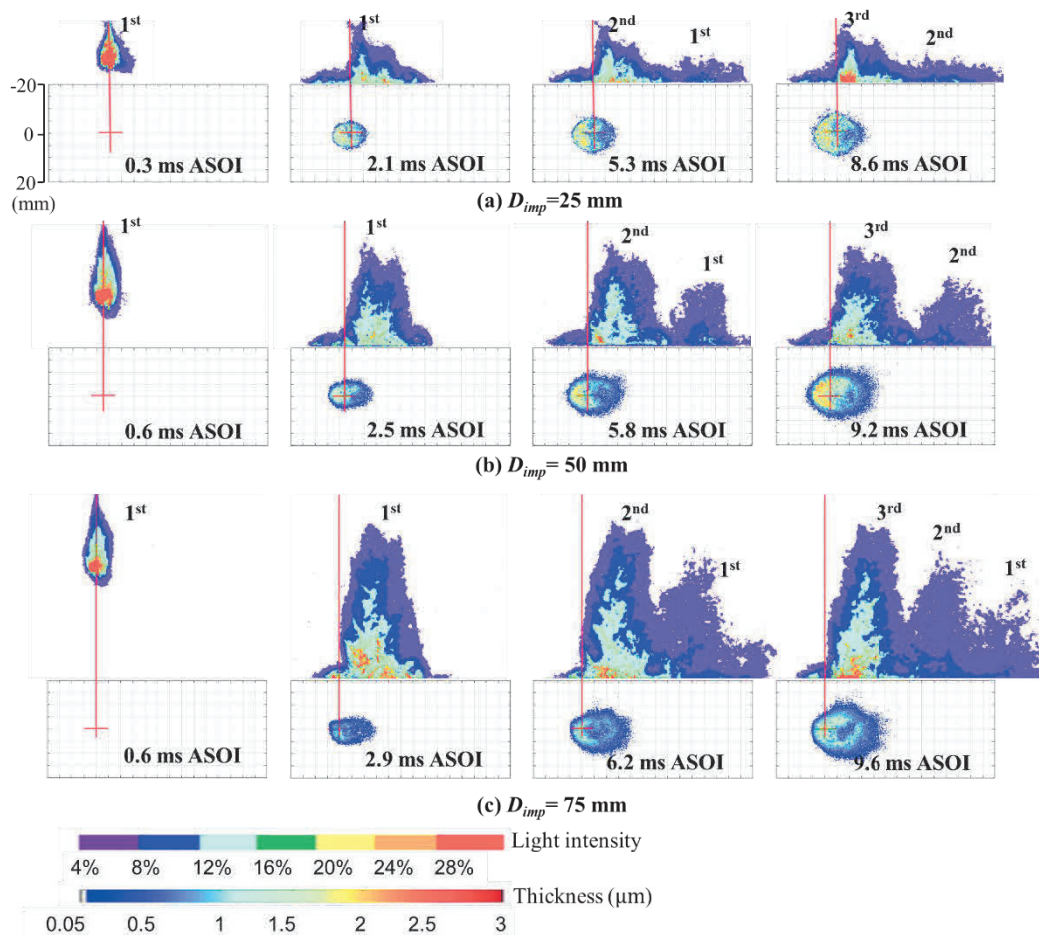
Figure 6.7 Side view of wall-impingement spray and fuel adhesion for different impingement distance at early stage (Cross-flow flow field).

Black, blue, and red solid, open dot line plots represent fuel adhesion at impingement distances of 25 mm, 50 mm, and 75 mm in the no cross-flow and under cross-flow conditions, respectively. Figure 6.8 illustrates the variation of fuel adhesion area over ASOI time for different impingement distances. In the early stages, when the wall impingement distance is low (25mm, 50mm), the fuel adhesion area under cross-flow conditions is slightly higher than that under no cross-flow conditions. However, when the wall impingement distance is higher (75mm), the fuel adhesion area under cross-flow conditions is slightly lower than that under no cross-flow conditions. This is because, at a lower wall impingement distance, the time for the spray to reach the impingement plate is shorter. The cross-flow increases the lateral kinetic energy of the spray droplets, promoting their lateral dispersion and resulting in a larger fuel adhesion area. In contrast, at a higher wall impingement distance, the time for the

spray to reach the impingement plate is longer. The cross-flow increases the lateral kinetic energy of the spray droplets even more, causing a significant increase in the lateral dispersion of the spray. Consequently, the spray droplets are blown downstream and cannot adhere to the impingement plate, leading to a decrease in the fuel adhesion area. As the impingement distance increases, the fuel adhesion area increases. As the impingement distance increases, spray droplets are more likely to diffuse and disperse in the air. This results in a wider distribution of droplets when attaching the wall, increasing the fuel adhesion area.
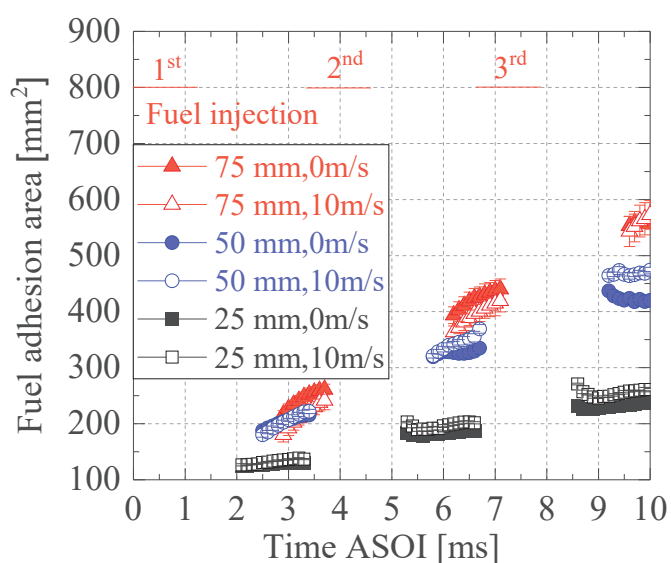
Figure 6.8 Development of fuel adhesion area at early stage.

Figure 6.9 depicts the variation of average fuel adhesion thickness over time at different impingement distances. According to Figure 6.9, during each injection process: when the wall impingement distance is 25mm, the average fuel adhesion thickness first increases and then stabilizes; when the wall impingement distance is 50mm, the average fuel adhesion thickness first increases and then slightly decreases; when the wall impingement distance is 75mm, the average fuel adhesion thickness first increases and then decreases. This is because as the spray gradually adheres to the wall surface, the fuel adhesion thickness initially increases. As the wall impingement distance increases, the dispersion of the spray is enhanced, resulting in

larger areas with thinner fuel layers, which leads to a decrease in the average fuel adhesion thickness. This phenomenon can be confirmed by Figures 6.6 and 6.7. Additionally, Figure 6.9 shows that the average fuel adhesion thickness declines with a rise in the impingement distance. As mentioned previously, as the impingement distance increases, the spray droplets have more time and space to be atomized, broken up, and volatilized before adhering to the wall, subsequently blowing downstream and reducing the fuel adhesion thickness.
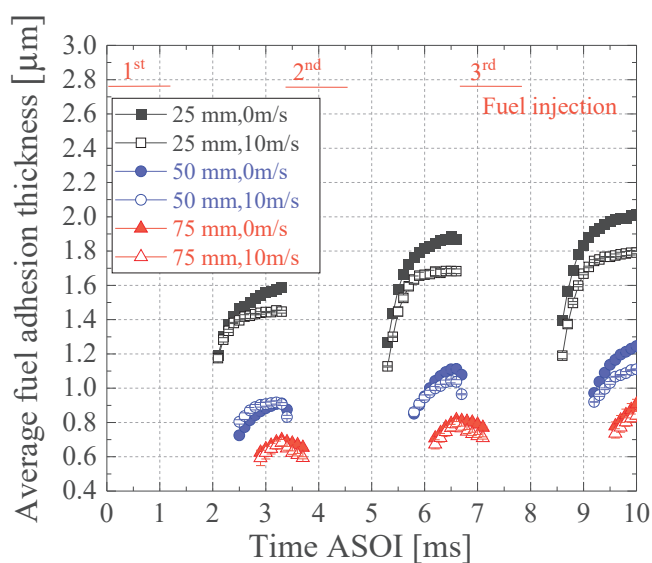
Figure 6.9 Development of fuel adhesion thickness at early stage.

Figure 6.10 depicts the variation of fuel adhesion mass and the ratio of fuel adhesion mass (fuel adhesion mass/total injection mass) with time at different impingement distances. The left vertical axis represents the fuel adhesion mass, and the right vertical axis represents the ratio of fuel adhesion mass. The fuel adhesion mass increases initially. After the injection is completed, there are a large number of fuel droplets in the air, which then adhere to the impingement wall.
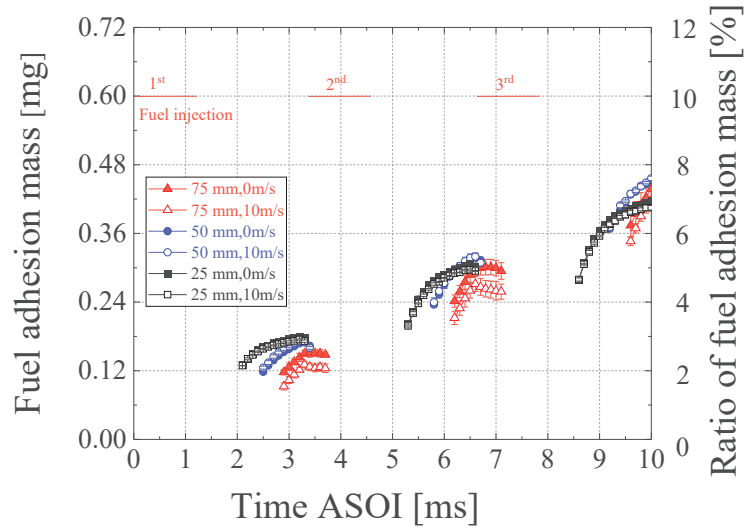
Figure 6.10 Development of fuel adhesion mass at early stage.

6.4.3 Later stage analyses
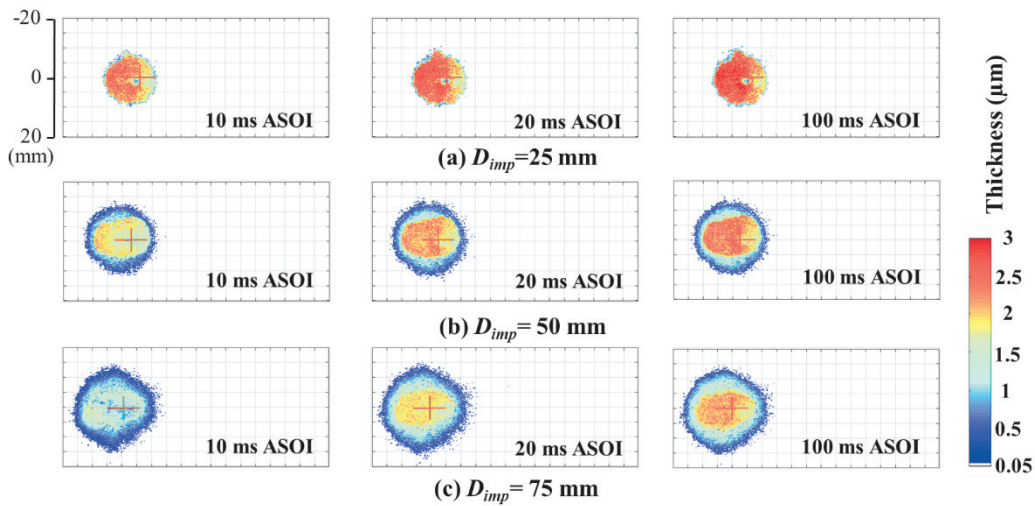
Figure 6.11 Development of fuel adhesion for different impingement distance at later stage (Static flow field).

Figures 6.11 and 6.12 respectively represent the development of fuel adhesion for different impingement distances at later stage. From Figures 6.11 and 6.12 in the later stage of fuel adhesion, as the impingement distance increases, the thicker area becomes thinner, and the thinner area becomes larger and larger. As the impingement distance increases, the early-stage fuel adhesion area enlarges. Under cross-flow

conditions, fuel adhesion moves downstream. Cross-flow promotes an increase in the area of thinner fuel adhesion.
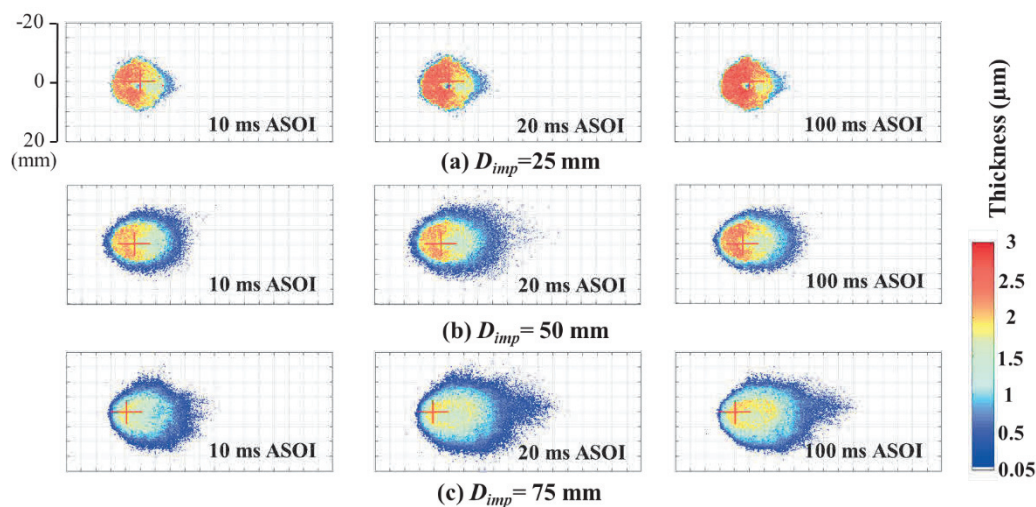
Figure 6.12 Development of fuel adhesion for different impingement distance at later stage (Cross-flow flow field).

Figure 6.13 shows the change of fuel adhesion area with time in the later stage. In the later stages, the fuel adhesion area under cross-flow conditions increased significantly. Due to the prolonged influence of cross-flow post-spraying, the degree of spray diffusion increases, intensifying the effect of cross-flow. Consequently, fuel adhesion area increases. The fuel adhesion area rose with the impingement distance. Because the impingement distance rose, the droplets had more time and space to disperse and spread before adhering to the wall, thus increasing the fuel adhesion area. As the impingement distance increases, the rate of decrease in fuel adhesion area becomes more pronounced at the later stage under cross-flow conditions. because the thinner fuel adhesion area is bigger at higher impingement distances, leading to a shorter evaporation time at longer impingement distances, the rate of decrease in fuel adhesion area becomes more pronounced.
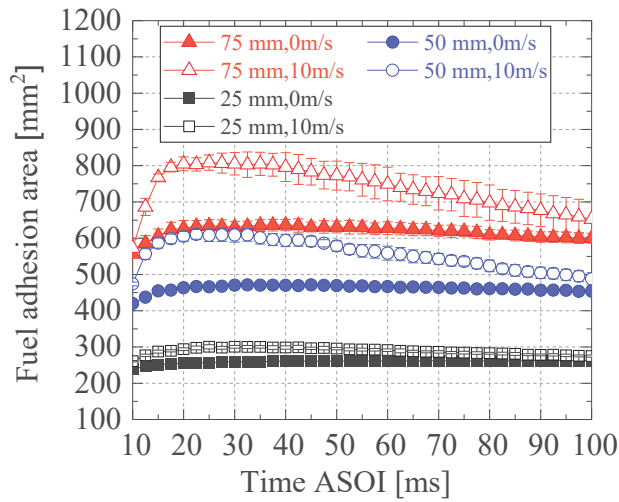
Figure 6.13 Development of fuel adhesion area at later stage.

Figure 6.14 depicts the variation of average fuel adhesion thickness over time at different impingement distances. Fuel adhesion thickness decreases with the increase in impingement distance. Because the fuel droplets leaving the nozzle have high initial velocity and kinetic energy. As the impingement distance increases, the speed of the fuel droplets gradually decreases, and the kinetic energy during attachment decreases, which in turn causes the fuel adhesion droplets to be more dispersed, resulting in a thinner fuel adhesion thickness. The average fuel adhesion thickness increases over time because, under the influence of cross-flow, thinner regions evaporate over time. Meanwhile, thicker regions persist, resulting in an overall increase in average fuel adhesion thickness over time.

126
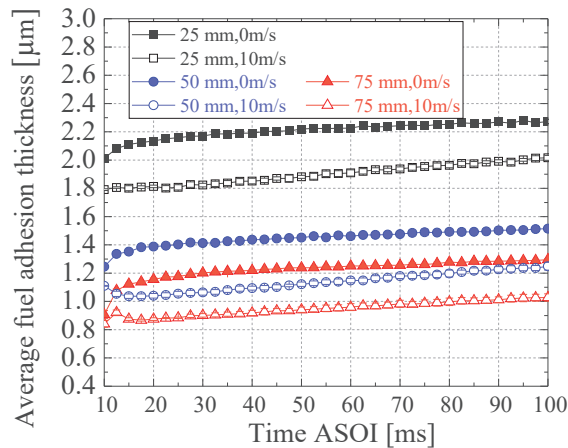
Figure 6.14 Development of fuel adhesion thickness at later stage.

Figure 6.15 illustrates the fluctuation in the fuel adhesion mass and adhesion mass ratio with time during the late stage. Fuel adhesion mass and mass ratio are represented by the left and right vertical axes, respectively. As time goes by, when the impingement distance (50mm-75mm) is larger, the fuel adhesion mass decreases, because cross-flow is conducive to the evaporation of thinner fuel adhesion, whereas when the impingement distance (25mm) is small, the fuel adhesion mass basically unchanged, because the fuel adhesion thickness is larger, and cross-flow has less impact on the evaporation of thicker fuel adhesion. The fuel adhesion mass increases with the impingement distance, as larger impingement distances result in more fuel droplets coming into adhere with the impingement wall surface. This leads to the formation of a more extensive but thinner adhesion layer on the impingement wall surface, thereby increasing the fuel adhesion mass.
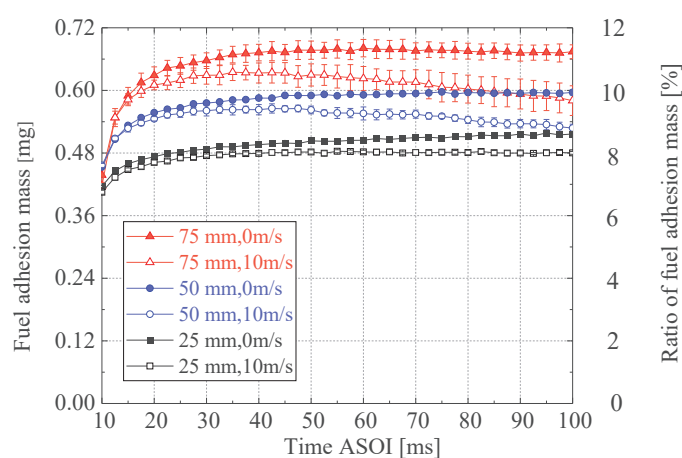
Figure 6.15 Development of fuel adhesion mass at later stage.

6.4.4   *Spreading of fuel adhesion*
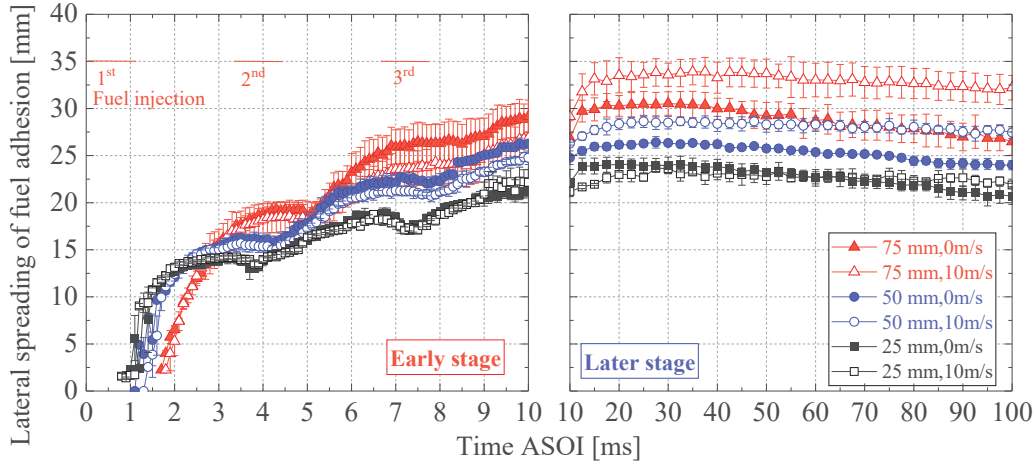
Figure 6.16 Lateral spreading of fuel adhesion.
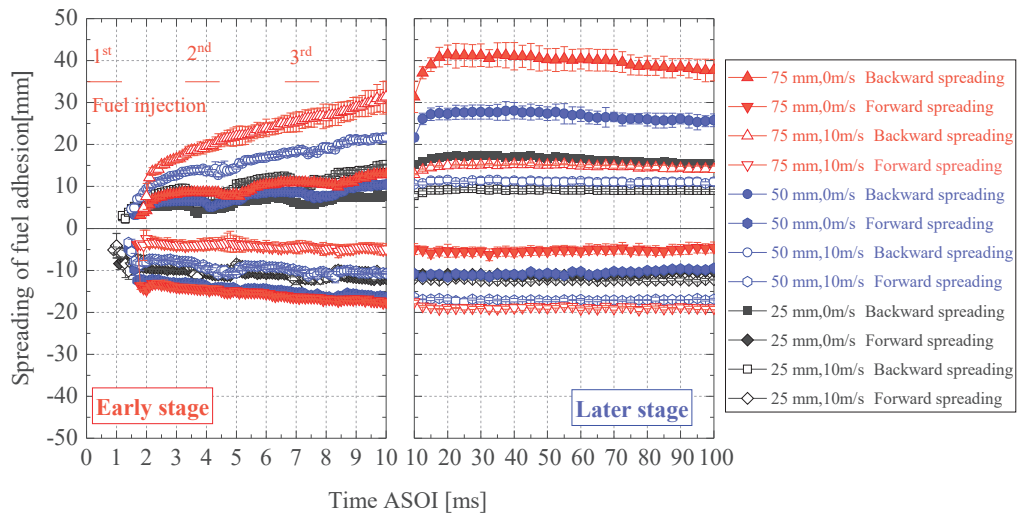
Figure 6.17 Spreading of fuel adhesion.

Figures 6.16 and 6.17 respectively display the changes in lateral spreading and spreading of fuel adhesion over time. Under cross-flow conditions the backward spreading of fuel adhesion increases while the forward spreading of fuel adhesion decreases. The cross-flow causes the spray to move laterally as a whole, resulting in the overall lateral movement of spray distribution, thereby increasing the backward spreading while decreasing the forward spreading in the upstream area. As the

128

impingement distance increases, the backward spreading increases. However, under cross-flow conditions, the forward spreading decreases, while under no cross-flow conditions, the forward spreading increases. The increased impingement distance leads to a decrease in the force of the spray droplets, allowing them to penetrate deeper into the downstream area, thus increasing the backward spreading. The lateral spreading of fuel adhesion increases with the increase in impingement distance. Because a larger impingement distance can induce stronger aerodynamic effects, such as vortices and turbulence. These effects influence the motion and shape of the spray, resulting in larger lateral spreading of fuel adhesion.

6.4.5 *Fuel adhesion distribution*

Figures 6.18 (a), (b), (c), and (d) illustrate the relationship between fuel adhesion thickness and mass at two different time points (20 ms and 100 ms ASOI) under cross-flow conditions of 0 m/s and 10 m/s. These figures reveal two peaks: a smaller peak (representing thinner regions) and a larger peak (representing thicker regions). When the wall impingement distance is higher, the smaller peak becomes more pronounced, indicating an increase in the thinner regions, while the larger peak decreases, indicating a reduction in the thicker regions. This observation is consistent with Figures 6.11 and 6.12 Over time, both peaks shift towards thicker regions, signifying that the fuel adhesion mass increases with the fuel adhesion thickness. This is because residual spray droplets in the air gradually settle and adhere to the wall over time, leading to an increase in fuel adhesion thickness and causing both peaks to shift towards the thicker regions. Under cross-flow conditions, the larger peak (thicker regions) is reduced, and the smaller peak (thinner regions) is increased. This occurs because the cross-flow imparts lateral kinetic energy to the spray droplets, causing them to deviate from their original trajectories, increasing dispersion, and reducing droplets aggregation, thereby resulting in a more uniform distribution. Additionally, the cross-flow increases the relative velocity of the droplets, enhancing aerodynamic and evaporation effects, which causes the droplets to become smaller and lighter.

These smaller droplets are more easily dispersed, leading to a more uniform fuel adhesion distribution.
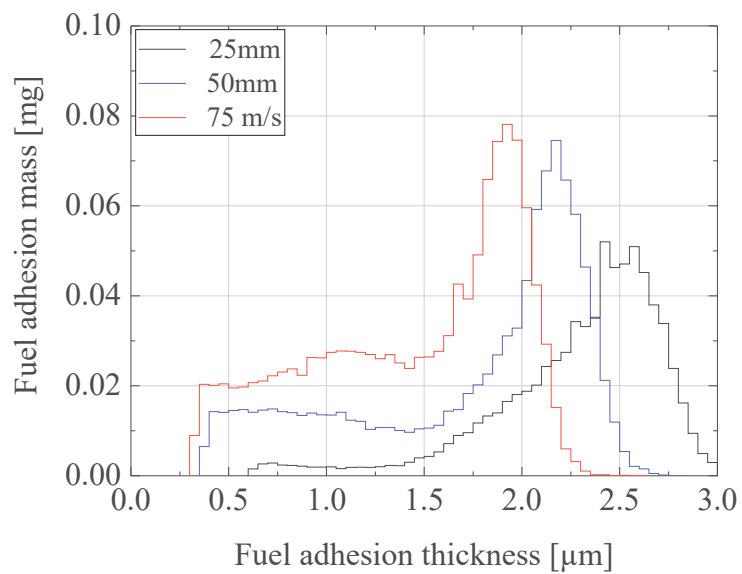
(a) $U_x = 0$ m/s; T = 20 ms ASOI
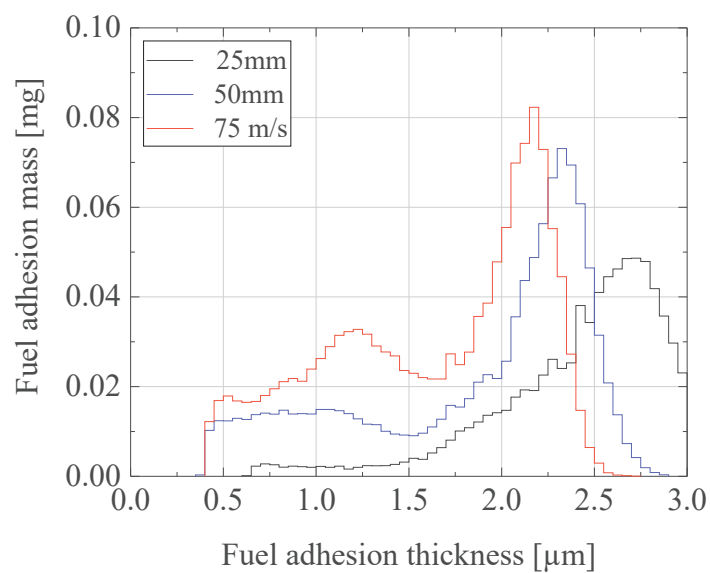
(b) $U_x = 0$ m/s; T = 100 ms ASOI
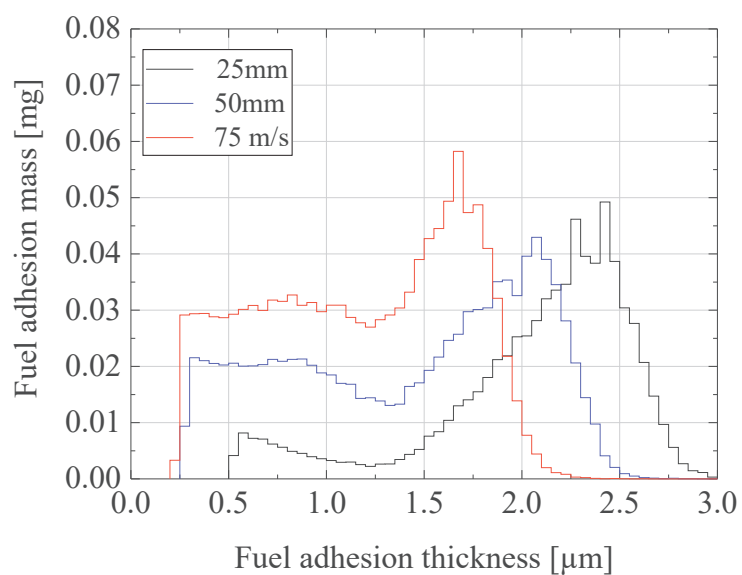
(c) U_x = 10 m/s; T = 20 ms ASOI
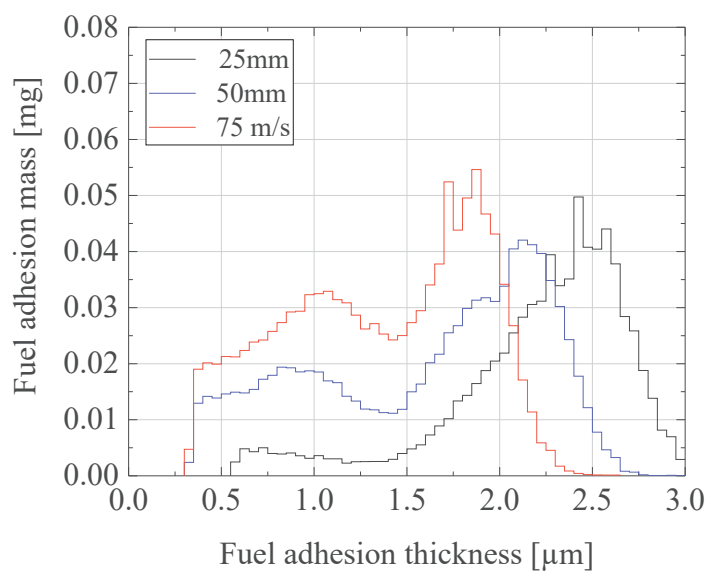
(d) U_x = 10 m/s; T = 100 ms ASOI
Figure 6.18 Connection between the thickness and mass of fuel adhesion.

6.4.6 *Mechanism of fuel adhesion formation*

Figure 6.19 (a), and (b) illustrates different mechanisms of fuel adhesion development at early and later stages. The purple line graph represents the spray profile when the

first injection starts to adhere to the plate, and the blue line graph represents the spray profile before the second injection begins. The fuel adhesion duration time is t. In the early stage of fuel adhesion, the bigger the impingement distance, the shorter the fuel adhesion duration and low impinging velocity, and the smaller the fuel adhesion mass. In the later stage of fuel adhesion, when the impingement distance increases, the droplet velocity decreases and the droplet splash velocity decreases, at the same time, droplets move with entrainment, resulting in thinner fuel adhesion.
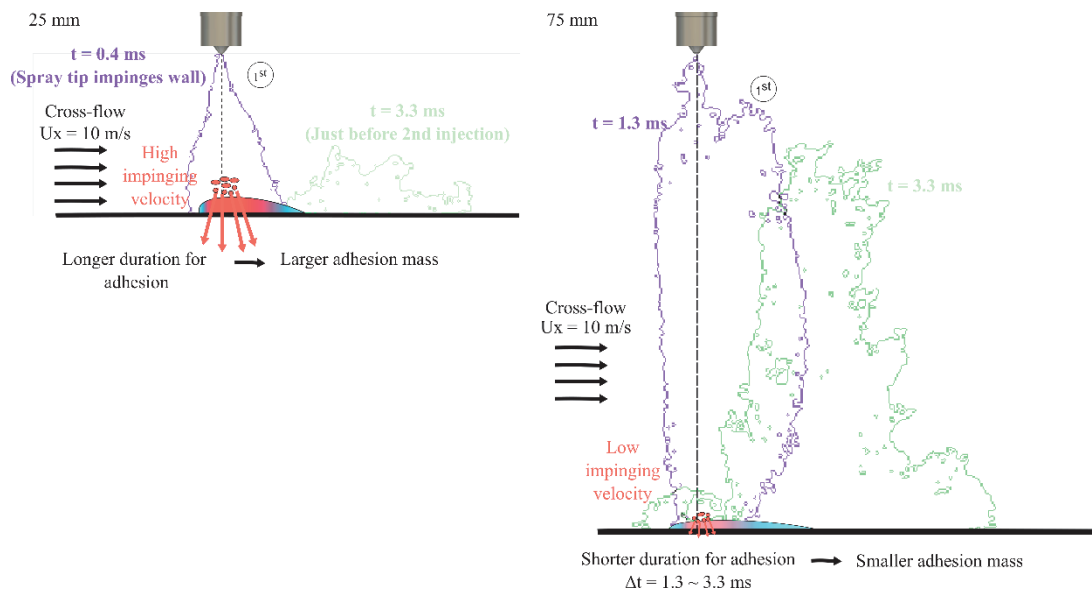
(a) Δt = wall impingement to 3.3 ms (Just before 2nd injection)
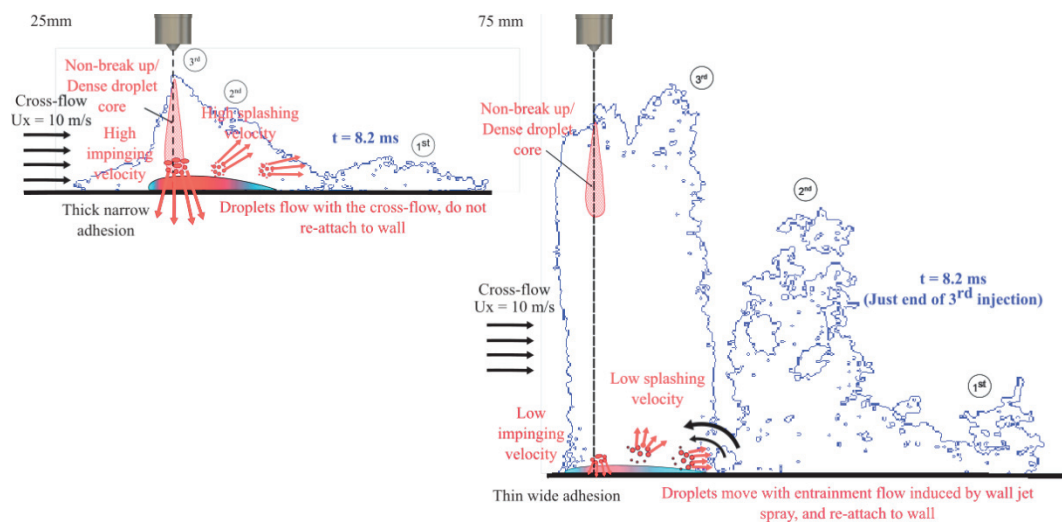
(b) t = 8.2 ms at end of 3rd injection.
Figure 6.19 Mechanism of fuel adhesion formation.

6.5 Summary

This chapter utilizes HSV to observe spray structures on a vertical plane and employs the RIM method to investigate fuel adhesion phenomena. The research analyzes the different impingement distances on fuel adhesion area, thickness, and mass under cross-flow conditions. The detailed conclusions are as follows:

(1) As the impingement distance increases, the later the spray hits the impingement wall, the spray spreads more widely, and the horizontal penetration of the spray increases.

(2) The average fuel adhesion thickness decreases with the increase in impingement distance. In the later stage of fuel adhesion, as the impingement distance increases, the thicker area becomes thinner, and the thinner area becomes larger and larger.

(3) As the impingement distance increases, the fuel adhesion area increases, the rate of decrease in fuel adhesion area becomes more pronounced at the later stage under cross-flow conditions.

(4) The fuel adhesion mass increases with the impingement distance.

(5) Under cross-flow conditions the backward spreading of fuel adhesion increases while the forward spreading of fuel adhesion decreases. As the impingement distance increases, the backward spreading increases.

CHAPTER 7 CONCLUSIONS

This paper experimentally investigates the wall impingement spray phenomenon of a single hole gasoline injector under different dynamic conditions. Firstly, the study uses PIV technique to measure homogeneity under different cross-flow conditions. This can help understand the impact of cross-flow on fuel adhesion and spray dispersion, which is important for optimizing fuel injection system design. Then, continuous wave laser-Mie scattering technique and RIM method are employed to visualize the spray spread and fuel adhesion characteristics, analyzing in detail the fuel adhesion properties such as fuel mass, area, and thickness.

Firstly, the evolution rules of impact spray and fuel adhesion caused by different injection strategies (single injection, double injection, triple injection) were studied: investigations were conducted under cross-flow and static flow conditions to explore the evolution rules of impact spray and fuel adhesion caused by different injection strategies. This can help optimize injection strategies, improve fuel utilization, and reduce emissions. Next, the effects of different cross-flow velocities fields (0, 10, 20, 30 m/s) on split spray and fuel adhesion characteristics were studied: The effects of different cross-flow flow fields on split spray and fuel adhesion characteristics were studied. This helps to understand the effect of cross-flow on fuel spray behavior and thereby optimize the fuel injection system. Finally, the effects of different wall impingement distances (25, 50, 75 mm) on impact spray and fuel adhesion under cross-flow and static flow conditions were investigated. Additionally, under the same experimental conditions, the relationship between fuel adhesion and spray behavior is studied. This chapter summarizes the main conclusions of the research.

7.1 Main Findings of This Study

7.1.1 Fuel adhesion characteristics of split injection in cross-flow under baseline conditions

This chapter utilizes continuous wave laser-Mie scattering technology and the RIM method to investigate the dynamic behavior and fuel adhesion characteristics of wall-impinging sprays, with a focus on a 75 mm wall-impingement distance as the reference point. Observations under cross-flow conditions reveal several key findings:

The spray diffuses downstream without collision with previous segments, and the length of fuel adhesion on the impingement wall consistently remains shorter than the vertical spray length.

Vertical penetration of the spray increases linearly up to a 75 mm impingement distance, while horizontal penetration initially increases linearly and then stabilizes over time.

Fuel adhesion exhibits varying thickness, being thicker near the coordinate origin and thinner at the edges. The fuel adhesion area initially increases but later decreases. The average fuel adhesion thickness of each segment injection increases initially before decreasing in the early stage, and then gradually increases in the later stages. Similarly, fuel adhesion mass shows an initial increase followed by a decrease. These findings highlight the complex dynamics and characteristics of wall-impinging sprays under cross-flow conditions, providing valuable insights for related research and applications.

7.1.2 Various split injection strategy on fuel adhesion

This chapter investigates the effect of split injection on wall-impingement spray and the fuel adhesion characteristics under static flow and cross-flow field conditions:

In static-flow conditions, the second and third sprays collide with the residual spray

from previous injections before reaching the wall. However, under cross-flow conditions, the second and third sprays do not collide with the residual spray from the first and second injections before reaching the wall.

In static flow conditions, the fuel adhesion area initially increased and then stabilized, whereas in cross-flow conditions, it initially increased and then decreased dramatically due to enhanced diffusion and evaporation. Triple injection led to a reduction in fuel adhesion area in cross-flow conditions but resulted in the largest adhesion area in static flow conditions due to increased ductility of fuel adhesion.

In static flow conditions, the fuel adhesion mass stabilized over time, while in cross-flow conditions, it gradually decreased due to increased evaporation. Triple injection resulted in the smallest fuel adhesion mass in cross-flow conditions, attributed to decreased injection mass and enhanced atomization.

The average fuel adhesion thickness was significantly smaller in cross-flow conditions compared to static flow conditions, attributed to enhanced evaporation. Triple injection yielded the smallest average fuel adhesion thickness under both static and cross-flow conditions.

Under static flow conditions, the distribution of fuel adhesion thickness was concentrated near a thicker peak, whereas in cross-flow conditions, it shifted towards a thinner peak. Peak values of split injection decreased over time under cross-flow conditions.

These findings underscore the influence of injection strategy and flow conditions on fuel adhesion characteristics, with implications for optimizing spray performance in real-world applications. Split injection improves mixture formation, ensures a more uniform mixing of fuel and air, helps complete combustion. Fuel is burned more fully, which can increase the engine's power output and enhance the vehicle's power performance.

7.1.3 Various cross-flow velocity on fuel adhesion

This chapter examined spray distribution and fuel adhesion under various cross-flow velocities, yielding the following findings:

Under cross-flow conditions, the horizontal penetration of split injection spray drops sharply because the previous spray disappears under the action of cross-flow. With the increase of cross-flow velocity, the faster the spray moves downstream, and the larger the spray area, the spray horizontal penetration increases, but the time for the spray to hit the wall is basically the same.

Initially, the rate of increase in fuel adhesion area accelerated with rising cross-flow velocity. However, in later stages, the rate of decrease in fuel adhesion area exhibited an initial increase with increasing cross-flow velocity. Upon surpassing a critical velocity threshold (20 m/s), the rate of decrease in fuel adhesion area tended to stabilize, suggesting a threshold effect influenced by cross-flow velocity.

Increasing cross-flow velocities led to a consistent decrease in fuel adhesion thickness throughout the adhesion process. Elevated cross-flow velocities intensified airflow, promoting turbulence and eddy formation. This dispersion effect fragmented spray droplets into smaller sizes, diminishing the probability of adhesion to the wall.

In later stages, the rate of reduction in fuel adhesion mass escalated with higher cross-flow velocities. Stronger cross-flow forces facilitated downstream movement of droplets, reducing their chances of impingement on the wall. Consequently, this contributed to an accelerated decrease in fuel adhesion mass.

At high cross-flow velocity, the fuel adhesion thickness decreases, reducing fuel residue, decreasing carbon deposits on engine components, and lowering the risk of engine wear. The reduction in fuel adhesion means that more fuel is fully combusted, improving fuel efficiency and enhancing fuel economy. Cross-flow helps reduce fuel adhesion, promoting more complete combustion and lowering unburned hydrocarbon emissions. By designing more optimized airflow, fuel adhesion characteristics can be

better controlled, thereby enhancing overall performance. These findings underscore the complex interplay between cross-flow velocity and fuel adhesion dynamics, highlighting the importance of optimizing engine parameters to minimize fuel adhesion and enhance engine performance.

7.1.4　Various impingement distance on fuel adhesion

The chapter analyzes the effects of different impingement distances on wall-impingement spray, fuel adhesion area, thickness, and mass under cross-flow conditions, yielding the following detailed conclusions:

As the impingement distance increases, the later the spray hits the impingement wall, the spray spreads more widely, and the horizontal penetration of the spray increases.

The average fuel adhesion thickness decreases as the impingement distance increases. In the later stages of fuel adhesion, with increasing impingement distance, thicker areas become thinner, while thinner areas become larger. With increasing impingement distance, the fuel adhesion area increases. The rate of decrease in fuel adhesion area becomes more pronounced in the later stages under cross-flow conditions as the impingement distance increases. The fuel adhesion mass increases with the impingement distance. As the impingement distance increases, the backward spreading of fuel adhesion further intensifies.

These findings highlight the intricate relationship between impingement distance and fuel adhesion characteristics under cross-flow conditions. Different impingement distances significantly impact fuel adhesion characteristics. By optimizing the impingement distance, the quality, thickness, and area of fuel adhesion can be effectively controlled, enhancing combustion efficiency, reducing emissions and carbon deposits, and optimizing engine performance. These research findings provide valuable references for the design and optimization of internal combustion engine fuel injection systems.

7.2 Recommendations for Future Works

Most of the adhered fuel should be in the boundary layer, based on the measured fuel adhesion characteristics in this study. Therefore, the interaction between the boundary layer and the spray impingement is critical. To better understand the fuel adhesion mechanism under cross-flow field conditions, including the evolution of fuel adhesion structure, the PIA technique will be employed to measure detailed microscopic droplet behaviors above the flat-wall in the future. Additionally, the impact of comparing the effects of using a quartz glass plate versus a metal plate on fuel adhesion will be analyzed. The PIV technique will be employed to observe the interaction between fuel injection and ambient gas flow. Furthermore, the effects of wall heating and wall inclination angle change within the cross-flow on fuel thickness and fuel adhesion area will also be analyzed.

REFERENCES

[1]   U. NATIONS, " United Nations Framework Convention on Climate Change (UNFCCC),"
1992, vol. FCCC/INFORMAL/84 [Online]. Available:
https://unfccc.int/resource/docs/convkp/conveng.pdf viewed on May 10, 2024. [Online].
Available: https://unfccc.int/resource/docs/convkp/conveng.pdf viewed on May 10, 2024.

[2]   T. Jayaraman, "The Paris agreement on climate change: Background, analysis, and
implications," *Review of Agrarian Studies,* vol. 5, no. 2, 2015.

[3]   T. Kanitkar, "What Should the Climate Goal Be, 1.5°C or 2°C?," *Review of Agrarian
Studies,* vol. 5, 2, 2015. [Online]. Available:
https://ras.org.in/what_should_the_climate_goal_be viewed on May 10, 2024.

[4]   (2015). *Intergovernmental Panel on Climate Change (IPCC). Summary for Policymakers.
In: Climate Change 2021.* [Online] Available: https://www.ipcc.ch/report/ar6/wg1/
viewed on May 10, 2024.

[5]   (2013). *Intergovernmental Panel on Climate Change (IPCC) (2013), Climate Change 2013:
The Physical Science Basis.* [Online] Available:
https://www.ipcc.ch/site/assets/uploads/2017/09/WG1AR5_Frontmatter_FINAL.pdf
viewed on May 10, 2024.

[6]   P. b. t. President, "UNFCCC. Adoption of the Paris Agreement.," in *Conference of the
Parties*
Twenty-first session
Paris, 2015, vol. FCCC/CP/2015/L.9/Rev.1. [Online]. Available:
http://unfccc.int/resource/docs/2015/cop21/eng/l09r01.pdf viewed on May 10, 2024.
[Online]. Available: http://unfccc.int/resource/docs/2015/cop21/eng/l09r01.pdf viewed
on May 10, 2024.

[7]   (2015). *Net Zero by 2050 A Roadmap for the*
Global Energy Sector. [Online] Available: https://iea.blob.core.windows.net/assets/063ae08a-
7114-4b58-a34e-39db2112d0a2/NetZeroby2050-
ARoadmapfortheGlobalEnergySector.pdf viewed on May 10, 2024.

[8]   W. Wang and J. Wang, "Determinants investigation and peak prediction of CO2
emissions in China's transport sector utilizing bio-inspired extreme learning machine,"
Environmental Science and Pollution Research, vol. 28, no. 39, pp. 55535-55553, 2021.

[9]   M. S. Sardar, N. Asghar, and H. U. Rehman, "Moderation of competitiveness in
determining environmental sustainability: economic growth and transport sector carbon
emissions in global perspective," *Environment, Development and Sustainability,* vol. 26,
no. 1, pp. 1481-1503, 2024.

[10]   M. Robaina and A. Neves, "Complete decomposition analysis of CO2 emissions intensity
in the transport sector in Europe," *Research in Transportation Economics,* vol. 90, p.
101074, 2021.

[11]   C. Zhao, K. Wang, X. Dong, and K. Dong, "Is smart transportation associated with
reduced carbon emissions? The case of China," *Energy Economics,* vol. 105, p. 105715,
2022.

[12]   T. S. Zueva, A. B. Garyaev, and L. Weiss, "Model of fuel spray propagation in direct

injecting internal combustion engines under cross-flow conditions," 2020, vol. 1565: IOP Publishing, 1 ed., p. 012054.

[13] J. Rubin and C. Kling, "An emission saved is an emission earned: an empirical study of emission banking for light-duty vehicle manufacturers," *Journal of Environmental Economics and Management,* vol. 25, no. 3, pp. 257-274, 1993.

[14] F. Leach, G. Kalghatgi, R. Stone, and P. Miles, "The scope for improving the efficiency and environmental impact of internal combustion engines," *Transportation Engineering,* vol. 1, p. 100005, 2020.

[15] R. Zhu *et al.*, "Tailpipe emissions from gasoline direct injection (GDI) and port fuel injection (PFI) vehicles at both low and high ambient temperatures," *Environmental Pollution,* vol. 216, pp. 223-234, 2016.

[16] F. Zhao, M. C. Lai, and D. L. Harrington, "Automotive spark-ignited direct-injection gasoline engines," *Progress in energy and combustion science,* vol. 25, no. 5, pp. 437-562, 1999.

[17] A. Bengo, "Dujos automobiliams – varikliai, draugaujantys su dujomis. Į ką atkreipti dėmesį?," ed, 2022.

[18] W. Zhang *et al.*, "Impact of injector tip deposits on gasoline direct injection engine combustion, fuel economy and emissions," *Applied energy,* vol. 262, p. 114538, 2020.

[19] T. Kim, J. Song, and S. Park, "Effects of turbulence enhancement on combustion process using a double injection strategy in direct-injection spark-ignition (DISI) gasoline engines," *International Journal of Heat and Fluid Flow,* vol. 56, pp. 124-136, 2015.

[20] A. Montanaro, S. Malaguti, and S. Alfuso, "Wall impingement process of a multi-hole GDI spray: experimental and numerical investigation," SAE Technical Paper, 0148-7191, 2012.

[21] Y. Qian, Z. Li, L. Yu, X. Wang, and X. Lu, "Review of the state-of-the-art of particulate matter emissions from modern gasoline fueled engines," *Applied Energy,* vol. 238, pp. 1269-1298, 2019.

[22] M. C. Drake, T. D. Fansler, A. S. Solomon, and G. A. Szekely Jr, "Piston fuel films as a source of smoke and hydrocarbon emissions from a wall-controlled spark-ignited direct-injection engine," *SAE transactions,* pp. 762-783, 2003.

[23] Z. Lee and S. Park, "Particulate and gaseous emissions from a direct-injection spark ignition engine fueled with bioethanol and gasoline blends at ultra-high injection pressure," *Renewable Energy,* vol. 149, pp. 80-90, 2020.

[24] J. Etheridge, S. Mosbach, M. Kraft, H. Wu, and N. Collings, "Modelling soot formation in a DISI engine," *Proceedings of the Combustion Institute,* vol. 33, no. 2, pp. 3159-3167, 2011.

[25] Q. Jiao and R. D. Reitz, "The effect of operating parameters on soot emissions in GDI engines," *SAE International Journal of Engines,* vol. 8, no. 3, pp. 1322-1333, 2015.

[26] T. D. Fansler, M. F. Trujillo, and E. W. Curtis, "Spray-wall interactions in direct-injection engines: An introductory overview," *International Journal of Engine Research,* vol. 21, no. 2, pp. 241-247, 2020.

[27] S. Henkel, F. Beyrau, Y. Hardalupas, and A. Taylor, "Novel method for the measurement of liquid film thickness during fuel spray impingement on surfaces," *Optics express,* vol. 24, no. 3, pp. 2542-2561, 2016.

[28]   J. Demuynck, C. Favre, D. Bosteels, H. Hamje, and J. Andersson, "Real-world emissions measurements of a gasoline direct injection vehicle without and with a gasoline particulate filter," SAE Technical Paper, 0148-7191, 2017.

[29]   M. Salvia *et al.*, "Will climate mitigation ambitions lead to carbon neutrality? An analysis of the local-level plans of 327 cities in the EU," *Renewable and Sustainable Energy Reviews,* vol. 135, p. 110253, 2021.

[30]   S. P. Chincholkar and J. G. Suryawanshi, "Gasoline direct injection: an efficient technology," *Energy Procedia,* vol. 90, pp. 666-672, 2016.

[31]   W. Salber, P. Wolters, T. Esch, J. Geiger, and J. Dilthey, "Synergies of variable valve actuation and direct injection," *SAE Transactions,* pp. 1213-1221, 2002.

[32]   A. C. Alkidas, "Combustion advancements in gasoline engines," *Energy Conversion and Management,* vol. 48, no. 11, pp. 2751-2761, 2007.

[33]   C. Preussner, C. Döring, S. Fehler, and S. Kampmann, "GDI: Interaction between mixture preparation, combustion system and injector performance," SAE Technical Paper, 0148-7191, 1998.

[34]   S. Itabashi, E. Murase, H. Tanaka, M. Yamaguchi, and T. Muraguchi, "New combustion and powertrain control technologies for fun-to-drive dynamic performance and better fuel economy," SAE Technical Paper, 0148-7191, 2017.

[35]   C. Schwarz, E. Schünemann, B. Durst, J. Fischer, and A. Witt, "Potentials of the spray-guided BMW DI combustion system," SAE Technical Paper, 0148-7191, 2006.

[36]   C. Park, S. Kim, H. Kim, and Y. Moriyoshi, "Stratified lean combustion characteristics of a spray-guided combustion system in a gasoline direct injection engine," *Energy,* vol. 41, no. 1, pp. 401-407, 2012.

[37]   P. K. Wu and G. M. Faeth, "Onset and end of drop formation along the surface of turbulent liquid jets in still gases," *Physics of Fluids,* vol. 7, no. 11, pp. 2915-2917, 1995.

[38]   S. M. Arai M, Hiroyasu H., "Similarity between the breakup lengths of a high speed liquid jet in atmospheric and pressurized conditions.," *NIST Special Publication,* vol. 813, 563-570, 1991.

[39]   C. Soteriou, R. Andrews, and M. Smith, "Direct injection diesel sprays and the effect of cavitation and hydraulic flip on atomization," *SAE transactions,* pp. 128-153, 1995.

[40]   N. Tamaki, M. Shimizu, and H. Hiroyasu, "Enhancement of the atomization of a liquid jet by cavitation in a nozzle hole," *Atomization and Sprays,* vol. 11, no. 2, 2001.

[41]   C. Baumgarten, *Mixture formation in internal combustion engines*. Springer Science & Business Media, 2006.

[42]   R. Rioboo, C. Tropea, and M. Marengo, "Outcomes from a drop impact on solid surfaces," *Atomization and sprays,* vol. 11, no. 2, 2001.

[43]   Y. Liu, X. Yan, and Z. Wang, "Droplet dynamics on slippery surfaces: small droplet, big impact," *Biosurface and Biotribology,* vol. 5, no. 2, pp. 35-45, 2019.

[44]   H. Fujimoto, M. Saito, A. Minoura, N. Katsura, I. Y. Cho, and J. Senda, "Characteristics of a diesel spray impinging on a flat wall," 1988, vol. 88, p. 439.

[45]   N. Katsura, M. Saito, J. Senda, and H. Fujimoto, "Characteristics of a diesel spray impinging on a flat wall," *SAE Transactions,* pp. 252-268, 1989.

[46]   L. Zhao *et al.*, "An experimental and numerical study of diesel spray impingement on a flat plate," *SAE International Journal of Fuels and Lubricants,* vol. 10, no. 2, pp. 407-422,

2017.

[47]   X. He *et al.*, "Characteristics of spray and wall wetting under flash-boiling and non-flashing conditions at varying ambient pressures," *Fuel,* vol. 264, p. 116683, 2020.

[48]   H. Luo, K. Nishida, S. Uchitomi, Y. Ogata, W. Zhang, and T. Fujikawa, "Effect of spray impingement distance on piston top fuel adhesion in direct injection gasoline engines," *International Journal of Engine Research,* vol. 21, no. 5, pp. 742-754, 2020.

[49]   H. Luo, K. Nishida, S. Uchitomi, Y. Ogata, W. Zhang, and T. Fujikawa, "Effect of temperature on fuel adhesion under spray-wall impingement condition," *Fuel,* vol. 234, pp. 56-65, 2018.

[50]   H. Luo, K. Nishida, and Y. Ogata, "Fuel adhesion characteristics under non-evaporation and evaporation conditions: Part 2–Effect of ambient pressure," *Fuel,* vol. 251, pp. 98-105, 2019.

[51]   H. Luo, K. Nishida, Y. Ogata, W. Zhang, and T. Fujikawa, "Fuel adhesion characteristics under non-evaporation and evaporation conditions: Part 1-effect of injection pressure," *Fuel,* vol. 240, pp. 317-325, 2019.

[52]   H. Luo, S. Uchitomi, K. Nishida, Y. Ogata, W. Zhang, and T. Fujikawa, "Experimental investigation on fuel film formation by spray impingement on flat walls with different surface roughness," *Atomization and Sprays,* vol. 27, no. 7, 2017.

[53]   M. Z. Akop, Y. Zama, T. Furuhata, and M. Arai, "Characteristics of adhesion of diesel fuel on impingement disk wall. Part 1: effect of impingement area and inclination angle of disk," *Atomization and Sprays,* vol. 23, no. 8, 2013.

[54]   C. P. Koci *et al.*, "Multiple-event fuel injection investigations in a highly-dilute diesel low temperature combustion regime," *SAE International Journal of Engines,* vol. 2, no. 1, pp. 837-857, 2009.

[55]   S. Busch, K. Zha, and P. C. Miles, "Investigations of closely coupled pilot and main injections as a means to reduce combustion noise in a small-bore direct injection Diesel engine," *International Journal of Engine Research,* vol. 16, no. 1, pp. 13-22, 2015.

[56]   Z. Zhang, F. Zhao, J. Deng, L.-g. Li, and Y. Shen, "Characteristics of the multiple injection diesel spray employed common rail system," *Journal of Thermal science and technology,* vol. 8, no. 1, pp. 106-119, 2013.

[57]   T. Li, K. Nishida, Y. Zhang, M. Yamakawa, and H. Hiroyasu, "An insight into effect of split injection on mixture formation and combustion of DI gasoline engines," SAE Technical Paper, 0148-7191, 2004.

[58]   T. Li, K. Nishida, Y. Zhang, T. Onoe, and H. Hiroyau, "Enhancement of stratified charge for DISI engines through split injection (Effect and its mechanism)," *JSME International Journal Series B Fluids and Thermal Engineering,* vol. 48, no. 4, pp. 687-694, 2005.

[59]   Z. Wang, C. Jiang, H. Xu, T. Badawy, B. Wang, and Y. Jiang, "The influence of flash boiling conditions on spray characteristics with closely coupled split injection strategy," *Applied energy,* vol. 187, pp. 523-533, 2017.

[60]   Z. Wang, Y. Li, H. Guo, C. Wang, and H. Xu, "Microscopic and macroscopic characterization of spray impingement under flash boiling conditions with the application of split injection strategy," *Fuel,* vol. 212, pp. 315-325, 2018.

[61]   K. Yang, H. Yamakawa, K. Nishida, Y. Ogata, and Y. Nishioka, "Effect of split injection on mixture formation and combustion processes of diesel spray injected into two-

dimensional piston cavity," *Proceedings of the Institution of Mechanical Engineers, Part D: Journal of Automobile Engineering,* vol. 232, no. 8, pp. 1121-1136, 2018.

[62] F. Chang, H. Luo, Y. Hagino, T. Tashima, K. Nishida, and Y. Ogata, "Effect of split injection on fuel adhesion characteristics under non-evaporation and evaporation conditions," *Fuel,* vol. 317, p. 123465, 2022.

[63] D. A. Nehmer and R. D. Reitz, "Measurement of the effect of injection rate and split injections on diesel engine soot and NOx emissions," *SAE transactions,* pp. 1030-1041, 1994.

[64] Z. Han, A. Uludogan, G. J. Hampson, and R. D. Reitz, "Mechanism of soot and NOx emission reduction using multiple-injection in a diesel engine," *SAE transactions,* pp. 837-852, 1996.

[65] S. H. Park, S. H. Yoon, and C. S. Lee, "Effects of multiple-injection strategies on overall spray behavior, combustion, and emissions reduction characteristics of biodiesel fuel," *Applied Energy,* vol. 88, no. 1, pp. 88-98, 2011.

[66] Y. Bo, H. Wu, P. Xiao, H. Li, Z. Shi, and X. Li, "Numerical study on the effect of multiple injection strategies on ignition processes for low-temperature diesel spray," *Fuel,* vol. 324, p. 124697, 2022.

[67] M. Costa, U. Sorge, S. Merola, A. Irimescu, M. La Villetta, and V. Rocco, "Split injection in a homogeneous stratified gasoline direct injection engine for high combustion efficiency and low pollutants emission," *Energy,* vol. 117, pp. 405-415, 2016.

[68] C. Park, S. Kim, H. Kim, S. Lee, C. Kim, and Y. Moriyoshi, "Effect of a split-injection strategy on the performance of stratified lean combustion for a gasoline direct-injection engine," *Proceedings of the Institution of Mechanical Engineers, Part D: Journal of Automobile Engineering,* vol. 225, no. 10, pp. 1415-1426, 2011.

[69] K. Yehliu, A. L. Boehman, and O. Armas, "Emissions from different alternative diesel fuels operating with single and split fuel injection," *Fuel,* vol. 89, no. 2, pp. 423-437, 2010.

[70] H. Oh, C. Bae, J. Park, and J. Jeon, "Effect of the multiple injection on stratified combustion characteristics in a spray-guided DISI engine," SAE Technical Paper, 0148-7191, 2011.

[71] T. C. Tow, D. A. Pierpont, and R. D. Reitz, "Reducing particulate and NO x emissions by using multiple injections in a heavy duty DI diesel engine," *SAE transactions,* pp. 1403-1417, 1994.

[72] H. G. How, H. H. Masjuki, M. A. Kalam, and Y. H. Teoh, "Influence of injection timing and split injection strategies on performance, emissions, and combustion characteristics of diesel engine fueled with biodiesel blended fuels," *Fuel,* vol. 213, pp. 106-114, 2018.

[73] S. H. R. Müller, S. Arndt, and A. Dreizler, "Analysis of the in-cylinder flow field/spray injection interaction within a DISI IC engine using high-speed PIV," SAE Technical Paper, 0148-7191, 2011.

[74] P. G. Aleiferis, A. Taylor, K. Ishii, and Y. Urata, "The nature of early flame development in a lean-burn stratified-charge spark-ignition engine," *Combustion and Flame,* vol. 136, no. 3, pp. 283-302, 2004.

[75] H. Chen, M. Xu, D. L. S. Hung, J. Yang, and H. Zhuang, "Development of a POD-based analysis approach for quantitative comparison of spray structure variations in a spark-ignition direct-injection engine," SAE Technical Paper, 0148-7191, 2013.

[76] P. Koch, M. G. Löffler, M. Wensing, and A. Leipertz, "Study of the mixture formation processes inside a modern direct-injection gasoline engine," *International Journal of Engine Research,* vol. 11, no. 6, pp. 455-471, 2010.

[77] D. L. S. Hung, H. Chen, M. Xu, J. Yang, and H. Zhuang, "Experimental investigation of the variations of early flame development in a spark-ignition direct-injection optical engine," *Journal of Engineering for Gas Turbines and Power,* vol. 136, no. 10, p. 101503, 2014.

[78] Z. Lee, D. Kim, and S. Park, "Effects of spray behavior and wall impingement on particulate matter emissions in a direct injection spark ignition engine equipped with a high pressure injection system," *Energy conversion and management,* vol. 213, p. 112865, 2020.

[79] B. Peterson and V. Sick, "Simultaneous flow field and fuel concentration imaging at 4.8 kHz in an operating engine," *Applied Physics B,* vol. 97, pp. 887-895, 2009.

[80] M. Braun, M. Klaas, and W. Schröder, "Influence of miller cycles on engine air flow," *SAE International Journal of Engines,* vol. 11, no. 2, pp. 161-178, 2018.

[81] K. Kawajiri, T. Yonezawa, H. Ohuchi, M. Sumida, and H. Katashiba, "Study of interaction between spray and air motion, and spray wall impingement," *SAE Transactions,* pp. 1356-1364, 2002.

[82] A. Ghasemi, R. M. Barron, and R. Balachandar, "Spray-induced air motion in single and twin ultra-high injection diesel sprays," *Fuel,* vol. 121, pp. 284-297, 2014.

[83] G. Wang, W. Yu, X. Li, Y. Su, R. Yang, and W. Wu, "Experimental and numerical study on the influence of intake swirl on fuel spray and in-cylinder combustion characteristics on large bore diesel engine," *Fuel,* vol. 237, pp. 209-221, 2019.

[84] K. Y. Kang and J. H. Baek, "Turbulence characteristics of tumble flow in a four-valve engine," *Experimental Thermal and Fluid Science,* vol. 18, no. 3, pp. 231-243, 1998.

[85] M. Mittal, D. L. S. Hung, G. Zhu, and H. Schock, "High-speed flow and combustion visualization to study the effects of charge motion control on fuel spray development and combustion inside a direct-injection spark-ignition engine," *SAE International Journal of Engines,* vol. 4, no. 1, pp. 1469-1480, 2011.

[86] P. G. Hill and D. Zhang, "The effects of swirl and tumble on combustion in spark-ignition engines," *Progress in energy and combustion science,* vol. 20, no. 5, pp. 373-429, 1994.

[87] D. Frieden and V. Sick, "Investigation of the fuel injection, mixing and combustion processes in an SIDI engine using quasi-3D LIF imaging," *SAE transactions,* pp. 270-281, 2003.

[88] C. Funk, V. Sick, D. L. Reuss, and W. J. A. Dahm, "Turbulence properties of high and low swirl in-cylinder flows," SAE Technical Paper, 0148-7191, 2002.

[89] T. D. Fansler, "Turbulence production and relaxation in bowl-in-piston engines," *SAE Transactions,* pp. 616-628, 1993.

[90] Y. Li, Y. Huang, S. Yang, K. Luo, R. Chen, and C. Tang, "A comprehensive experimental investigation on the PFI spray impingement: Effect of impingement geometry, cross-flow and wall temperature," *Applied Thermal Engineering,* vol. 159, p. 113848, 2019.

[91] M. R. O. Panão, A. L. N. Moreira, and D. F. G. Durão, "Effect of a cross-flow on spray impingement with port fuel injection systems for HCCI engines," *Fuel,* vol. 106, pp. 249-257, 2013.

[92]   G. Zhang, H. Luo, K. Kita, Y. Ogata, and K. Nishida, "Statistical variation analysis of fuel spray characteristics under cross-flow conditions," *Fuel,* vol. 307, p. 121887, 2022.

[93]   R. Welss, S. Bornschlegel, and M. Wensing, "Characterizing spray propagation of GDI injectors under crossflow conditions," SAE Technical Paper, 0148-7191, 2018.

[94]   D. Sedarsky *et al.*, "Model validation image data for breakup of a liquid jet in crossflow: part I," *Experiments in fluids,* vol. 49, pp. 391-408, 2010.

[95]   M. Braun, J. Palmer, T. van Overbrueggen, M. Klaas, R. Kneer, and W. Schroeder, "Influence of in-cylinder air flow on spray propagation," *SAE International Journal of Engines,* vol. 10, no. 4, pp. 1398-1410, 2017.

[96]   S. Moon, C. Bae, J. Choi, and E. Abo-Serie, "The influence of airflow on fuel spray characteristics from a slit injector," *Fuel,* vol. 86, no. 3, pp. 400-409, 2007.

[97]   M. Guo, N. Shimasaki, K. Nishida, Y. Ogata, and Y. Wada, "Experimental study on fuel spray characteristics under atmospheric and pressurized cross-flow conditions," *Fuel,* vol. 184, pp. 846-855, 2016.

[98]   M. Guo, K. Nishida, Y. Ogata, C. Wu, and Q. Fan, "Experimental study on fuel spray characteristics under atmospheric and pressurized cross-flow conditions, second report: Spray distortion, spray area, and spray volume," *Fuel,* vol. 206, pp. 401-408, 2017.

[99]   Z. Si, Y. Ashida, N. Shimasaki, K. Nishida, and Y. Ogata, "Effect of cross-flow on spray structure, droplet diameter and velocity of impinging spray," *Fuel,* vol. 234, pp. 592-603, 2018.

[100]   Z. Si *et al.*, "Experimental study on impingement spray and near-field spray characteristics under high-pressure cross-flow conditions," *Fuel,* vol. 218, pp. 12-22, 2018.

[101]   C. Arcoumanis, D. S. Whitelaw, and J. H. Whitelaw, "Gasoline injection against surfaces and films," *Atomization and Sprays,* vol. 7, no. 4, 1997.

[102]   G. Zhang, Z. Si, C. Zhai, H. Luo, Y. Ogata, and K. Nishida, "Characteristics of wall-jet vortex development during fuel spray impinging on flat-wall under cross-flow conditions," *Fuel,* vol. 317, p. 123507, 2022.

[103]   G. Zhang, P. Shi, H. Luo, Y. Ogata, and K. Nishida, "Investigation on fuel adhesion characteristics of wall-impingement spray under cross-flow conditions," *Fuel,* vol. 320, p. 123925, 2022.

[104]   Ö. L. Gülder, G. J. Smallwood, and D. R. Snelling, "Diesel spray structure investigation by laser diffraction and sheet illumination," *SAE transactions,* pp. 1046-1053, 1992.

[105]   D. L. Siebers, "Liquid-phase fuel penetration in diesel sprays," *SAE transactions,* pp. 1205-1227, 1998.

[106]   S. Padala, S. Kook, and E. R. Hawkes, "Effect of ethanol port-fuel-injector position on dual-fuel combustion in an automotive-size diesel engine," *Energy & fuels,* vol. 28, no. 1, pp. 340-348, 2014.

[107]   M. A. Linne, M. Paciaroni, E. Berrocal, and D. Sedarsky, "Ballistic imaging of liquid breakup processes in dense sprays," *Proceedings of the Combustion Institute,* vol. 32, no. 2, pp. 2147-2161, 2009.

[108]   M. Linne, M. Paciaroni, T. Hall, and T. Parker, "Ballistic imaging of the near field in a diesel spray," *Experiments in fluids,* vol. 40, pp. 836-846, 2006.

[109]   M. Pawlicki, H. A. Collins, R. G. Denning, and H. L. Anderson, "Two-photon absorption

and the design of two-photon dyes," *Angewandte Chemie International Edition,* vol. 48, no. 18, pp. 3244-3266, 2009.

[110]   E. Berrocal *et al.*, "Two-photon fluorescence laser sheet imaging for high contrast visualization of atomizing sprays," *OSA Continuum,* vol. 2, no. 3, pp. 983-993, 2019.

[111]   M. C. Drake and D. C. Haworth, "Advanced gasoline engine development using optical diagnostics and numerical modeling," *Proceedings of the Combustion Institute,* vol. 31, no. 1, pp. 99-124, 2007.

[112]   J. E. Parks, J. S. Armfield, T. E. Barber, J. M. E. Storey, and E. A. Wachter, "In situ measurement of fuel in the cylinder wall oil film of a combustion engine by LIF spectroscopy," *Applied spectroscopy,* vol. 52, no. 1, pp. 112-118, 1998.

[113]   R. Uchida, D. Tanaka, T. Noda, S. Okamoto, K. Ozawa, and T. Ishima, "Impingement behavior of fuel droplets on oil film," SAE Technical Paper, 0148-7191, 2015.

[114]   C. Wang *et al.*, "Laser induced fluorescence investigation on deposited fuel film from spray impingement on viscous film over a solid wall," *Energy,* vol. 231, p. 120893, 2021.

[115]   B. E. Schmidt and J. A. Sutton, "High-resolution velocimetry from tracer particle fields using a wavelet-based optical flow method," *Experiments in Fluids,* vol. 60, no. 3, p. 37, 2019.

[116]   B. E. Schmidt and J. A. Sutton, "Improvements in the accuracy of wavelet-based optical flow velocimetry (wOFV) using an efficient and physically based implementation of velocity regularization," *Experiments in Fluids,* vol. 61, pp. 1-17, 2020.

[117]   B. E. Schmidt, A. W. Skiba, S. D. Hammack, C. D. Carter, and J. A. Sutton, "High-resolution velocity measurements in turbulent premixed flames using wavelet-based optical flow velocimetry (wOFV)," *Proceedings of the combustion institute,* vol. 38, no. 1, pp. 1607-1615, 2021.

[118]   M. Raffel *et al.*, "Techniques for 3D-PIV," *Particle Image Velocimetry: A Practical Guide,* pp. 309-365, 2018.

[119]   P. Stansfield, G. Wigley, T. Justham, J. Catto, and G. Pitcher, "PIV analysis of in-cylinder flow structures over a range of realistic engine speeds," *Experiments in fluids,* vol. 43, pp. 135-146, 2007.

[120]   K. Tajima, D. Tsuru, S. Kawauchi, and H. Kato, "Spray model verification via observation of diesel spray propagation in parallel flow field to injection direction," *ILASS-Japan 2011,* pp. 194-198, 2011.

[121]   R. Klopfenstein Jr, "Air velocity and flow measurement using a Pitot tube," *ISA transactions,* vol. 37, no. 4, pp. 257-263, 1998.

[122]   G. E. Andrews, D. Bradley, and G. F. Hundy, "Hot wire anemometer calibration for measurements of small gas velocities," *International Journal of Heat and Mass Transfer,* vol. 15, no. 10, pp. 1765-1786, 1972.

[123]   J. C. Bhatia, F. Durst, and J. Jovanovic, "Corrections of hot-wire anemometer measurements near walls," *Journal of Fluid Mechanics,* vol. 122, pp. 411-431, 1982.

[124]   F. Motallebi, "A review of the hot-wire technique in 2-D compressible flows," *Progress in aerospace sciences,* vol. 30, no. 3, pp. 267-294, 1994.

[125]   L. Sileghem *et al.*, "Laminar burning velocity of gasoline and the gasoline surrogate components iso-octane, n-heptane and toluene," *Fuel,* vol. 112, pp. 355-365, 2013.

[126]   W. J. Pitz *et al.*, "Development of an experimental database and chemical kinetic models

for surrogate gasoline fuels," *SAE Transactions,* pp. 195-216, 2007.

[127] X. He *et al.,* "Impact of coolant temperature on piston wall-wetting and smoke generation in a stratified-charge DISI engine operated on E30 fuel," *Proceedings of the Combustion Institute,* vol. 37, no. 4, pp. 4955-4963, 2019.

[128] T. E. Daubert, "Physical and thermodynamic properties of pure chemicals: data compilation," *Design Institute for Physacal Property Data (DIPPR),* 1989.

[129] W. M. Haynes, *CRC handbook of chemistry and physics.* CRC press, 2016.

[130] H. Hiroyasu and M. Arai, "Structures of fuel sprays in diesel engines," *SAE transactions,* pp. 1050-1061, 1990.

[131] A. Saito and K. Kawamura, "Behavior of fuel film on a wall at fuel spray impinging," *International Journal of Fluid Mechanics Research,* vol. 24, no. 4-6, 1997.

LIST OF PUBLICATIONS

International Journals

[1] **Shi PH**, Zhang GX, Luo HL, Ogata Y, Nishida K. The effect of split injection on fuel adhesion characteristics under static flow and cross-flow field conditions. Fuel 2023; 354: 129282. (Q1，IF=7.4)

[2] **Shi PH**, Zhang GX, Luo HL, Ogata Y, Nishida K. Effect of wall-impingement distance on fuel adhesion characteristics of split injection spray under cross-flow condition. Fuel 2024; 362: 130807. (Q1，IF=7.4)

[3] Zhang GX, **Shi PH**, Luo HL, Ogata Y, Nishida K. Investigation on fuel adhesion characteristics of wall-impingement spray under cross-flow conditions. Fuel 2022; 320: 123925. (Q1，IF=7.4)

[4] Zhang GX, **Shi PH**, Dong PP, Zhang FY, Zhang YF, Luo HL. Experimental Study on the Adhesive Fuel Features of Inclined Wall-Impinging Spray at Various Injection Pressure Levels in a Cross-Flow Field. Sustainability 2023; 15 (7): 6312. (Q2，IF=3.9)

International Conferences

[1] **Shi PH**, Zhang GX, Trong NB, Luo HL, Ogata Y, Nishida K. Effect of Cross-Flow Velocity on Fuel Adhesion of Flat-Wall Impinging under Triple Injection Strategy. 2023 SAE/Pel, Best paper award.

[2] **Shi PH**, Ogata Y, Nishida K, Trong NB, Luo HL, Zhang GX. Influence of impingement distance on fuel adhesion of flat-wall impinging fuel spray in cross-flow ambient. 2024 ICLASS international conference.

[3] **Shi PH**, Zhang GX*, Luo HL, Ogata Y, Nishida K. Adhesion Characteristics of Flat-Wall Impinging Fuel Spray under Cross-flow Condition. ICEs 2022.

[4] Zhang GX, **Shi PH**, Luo HL, Ogata Y, Nishida K. RIM Experiment on Fuel Adhesion Characteristics of Inclined-Wall-Impinging Spray under Cross-Flow Conditions. COMODIA 2022.

ACKNOWLEDGEMENT